HYDROGENOLYSIS OF GLYCEROL OVER NI-BASED CATALYSTS.

Bárbara Cristina Miranda Morales

Dipòsit Legal: T 1654-2014

Bárbara Cristina Miranda Morales

Hydrogenolysis of glycerol over Ni-based catalysts

Doctoral thesis

Supervised by

Dr. Ricardo Chimentão

Dr. Francesc Medina

Department of Chemical Engineering

Universitat Rovira i Virgili

Tarragona

2014

UNIVERSITAT ROVIRA I VIRGILI

Departament d' Enginyería Química
Av. Països Catalans, 26
Campus Sescelades
43007, Tarragona
Tel. 977 55 86 75
Fax. 977 55 96 21

Dr. Ricardo Chimentão, Researcher and Dr. Francesc Medina, Professor and Researcher of the Department of Chemical Engineering at the University Rovira i Virgili.

CERTIFY:

That the doctoral thesis entitled: "Hydrogenolysis of glycerol over Ni-based catalysts" by Bárbara Cristina Miranda Morales to obtain the degree of doctor from the University Rovira i Virgili, has been carried out under our supervision in the Department of Chemical Engineering at the University Rovira i Virgili in Tarragona, Spain.

Tarragona, September 2014.

Dr. Ricardo Chimentão Dr. Francesc Medina

Agradecimientos

En primer lugar quiero expresarle mi sincero agradecimiento al Dr. Jesús Sueiras por mostrar interés en Costa Rica y en la escuela de Ingeniería Química de la Universidad de Costa Rica. Gracias por el apoyo brindado para emprender este nuevo reto profesional en mi vida.

Agradezco al Dr. Francesc Medina por acogerme en su grupo de investigación (Catheter), y por su supervisión durante el doctorado.

Quiero agradecer al Dr. Ricardo Chimentão por su supervisión y toda la ayuda que me brindó para llevar a cabo esta investigación. Por todas sus enseñanzas pues el tema era nuevo para mí, por toda la paciencia que me mostró en el camino. Decirle que termino este proyecto considerándolo un amigo para toda la vida.

Al Dr. Joao B.O. Santos (Universidade Federal de São Carlos) por toda su colaboración, por sus consejos y revisiones que hicieron que esta investigación fuera por buen camino.

Al Dr. Jordi Llorca (Universitat Politècnica de Catalunya) y al Dr. Francesc Gispert-Guirado (Universitat Rovira i Virgili), por toda la ayuda brindada en la realización e interpretación de análisis.

Al European Synchrotron Radiation Facility (ESRF), Brazilian National Laboratory Light Synchrotron (LNLS), y al Pacific Northwest National Laboratory (PNNL) por su apoyo en la realización de análisis XRD, XANES y FTIR-CO, respectivamente.

A mi alma máter, la Universidad de Costa Rica, por confiar en mi capacidad profesional, por su apoyo económico. Regresaré feliz a esta institución educativa a aportar lo que he aprendido durante esta experiencia de vida.

Un agradecimiento especial a mi familia que desde lejos me han alentado con su apoyo y muestras de amor.

A mi amiga Angie, que a pesar de la distancia nunca me ha dejado sola, por nuestros viajes por estos rumbos que siempre recordaré.

A Carlos, gracias por tu compañía.

UNIVERSITAT ROVIRA I VIRGILI
HYDROGENOLYSIS OF GLYCEROL OVER NI-BASED CATALYSTS.
Bárbara Cristina Miranda Morales
Dipòsit Legal: T 1654-2014

Table of Contents

Chapter 4- Influence of copper on nickel-based catalysts in the hydrogenolysis of glycerol

Appendix

UNIVERSITAT ROVIRA I VIRGILI
HYDROGENOLYSIS OF GLYCEROL OVER NI-BASED CATALYSTS.
Bárbara Cristina Miranda Morales
Dipòsit Legal: T 1654-2014

Abstract

World demand for energy, chemicals and products is increasing every year. Current production systems and consumption patterns are now unsustainable. New alternative ways must be developed to satisfy not only the energy needs and the production of chemicals but also for a more friendly effect on the environment. Biomass resources such as glycerol represent one alternative to this. Due to the highly functionalized nature of glycerol, it can readily be submitted to different processes such as hydrogenolysis, dehydration, and hydrogenation to obtain alternative commodity chemicals.

The catalyst role in the mechanism of the cleavage of the C-C and C-O bonds which modulates the routes in the glycerol conversion is the key to control the selectivity to target products. Because of that, this research work wishes to contribute with the development of catalysts for the catalytic transformation of glycerol to high value-added chemicals, and to understand the catalyst structure relationship with the catalytic performance. The attention of the present research is devoted to the glycerol conversion over Ni based catalysts. The main disadvantage of nickel catalysts is their lower stability due to carbon deposition. How to improve the stability of Ni-based catalysts remains a matter of debate.

Chapter 3 of this thesis was focused on the catalytic conversion of glycerol in gas phase over Ni/γ-Al_2O_3 catalyst at atmospheric pressure and 573 K in the presence of hydrogen in a fixed bed reactor. Different reduction temperatures of the Ni samples were used as parameter to evaluate its effect on the catalytic performance. The structure of the catalysts was characterized using techniques such as XRD, H_2-chemisorption, TEM, and XANES. The results show that the stability and the catalytic behavior of the catalysts were affected by the reduction pre-treatment. A glycerol reaction pathway was proposed based on dehydration, dehydrogenation and hydrogenolysis steps. The main products identified were: hydroxyacetone, pyruvaldehyde, pyruvic acid, lactic acid, lactide, acetaldehyde and CH_4. The number of exposed Ni atoms and the degree of reduction of the NiO species determined the hydrogenolysis reaction of glycerol to CH_4 formation. The catalyst was deactivated by coke formation, by transformation of Ni phase to Ni_3C, as well as by oxidation of the Ni phase during the reaction. In addition, Raman analysis revealed two types of carbonaceous deposits over the used samples: on the Ni species and on the

support. The regeneration of the catalysts was also studied. The regeneration treatment by oxidation-reduction reactivated the catalyst successfully.

It is know that the introduction of a second metal to catalyst systems may provide significant changes in the catalytic activity, selectivity and in the formation of coke. Unlike Ni, the hydrogenolytic capacity of Cu to cleavage the C-C bonds is poor. However, Cu is an efficient catalyst for the cleavage of C-O bonds, which can dramatically affect the product distribution in glycerol hydrogenolysis. Then, Chapter 4 was focused to study the effect of Cu introduction into Ni in the glycerol conversion. Different Ni/Cu atomic ratios of 8/1, 4/1, 2/1, 1/1, 1/2, 1/4, 1/8 were studied. XPS analysis revealed that the surface composition of the catalyst exhibited progressive enrichment of Cu as its content in the catalyst increased. H_2-chemisorption indicated that the total number of exposed Ni atoms decreased as the Cu content increased. As a result, deep hydrogenolysis to produce CH_4 was inhibited by the addition of Cu to the Ni catalyst, rendering higher selectivity towards the dehydration products of glycerol such as hydroxyacetone. FTIR spectra of adsorbed CO revealed that Cu asserts both geometric and electronic effects on the adsorption properties of Ni. HRTEM revealed metal particles very well distributed on the support with particle size of 1.5 nm to 5 nm. XRD showed that the Ni-Cu samples were not a total intermetallic alloys. Catalytic deactivation was observed in the glycerol conversion by coke formation. TPO results showed an increase in carbon deposition in the samples with higher Cu indicating the direct involvement of Cu species in the dehydration of glycerol which markedly contributes to the carbon deposition on the catalysts.

Resumen

La demanda de energía en el mundo va en aumento año a año. Los sistemas de producción y patrones de consumo actuales son insostenibles. Existe la necesidad de desarrollar nuevas formas de satisfacer no sólo, la demanda de energía y producción de compuestos químicos, sino también de encontrar una forma de hacerlo que sea amigable con el ambiente. El glicerol, como recurso biomásico, representa una alternativa a esto. Gracias a la alta funcionalidad de su estructura química, el glicerol puede ser sometido a procesos tales como la hidrogenólisis, la deshidratación, y la hidrogenación para obtener diferentes compuestos químicos.

El catalizador cumple un papel clave en el mecanismo de rompimiento de los enlaces C-C y C-O del glicerol, y modula la selectividad hacia los productos deseados. Debido a esto, el presente trabajo de investigación desea contribuir en el desarrollo de catalizadores para su aplicación en la transformación catalítica de glicerol a productos químicos de alto valor. Además, ayudar al entendimiento de la relación entre la estructura del catalizador y la actividad catalítica. La atención de esta investigación se centra en la conversión de glicerol sobre catalizadores de níquel, cuya principal desventaja es su baja estabilidad debido a la deposición de carbón. Cómo mejorar la estabilidad de los catalizadores de níquel es aún un tema de debate.

El capítulo 3 de esta tesis se enfocó en estudiar la conversión catalítica de glicerol en fase gas sobre un catalizador de Ni/γ-Al_2O_3 a presión atmosférica, 573 K y en presencia de hidrógeno en un reactor de lecho fijo. La temperatura de reducción del catalizador fue empleada como parámetro para evaluar su efecto sobre la actividad catalítica. La estructura de los catalizadores fue caracterizada por medio de técnicas tales como XRD, quimisorción de H_2, TEM y XANES. Los resultados muestran que la actividad y estabilidad de los catalizadores fue afectada por la temperatura de reducción empleada. Con base en las rutas de deshidratación, deshidrogenación e hidrogenólisis observadas, se propuso una ruta química general donde los principales productos identificados fueron: hidroxiacetona, piruvaldehído, ácido pirúvico, ácido láctico, lactide, acetaldehído y CH_4. El número de átomos de Ni expuestos y el grado de reducción de las especies de NiO afectaron la ruta de hidrogenólisis del glicerol hacia CH_4 y con ello, la estabilidad catalítica. Los catalizadores fueron desactivados por deposición de carbón, por la transformación de la fase de Ni metálico a Ni_3C, así como por la oxidación del Ni durante la reacción. Además, el análisis

Raman reveló la presencia de depósitos carbonosos tanto sobre la partícula de Ni como sobre el soporte. La regeneración de los catalizadores también fue estudiada. Se observó que el catalizador se reactiva por completo por medio de pasos de oxidación-reducción.

La introducción de un segundo metal a un catalizador puede provocar cambios significativos en la actividad, selectividad y formación de carbón del mismo. A diferencia del Ni, la capacidad del Cu de romper enlaces C-C es pobre. Sin embargo, el Cu es un metal eficiente en el rompimiento de enlaces C-O, lo cual puede afectar dramáticamente la distribución de productos durante la conversión de glicerol. Con base en ello, el capítulo 4 de esta tesis fue enfocado al estudio del efecto de la introducción de Cu en el catalizador de Ni/γ-Al_2O_3 sobre la conversión del glicerol. Diferentes razones atómicas Ni/Cu (8/1, 4/1, 2/1, 1/1, 1/2, 1/4, 1/8) fueron estudiadas. Los análisis de XPS revelaron que la composición de la superficie del catalizador exhibió un progresivo enriquecimiento en Cu conforme su contenido se incrementó en el catalizador. La quimisorción de H_2 indicó que el número total de átomos de Ni expuestos disminuyó conforme el contenido de Cu en el catalizador aumenta. Además, la ruta de hidrogenólisis para producir CH_4 fue inhibida por la introducción de Cu al catalizador de Ni, y con ello aumentó la selectividad hacia productos de la ruta de deshidratación tales como la hidroxiacetona. Los espectros de FTIR-CO revelaron tanto el efecto geométrico como electrónico del Cu sobre las propiedades de adsorción del Ni. Los resultados de HRTEM mostraron partículas metálicas bien distribuidas sobre el soporte con un tamaño de 1.5 nm a 5 nm. Por medio de XRD se observó que existe una pobre aleación en los catalizadores de Ni-Cu. La desactivación del catalizador fue observada durante la conversión del glicerol. Los resultados de TPO mostraron un aumento en la cantidad de carbón depositado en los catalizadores conforme aumentó el contenido de Cu, lo cual indica la participación del Cu en la deshidratación del glicerol, ruta que contribuye marcadamente a la deposición de carbón sobre el catalizador.

Index of Figures

Index of Tables

Index of Schemes

UNIVERSITAT ROVIRA I VIRGILI
HYDROGENOLYSIS OF GLYCEROL OVER NI-BASED CATALYSTS.
Bárbara Cristina Miranda Morales
Dipòsit Legal: T 1654-2014

List of Abbreviations

Abbreviation	Name
Al	Alumina
C	Carbon
Cu	Copper
I	Intensity
Ni	Nickel
Ref	Reference
RT	Room Temperature
S	Surface area
Satel	Satellite
Si	Silicium
T	Temperature
WL	White Line

Subscripts	Meaning
BET	Brunauer, Emmett and Teller
D	D-band
G	G-band
Red	Reduction

Chapter 1

General Introduction and Motivation

1.1 The rise of renewable energy

Fuels from crude oil supply are the majority worldwide energy demand for transport. There is a shortage of fossil fuel resources. The use of fossil fuels results in the collapse of the balance between CO_2 released to the environment, and the CO_2 that can be absorbed by plants. World demand for energy, chemicals and products is increasing every year. Current production systems and consumption patterns are now unsustainable. New alternative ways must be developed to satisfy not only the energy needs and the production of chemicals but also for a more friendly effect on the environment. The biomass resources represent one alternative to substitute fossil fuel energy [1, 2].

Biomass stores sunlight in the form of chemical energy. Plants use CO_2 in the process and they return that carbon, along with the solar energy, into stable organic compounds. This makes organic biomass a clear source for renewable energy maintaining a closed carbon cycle. It can be processed at some cost and effort into hydrocarbon fuel of the sort that today´s car, trucks and planes employ [3, 4].

The idea of using living plants as way to capture the all-but-unlimited energy of Sun has a great interest. Any and all contributions are certainly needed to replace the fossil resources, but: would the biomass potential be sufficiently large to justify the necessary capital replacements in the fuels? Can biomass production ever start to replace oil supplies over time – is there enough land and can it be converted to useful products efficiently?

The emission of solar energy to the Earth is 174 387 TW. The absorbed solar energy is about 124 600 TW. Most of the absorbed solar energy is converted into heat which is about 83 700 TW. About 32 % of absorbed energy takes part in the hydrological Earth cycle (about 40 400 TW). Around 400 TW are used for air movement. Other 100 TW of absorbed solar energy are driving forces behind the production of biomass. The ratio between the used energy to the energy put into the photosynthesis process amounts approximately 34%. In this way about 0.1% of solar energy takes part in the photosynthesis [3]. The biomass may not represent the total answer to our global energy problems but they have a substantial potential as a source for carbon neutral [4].

Plants are strikingly poor transducers of the solar energy; even an intensively managed plantation struggles to store away more than a watt or two per square meter on average. Highly efficient converters of fixed carbon to biomass, such as sugarcane can store about 1 % of incident light as biomass over a year. In addition, the rate of biomass

growing in time is not enough to compensate the CO_2 emitted into the atmosphere. The plants during the growing season need about 10 years in ideal conditions (proper lighting, temperature and humidity) [3].

There are many challenges if we want seriously consider the biomass as part of the sustainable energy source for the future. The processing of biomass to useful compounds must avoid the competition with the food- stock. It is necessary to reduce processing costs and integrate the products into the supply chain and get to the consumers. It is critical the minimization of the overall life cycle impact taking into account the use of lands, cost of process, the carbon foot print and the socio-economic benefit.

Biomass is a dilute energy source so to be truly useful one need to modify it first. A shift of the carbon resource base to biomass derived feedstocks requires a different approach and chemistry than that employed today for the fossil carbon sources. In contrast to oil and gas, carbohydrate biomass and the corresponding polyalcohols derived from it are characterized by an abundance of hydroxyl functions, i.e. are *overfunctionalized* exhibiting a reactivity that is very high and very difficult to control. The strategy of deoxygenation must be considered. The deoxygenation of carbohydrate biomass consists of an acid-catalyzed dehydration followed by a metal-catalyzed hydrogenation and/or hydrogenolysis, stoichiometrically resulting in a net removal of one oxygen atom per hydrogen molecule expended. Depending on the nature of the substrate many different intermediates will be formed and these two steps may have to occur iteratively several times [5]. The transformation of biomass feedstock molecules into linear chains is a necessary step in the production of energy-dense fuels because these linear chains can then be reduced and deoxygenated into alkanes used in gasoline and diesel fuel [5].

It is necessary to consider the best use of biomass resources. To determine how biomass is best utilized the effective H/C ratio, which is the ratio between H and C atoms in the molecule adjusted for heteroatoms, can be considered. For a molecule containing only C, H, and O, the ratio is calculated by the Equation (1.1). It provides a quantitative number for the overall degree of oxidation in a given molecule [6].

$$H/C\,ratio = \frac{n(H) - 2n(O)}{n(C)} \qquad \text{Eq. (1.1)}$$

Transportation fuels have an effective H/C ratio in the range of 1 to 2.3 (purple box, Figure 1.1), which is close to the ratio of crude oil. This ratio implies a high energy density, and it is thus ideal for liquid fuel purposes. Commodity chemicals, on the other hand, span a much wider H/C ratio (blue box, Figure 1.1) which is more comparable to that of biomass. A wide gap in the effective H/C ratio between a resource and a target chemical implies that a lengthy process is needed for its conversion [6].

By utilizing biomass as feedstock for the production of commodity chemicals instead of fuels, the necessity for deoxygenation, which is one of the biggest challenges when making fuels from biomass, can be also partially or even completely avoided. An opposite strategy to the deoxygenation must be also considered. Oxidation reactions typically involve product loss owing to overoxidation. It is also desirable if these reactions could be avoided, or at least their use minimized.

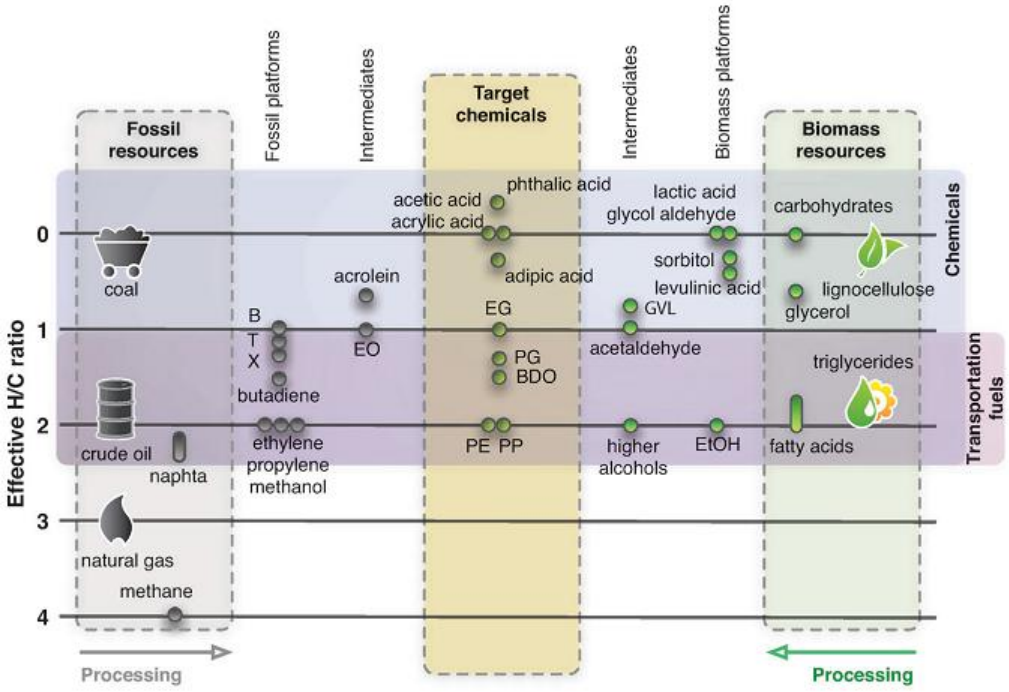

Figure 1.1 Effective H/C ratio map of current and future bulk chemicals as well as feedstocks with a qualitative indication of the degree of processing. B = benzene, BDO = 1,4-butanediol, EG = ethylene glycol, EO = ethylene oxide, GVL = γ-valerolactone, PE = polyethylene, PG = propylene glycol, T = toluene, X = xylenes [6]

1.2. Glycerol

Glycerol is an important molecule with an H/C ratio effective for the production of commodity chemicals (Figure 1.1). Glycerol is obtained as by-product during the production of biodiesel which is done by transesterification of vegetable oils and animal fats with CH_3OH using NaOH as a base catalyst, or from batch esterification of fatty acids catalyzed by sulfuric acid (Scheme 1.1). Glycerol is normally generated at the rate of 1 mol of glycerol for every 3 mol of methyl esters synthesized; that is approximately 10 wt% of the total product [7, 8].

100 kg of oil + 10.5 kg CH_3OH = 100 kg methyl esters (biodiesel) + 10.5 kg glycerol

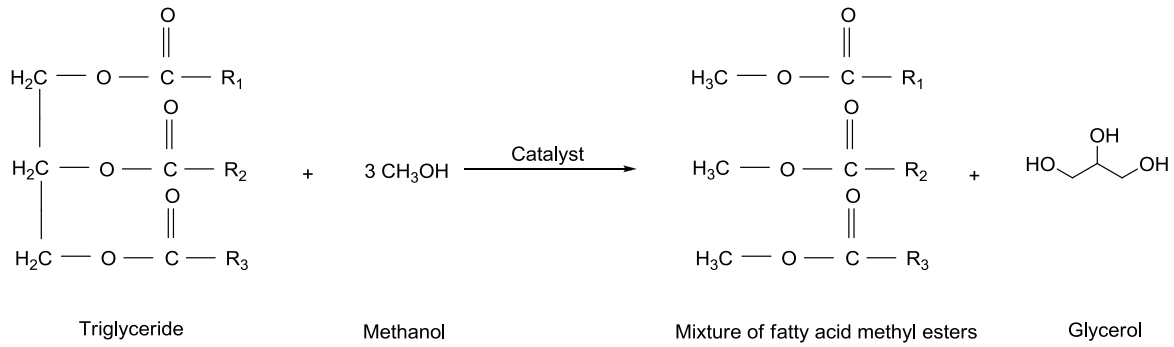

Scheme 1.1 Transesterification of a triglyceride with methanol [7]

The growing amount of glycerol derived from biodiesel has led to the development of new solutions in terms of recycling it in other processes. Traditional applications of glycerol, either directly as an additive or as a raw material, range from its use as a food, alkyd resins and polyurethanes [7, 9].

Due to the highly functionalized nature of glycerol, it can readily be submitted to different processes such as oxidation, hydrogenolysis, dehydration, pyrolysis, halogenation, etherification, esterification, fermentation and so on to obtain alternative commodity chemicals [1, 8, 10-13] (see Figure 1.2), such as glyceric acid [14] and dihydroxyacetone [15], mesoxalic acid, 3-propanediol [16], 1,3-dichloropropanol, glyceryl ethers, glycerol carbonate, and glyceryl esters [10, 12, 17, 18].

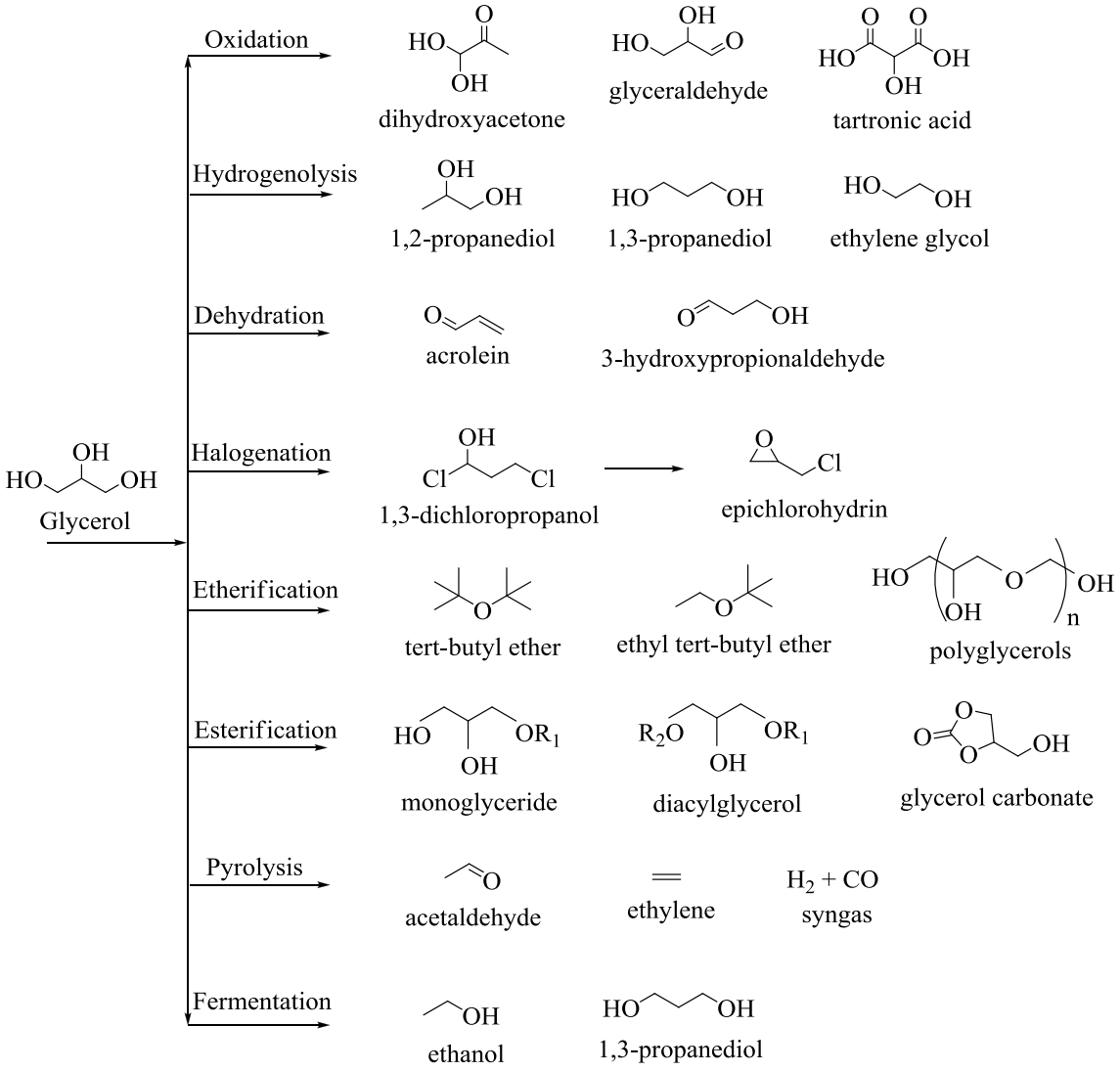

Figure 1.2 Processes of conversion of glycerol into useful chemicals [8, 10]

1.2.1 Hydrogenolysis of glycerol

Hydrogenolysis describes a chemical reaction whereby C-C or C–Heteroatom single bonds are cleaved by hydrogen [19] and occurs the formation of C-H bonds [20]. One industrially relevant route for the conversion of glycerol involves hydrogenolysis to polyols such as ethylene glycol (EG) and propanediol (1,2-PDO and 1,3-PDO). 1,2-PDO and EG are often used in antifreeze, paints, functional fluids, humectants, and polyester resins. 1,3-PDO is a valuable chemical used in the synthesis of polymethylene terephthalates, manufacture of polyurethanes and cyclic compounds [21, 22]. These glycols are usually produced from petroleum derivatives [12]. Due to shortages and rising

oil prices an alternative route for obtaining thermoplastic resins from renewable becomes an issue of central importance.

1.2.2 Dehydration of glycerol

Dehydration reaction involves the loss of a water molecule from the glycerol. Two important chemicals can be produced directly by dehydration of glycerol, acrolein and 3-hydroxypropionaldehyde (3-HPA) [23]. Acrolein has significant application as an herbicide for the control of aquatic plants. The current method for manufacturing acrolein is based on oxidation of propylene or propane derived from petroleum [24]. 3-HPA is a precursor for many modern chemicals including acrolein, acrylic acid, and 1,3-PDO and it is used for polymer production. Typically, 3-HPA is produced by synthesis from petrochemicals [25].

1.3. Different value-added chains in the glycerol conversion

The conversion of glycerol has been investigated both in liquid and gas phases. The conversion of glycerol in liquid phase is usually carried out at temperatures ranging from 393 K to 533 K and pressures of 1 MPa to 50 MPa using noble metals such as Pt and Ru [26-32]. Fukirado et al. [33] carried out the conversion of glycerol to 1,2-PDO and 1,3-PDO, over Rh/C, Ru/C, Pt/C, Pd/C catalysts (also SiO_2 and Al_2O_3 as supports) at 393 K and 8 MPa of H_2 pressure. Perosa et al. [34] performed the conversion of glycerol to 1,2-PDO, over Raney Ni catalyst at 463 K and 1 MPa of H_2 pressure. One drawback of the liquid phase reaction is that it needs expensive high pressure equipment which can increase the selectivity to degradation products [35] and that increase capital cost [7]. Huang et al. [36] reported the hydrogenolysis of glycerol in both liquid and vapor phases using the co-precipitated $Cu/Zn/Al_2O_3$ catalyst. A selectivity of 92.2 % to 1,2-PDO at 96.2 % conversion was achieved in the vapor phase at 463 K and 0.64 MPa of H_2. Using the same catalyst, the liquid-phase hydrogenolysis requires more severe conditions (473 K and 5 MPa H_2) and showed lower selectivity to 1,2-PDO (80.1 % at 20.4 % conversion).

The conversion of glycerol in gas phase is typically carried out at temperatures ranging from 373 K to 673 K and atmospheric pressure [23, 37-40]. Vasconcelos et al. [41], carried out the dehydration of glycerol over CeO_2–ZrO_2 catalyst in gas phase in a range of temperature between 373 K and 623 K and 0.1 MPa to obtain 1-hydroxycetone.

Suprun et al. [42] carried out the dehydration of glycerol to acrolein and hydroxyacetone, over Al_2O_3–PO_4 and TiO_2–PO_4 catalysts at 553 K at atmospheric pressure. Moreover, Atia et al. [43] performed the dehydration of glycerol to acrolein, over heteropolyacid catalysts, in a range of temperature between 498 K and 573 K at atmospheric pressure. Feng et al. [44] carried out the hydrogenolysis of glycerol over Cu/ZnO/MOx (MOx=Al_2O_3, TiO_2, and ZrO_2) catalysts in gas phase in a range of temperature between 513 K and 573 K and 0.1 MPa to obtain 1,3-PDO, EG, and hydroxyacetone.

1.3.1 Proposed reaction pathways for the glycerol hydrogenolysis

Several mechanisms have been proposed for the hydrogenolysis of glycerol [45-47]. The formation of 1,2-PDO and EG from glycerol can occur via several routes as discussed in this section. Dasari et al. [45] performed the hydrogenolysis of glycerol to 1,2-PDO using solid acid catalysts such as Ni, Pd, Pt, Cu and copper chromite catalysts, at 473 K and H_2 pressure of 1.38 MPa. The first route, proposed in that investigation [45], involves the direct dehydration of glycerol molecule to hydroxyacetone, which further reacts with H_2 to form 1,2-PDO (Scheme 1.2).

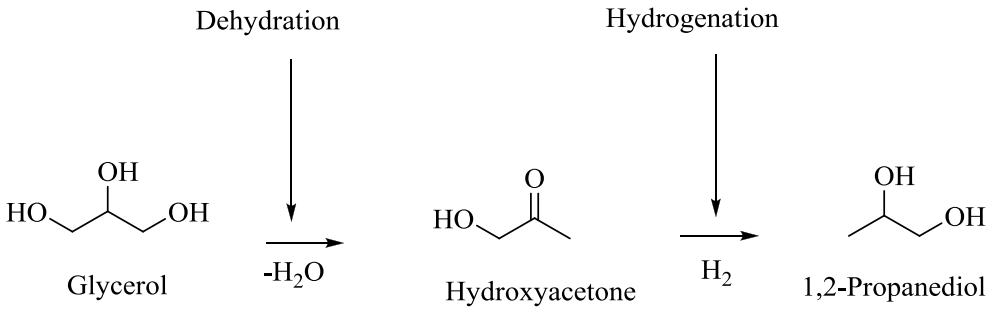

Scheme 1.2 Reaction mechanism for conversion of glycerol to 1,2-PDO proposed by Dasari et al. [45]

The mechanism proposed by Montassier et al. [48], is shown in Scheme 1.3. Dehydration and retro-aldol reactions of polyols were studied over a bimetallic Cu-Ru catalyst. According to this mechanism, the dehydrogenation of glycerol leads to glyceraldehyde, which is followed by dehydration to 2-hydroxyacrolein and subsequent hydrogenation to 1,2-PDO. Glyceraldehyde can also form glycolaldehyde and formaldehyde and subsequent hydrogenation to EG and methanol. The cleavage of C-C

bonds occurs through a base-catalyzed retro-aldol reaction, whereas the C-O cleavage occurs through a base-catalyzed dehydration reaction. The initial dehydrogenation step is believed to occur on the transition metal catalyst.

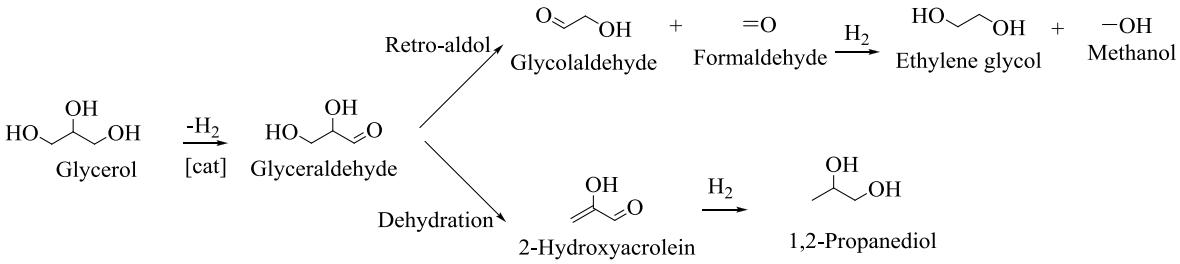

Scheme 1.3 Reaction scheme for the formation of 1,2-PDO as proposed by Montassier et al. [48]

The mechanism proposed by Maris and Davis [49], as illustrated in Scheme 1.4, is based on what Montassier et al. [48] proposed, but was adjusted on the results obtained in their study. Maris and Davis [49] investigated the selectivity and activity of Ru/C and Pt/C in the hydrogenolysis of glycerol. The effects of NaOH and CaO addition on the reaction rates were used to elucidate the metal-catalyzed versus base-catalyzed routes on the mechanism. The first step is the dehydrogenation of glycerol to glyceraldehyde on the transition metal catalyst and it can be enhanced by the presence of a base. The formation of EG can occur via two routes. Ru is an effective C-C bond cleavage catalyst, and therefore glyceraldehyde can be directly hydrogenated to EG and methanol over Ru. Pt, on the other hand, is not effective for C-C bond cleavage and therefore the formation of EG is via a base-catalyzed retro-aldol route. The base-catalyzed dehydration of glyceraldehyde yields pyruvaldehyde, which forms lactate in the presence of a base. Subsequent hydrogenation of the dehydration intermediates on the metal catalyst gives 1,2-PDO.

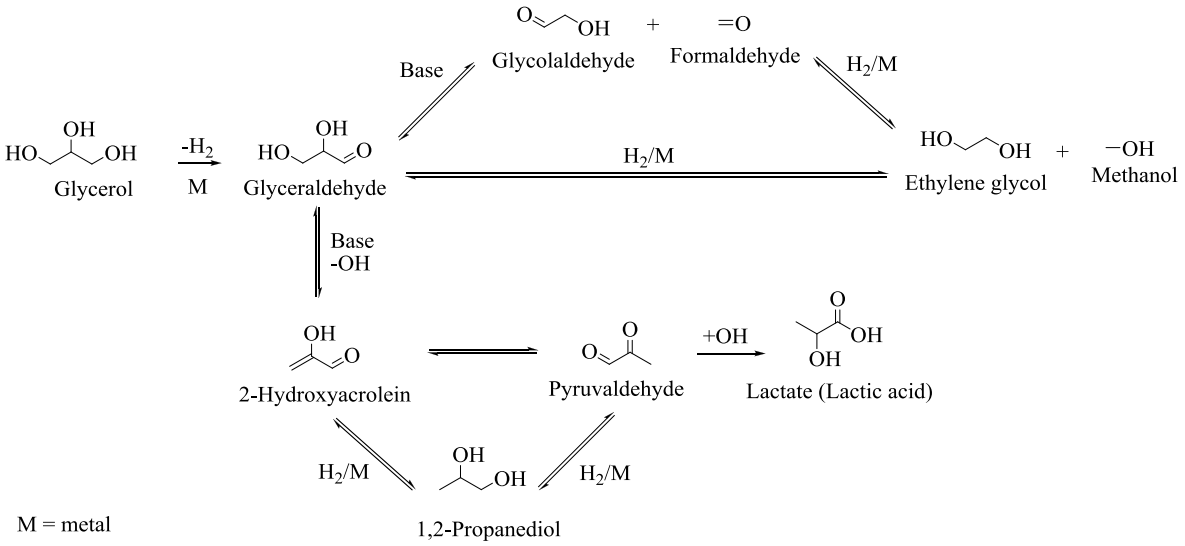

Scheme 1.4 Reaction scheme for the hydrogenolysis of glycerol proposed by Maris and Davis [49]

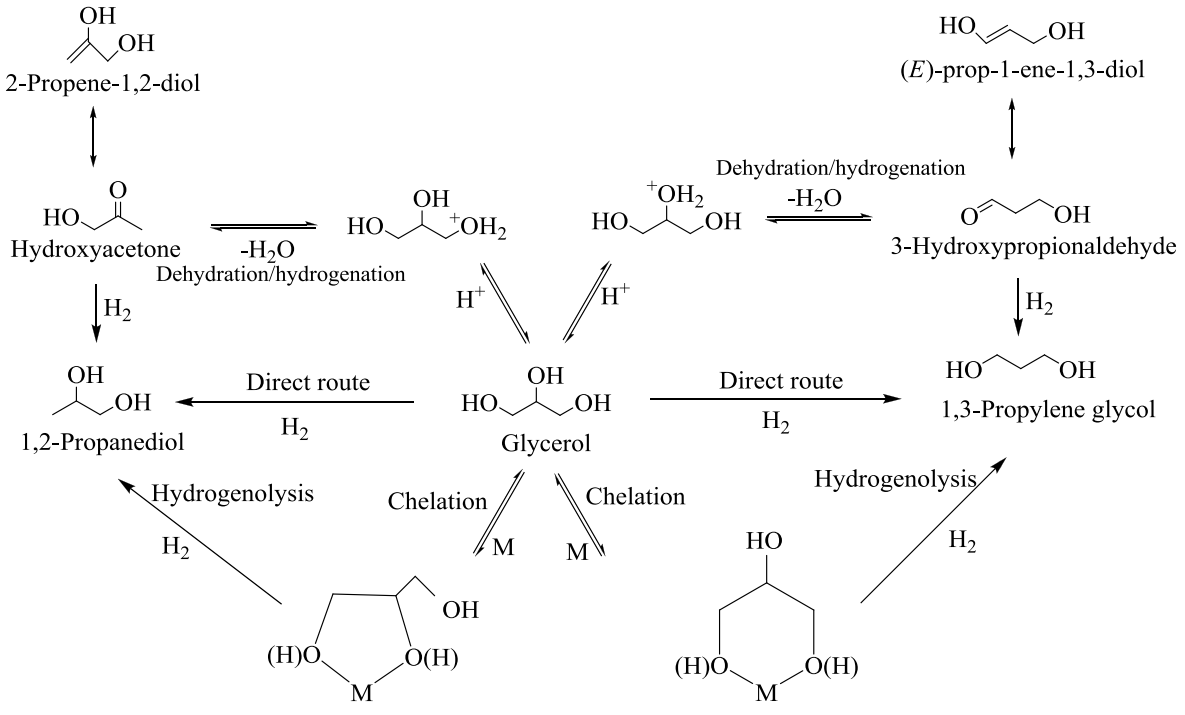

Scheme 1.5 Reaction scheme proposed by Chaminand et al. [50]

Chaminand et al. [50] proposed that diols can be form via several routes as shown in Scheme 1.5. They proposed a mechanism to explain the influence of different

parameters on the activity and selectivity of the reaction. They investigated the influence of the support on the Ru catalyst as well as the influence of a solvent on the hydrogenolysis of glycerol over Ru/C catalyst. The presence of an acid favoured the dehydration route via protonation of the hydroxyl groups of glycerol and then the loss of water forms a keto group as intermediate. If a primary OH group is protonated, then hydroxyacetone will be formed, which will lead to 1,2-PDO. If the secondary OH group is protonated, then 3-HPA is obtained and this keto group can be easily reduced under the reaction conditions to form 1,3-PDO.

Gandarias et al. [51], studied the role of acid and metal sites of Pt supported amorphous silica alumina (Pt/ASA) in glycerol hydrogenolysis to obtain 1,2-PDO. They also investigated the glycerol hydrogenolysis reactions under N_2 pressure due to H_2 available from glycerol aqueous phase reforming. Glycerol is first dehydrated to hydroxyacetone, which is then hydrogenated to 1,2-PDO. The last is further dehydrated to acetone and propanal; after hydrogenation of these products, 1-propanol (1-PO) and 2-propanol (2-PO) are formed (Scheme 1.6). Glycerol can also be dehydrated to 3-HPA, which is then subsequently hydrogenated to 1,3-PDO. 3-HPA is also readily dehydrated into acrolein. It was suggested that propanoic acid is produced through the oxidation of acrolein in aqueous solutions. Gandarias et al. [51] suggested that 3-HPA is very unstable and it was not detected in the reaction mixtures and it is instantaneously converted in subsequent reactions. Next, the route to cracked products was considered. The cracked products detected were EG, methanol, ethanol, acetaldehyde and acetic acid. It was suggested that EG and methanol were obtained directly from glycerol since these products were not detected in the experiments with 1,2-PDO, 1,3-PDO or hydroxyacetone as reactants. Furthermore, ethanol can be formed during the hydrogenolysis of EG and methane (CH_4) is formed from the hydrogenation of methanol. It was also proposed that acetaldehyde and formaldehyde were formed from 3-HPA, and that acetaldehyde is oxidized to acetic acid.

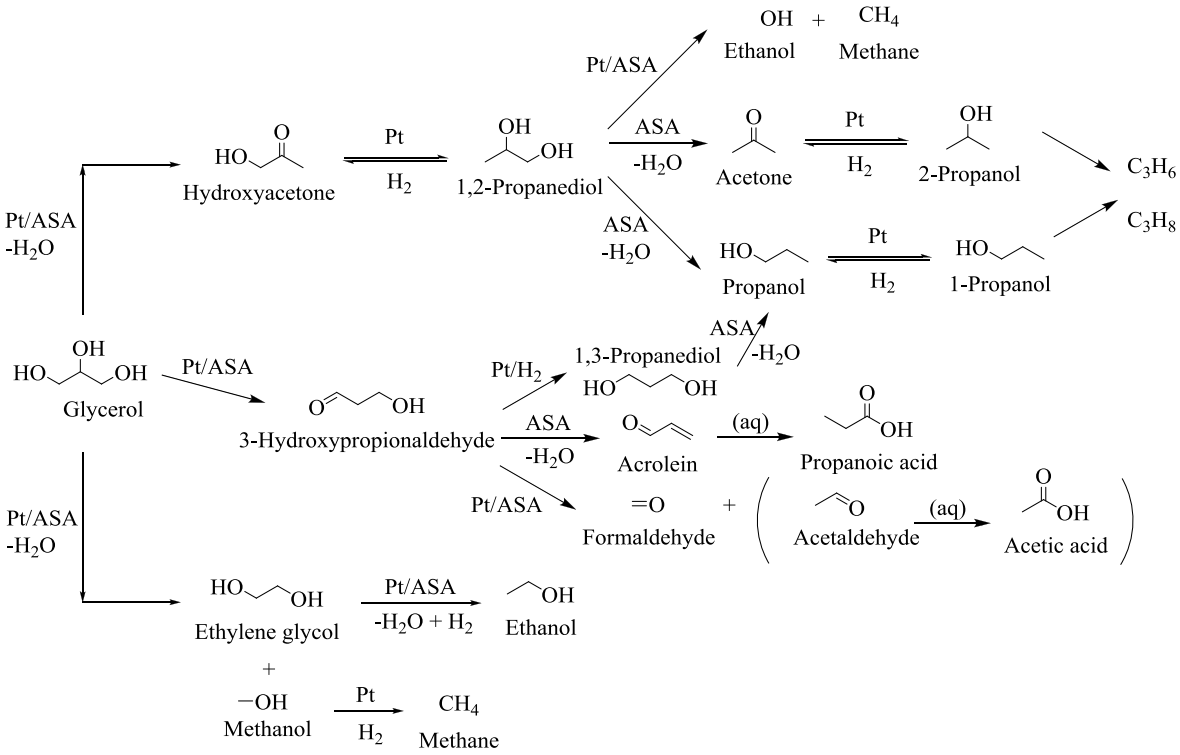

Scheme 1.6 Reaction scheme of glycerol hydrogenolysis and degradations products as proposed by Gandarias et al. [51]

Akizuki et al. [52] investigated the reactions of glycerol on TiO_2 and WO_3/TiO_2 in supercritical water at 673 K and 25 MPa - 41 MPa. The purpose of that study was to obtain fundamental knowledge of solid acid catalyzed reactions of glycerol in supercritical water. Both catalysts showed high activity in glycerol conversion. Main products were acrolein, acetaldehyde, hydroxyacetone and lactic acid. On TiO_2, propionic acid was also produced. Proposed reaction pathways are shown in Scheme 1.7. Glycerol was mainly consumed by dehydration reaction, which is known as a typical acid catalyzed reaction, and 3-HPA and hydroxyacetone were produced. 3-HPA is an unstable material and it is dehydrated into acrolein or decomposed into acetaldehyde and formaldehyde via retro-aldol reaction. Hydration of acrolein to 3-HPA also seems to occur. In general, TiO_2 has not only acid sites but also basic sites. These basic sites are considered to contribute to the production of lactic acid. On TiO_2, pyruvaldehyde was also considered to be formed from hydroxyacetone. Lactic acid is further dehydrated into acrylic acid and then hydrogenated into propionic acid.

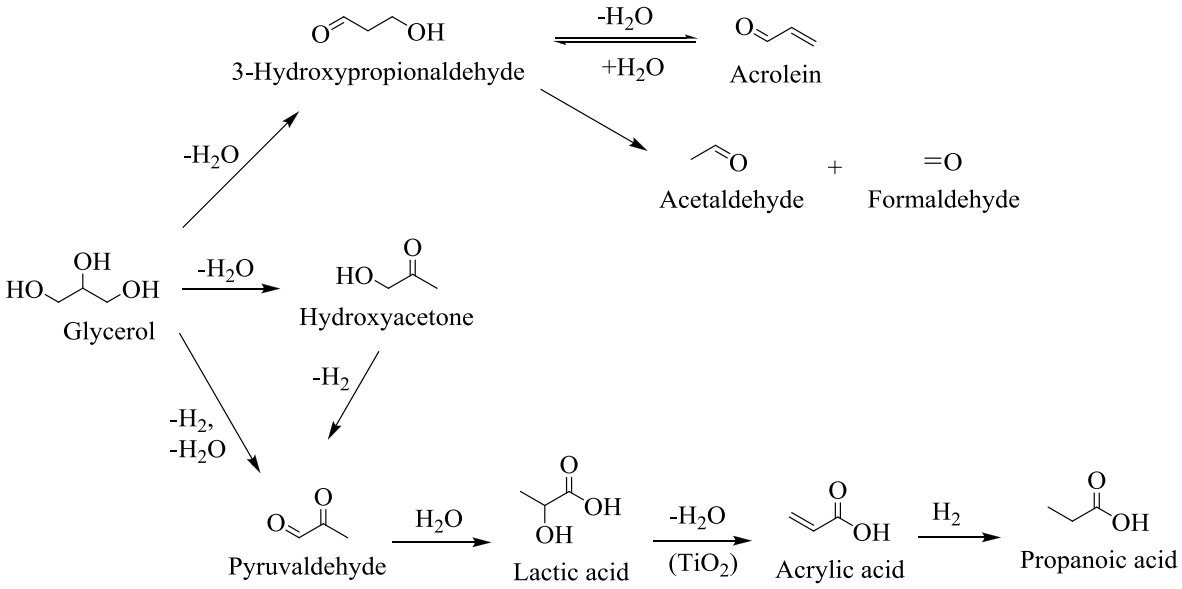

Scheme 1.7 Main reaction pathways on TiO_2 and WO_3/TiO_2 in supercritical water as proposed by Akizuki et al. [52]

1.4 Catalysts tested in the hydrogenolysis of glycerol

In the hydrogenolysis, the catalyst must have an ability to activate H_2 molecules since hydrogenolysis uses H_2 as a reactant. Noble metals are well known to be able to activate H_2 molecules and they are widely used in hydrogenation catalysts. In the hydrogenolysis of glycerol (Table 1.1, rows 1-7), Ru is frequently used as an active component [53, 54].

Noble-metal catalysts without additives generally give more than one product. There are several approaches to improve the selectivity to a desired product, and the most studied one is the addition of an acid (Table 1.1, rows 8-13).

Bases are also used as co-catalysts in the hydrogenolysis of glycerol (Table 1.1, rows 14-19), although the cases are fewer than using acidic co-catalysts.

Table 1.1 Selected examples of hydrogenolysis of aqueous glycerol over noble-metal catalysts

Row	Catalyst	H_2 (MPa)	Temperature (K)	Glycerol conversion (%)	Products	Ref
1	Ru/C	6	483	[a]	1,2-PDO, EG, propane, ethane	[48]
2	Ru-S/C	6	483	[a]	1,2-PDO, EG, methane	[48]
3	Ru/CNT	4	473	42.3	1,2-PDO, 1-PrOH, EG	[55]
4	Pt/C	1.38	473	34.6	1,2-PDO	[45]
5	Pd/C	1.38	473	5.0	1,2-PDO	[45]
6	Ru/C	1.38	473	43.7	1,2-PDO	[45]
7	Rh/SiO_2	8	393	7.2	1,2-PDO, 1,3-PDO, 1-PrOH, 2-PrOH	[33]
8	Ru/C+Amberlyst 15	8	393	79.3	1,2-PDO, EG, 1-PrOH, 2-PrOH	[56]
9	Ru/C +Amberlyst 70	8	453	48.8	1,2-PDO, 1,3-PDO, 1-PrOH, 2-PrOH, EG	[57]
10	Ru/C + Nb_2O_5	6	453	44.6	1,2-PDO, EG	[31]
11	Ru/C+$H_3PW_{12}O_{40}/ZrO_2$	6	453	44.0	1,2-PDO, EG	[31]
12	Ru/Al_2O_3	8	513	69	1,2-PDO, 1,3-PDO, PrOHs	[58]
13	Pt/SiO_2-Al_2O_3	4.5	493	19	1,2-PDO, 1,3-PDO, PrOHs, hydroxyacetone	[51]
14	Ru/TiO_2 + LiOH	3	443	89.6	1,2-PDO, EG	[59]
15	Ru/C + CaO	4	473	50	1,2-PDO, lactate, EG	[60]
16	Pt/C + CaO	4	473	40	1,2-PDO, lactate, EG	[60]
17	PtRu/C	4	473	100	1,2-PDO, lactate, formate	[49]
18	AuRu/C	4	473	100	1,2-PDO, lactate, formate	[49]
19	Pt/hydrotalcite	3	493	92.1	1,2-PDO	[61]

[a] Not reported

As well as noble metals, Cu [50, 62], Ni [34, 45, 63], and Co [64] are known to be able to activate H_2 molecules and are used as hydrogenation catalysts. Although the hydrogenation activity is generally lower than that of noble metals, the much lower prices and the high resistance to poisoning by trace impurities make non-noble-metal catalysts important. Application of non-noble-metal catalysts to glycerol hydrogenolysis has been investigated (Table 1.2).

Table 1.2 Selected examples of hydrogenolysis of aqueous glycerol over first-row transition metal catalysts

Catalyst	H_2 (MPa)	Temperature (K)	Glycerol conversion (%)	Products	Ref
Copper chromite	2.1	473	65.3	1,2-PDO	[45]
Cu-Zn-O	4.2	473	22.5	1,2-PDO, EG	[46]
Cu-Zn-Al-O	1.38	473	48	1,2-PDO, hydroxyacetone	[65]
Cu/SiO_2	9	473	73.4	1,2-PDO, EG	[47]
Cu/Al_2O_3	3.6	473	34.6	1,2PDO, 1,3-PD	[66]
Cu-Al-O	7	493	38	1,2-PDO, EG, hydroxyacetone	[67]
$Cu-ZnO/Al_2O_3$	10	463	25	1,2-PDO	[68]
Cu-MgO	3	453	94.2	1,2-PDO	[69]
Cu/Al_2O_3	0.1	393-473	100	1,2-PDO, EG, hydroxyacetone	[37]
RANEY® Copper	1.4	478	100	1,2-PDO, EG	[70]
RANEY® Nickel	1	463	97	1,2-PDO, ethanol, CO_2	[34]
Ni-Ce/active carbon	5	473	90.4	1,2-PDO, EG	[71]
$Ni-Pt/SiO_2$	8	453	79	1,2-PDO, EG, methane	[72]

1.5 Selectivity effects on bimetallic catalysts comprising combinations of metals from Groups VIII and IB

Since the pioneering work of Sinfelt et al. on the hydrogenolysis of ethane over Cu–Ni alloys in 1972 [73], Cu–Ni bimetallic catalysts have been considered as a representative system to study the structure–activity relationship in bimetallic catalysts. The activity of a metal catalyst for different reactions could be markedly altered by the incorporation of a second metallic element into the catalyst. A marked suppression in the formation of products of lower carbon number than the reactants is observed when a Group IB metallic element is incorporated with a Group VIII metal [20]. Table 1.2 shows

previous results dedicated on the study of the glycerol hydrogenolysis with Ni and Cu system.

In general, inclusion of a Group IB metal with a Group VIII metal marked decreases the hydrogenolysis activity of the latter but has a much smaller effect on the activity for reactions such as dehydrogenation of hydrocarbons [20]. In studies on the hydrogenolysis of ethane to CH_4, previous works have observed wide variation in catalytic activity from one metal to another [74]. It was shown that alloying Cu with Ni leads to catalytic effects in hydrogenolysis which are dramatically different from those observed for hydrogenation-dehydrogenation reaction.

Copper is well known to suppress C-C bond cleavage and be highly efficient for C-O hydro-dehydrogenation. The effect of Cu on the catalytic activity of Ni is strongly dependent on the nature of reaction. Ni-Cu metal system exhibits a high degree of specificity in catalyzing certain types of hydrocarbon transformations. Hydrogenation or dehydrogenation reactions would not be expected to behave like hydrogenolysis on bimetallic catalysts consisting of an active Group VIII metal in combination with an inactive Group IB metal. This line of reasoning leads to the expectation that the presence of the Group IB metal will markedly inhibit the hydrogenolysis activity of the Group VIII metal, thus rendering it more selectivity for hydrogenation or dehydrogenation reactions [20].

1.6 Catalytic hydrogenolysis and dehydrogenation over nickel-copper based catalysts

As was mentioned above, Ni and Cu catalysts have been investigated in the hydrogenolysis of glycerol. Some of the systems studied are brought up in this section:

1.6.1 Nickel- based catalysts

Nickel-based catalysts including RANEY® Nickel and supported catalysts have been tested for glycerol hydrogenolysis. Perosa et al. [34] converted glycerol to 1,2-PDO. When glycerol and RANEY® Nickel were heated to 423 K for 20 h in a stainless steel autoclave with 1 MPa of H_2, the conversion reached 12 % with 93 % selectivity to 1,2-PDO with small amounts of ethanol and CO_2 also formed. Addition of secondary metals has also been tested to change the activity and selectivity. The addition of cerium to Ni/active carbon decreased the reduction temperature of Ni, induced smaller Ni particle

size, and enhanced the catalytic activity [71]. The addition of Pt to Ni/SiO_2 enhanced the C–C hydrogenolysis activity to EG [72].

Alloying of catalysts is an alternative to improve catalytic performance by progressively changing the electronic structure of metals in catalysts [75]. Several Ni-based, alloyed catalysts have shown improved catalytic performance by improving their thermal stability during steam reforming, methanation, and direct hydrocarbon cracking [76, 77]. For example, nanoscale binary Fe-M (where M = Pd, Mo, Ni) catalysts containing 4.5 wt% Fe and 0.5 wt% M supported on Al_2O_3 were used for non-oxidative catalytic decomposition of CH_4 at 673 K – 773 K to produce pure H_2 and carbon nanofibers [78]. The bimetallic catalysts showed a higher activity than a corresponding monometallic catalyst containing 5 mol % Fe supported on Al_2O_3.

1.6.2 Copper-based catalysts

Copper is most often selected as an active component in the catalysts because of the high selectivity to 1,2-PDO in the glycerol hydrogenolysis. Copper chromite, a conventional hydrogenation catalyst, shows effective performance in the glycerol hydrogenolysis to 1,2-PDO [45] and it is selected by current industrial projects. Nearly 90 % selectivity at 65 % conversion is obtained at 473 K. Cu–ZnO catalysts, which are industrially used in methanol synthesis, water gas shift reaction, and methanol steam reforming, are also well studied [46, 65, 79]. Selectivities of about 80 % to 1,2-PDO are reported at relatively low conversions. Small amount of EG (2 %–10 %, selectivity) is almost always formed as a by-product. Pre-reduction of Cu–ZnO catalysts by H_2 stream is essential to avoid the aggregation of Cu particles in the reaction solutions and to obtain high selectivity to 1,2-PDO. Meher et al. [65] investigated the hydrogenolysis of glycerol over Cu/Zn-Al mixed oxide catalysts prepared by calcination of the hydrotalcite-type precursor. A glycerol conversion of 48 % with 94 % selectivity toward 1,2-PDO was obtained at 373 K and 0.7 MPa.

Supported Cu catalysts on SiO_2 [47, 80] or γ-Al_2O_3 [66] and the Cu–Al catalyst prepared by co-precipitation [67] were reported to be active in the glycerol hydrogenolysis to 1,2-PDO. Selectivities over 90 % were reported at $\leq$ 80 % conversions. The supported Cu–Zn catalyst on γ-Al_2O_3 was also reported [68], however, the performance (74 % selectivity at 25 % conversion) was not higher than Cu–ZnO without alumina.

Yuan et al. [69] published a comparative study of the hydrogenolysis of glycerol to 1,2-PDO over a CuO/MgO catalyst, prepared by impregnation and co-precipitation. The CuO/MgO catalyst prepared by co-precipitation showed the best activity with a glycerol conversion of 72 % and a 1,2-PDO selectivity of 97.6 %. Sato et al. [37] conducted the vapor-phase reaction of glycerol over the Cu/γ-Al_2O_3 catalyst at ambient H_2 pressure and gradient temperatures in the catalyst bed. The 1,2-PDO yield was initially limited at 80 % at 463 K. Dehydration needs relative high temperatures, whereas hydrogenation is favoured by low temperatures and high H_2 concentration. Sato et al. [37] developed a process where glycerol was dehydrated to hydroxyacetone at 473 K followed by the subsequent hydrogenation to 1,2-PDO at 393 K by controlling the thermodynamic equilibrium of the second hydrogenation step. In that process the 1,2-PDO yield was higher than 96 %.

Schmidt et al. [70] used a fixed bed RANEY® copper catalyst for gas-phase hydrogenolysis of glycerol. They obtained 94 % yield of 1,2-PDO at 478 K and 1.4 MPa H_2. The presence of chromium enhanced the C–C hydrogenolysis to ethanol and reduced the 1,2-PDO yield.

J. Zhou et al. [81] prepared supported Cu-containing bimetallic catalysts and studied the effect of different supports, metals, metal loading and impregnation sequences. An effect was observed between Cu and Ag when supported on γ-Al_2O_3. The addition of Ag resulted in an *in situ* reduction of CuO and also improved the dispersion of the Cu species on the support. This bimetallic catalyst system can be used directly without a reduction pre-treatment. A glycerol conversion of 27 % was obtained with 96 % selectivity to 1,2-PDO at 473 K with 1.5 MPa H_2 pressure in a batch reactor.

A. Bienholz et al. [82] investigated the hydrogenolysis of glycerol over CuO/ZnO catalysts which were prepared by the oxalate gel method and co-precipitation. The CuO/ZnO catalyst prepared by the oxalate gel method exhibited a much higher conversion than the catalyst prepared by the co-precipitation method (46 % compared to 17 %), but similar selectivities of 90 % were seen. The higher activity can be attributed to the higher surface area of the copper. In the presence of H_2O, the copper crystallites of the CuO/ZnO catalyst increased significantly, leading to a decrease in active surface area and a loss of activity.

C. Liang et al. [83] prepared and evaluated high surface area nanostructured Cu-Cr catalysts for the hydrogenolysis of glycerol. The reduced Cu-Cr catalysts showed significant catalytic activity and selectivity in glycerol hydrogenolysis. A 51 % glycerol conversion was obtained with a 96 % 1,2-PDO selectivity under 4.15 MPa H_2 at 483 K. The Cu-Cr catalysts with low Cu/Cr molar ratio gave high glycerol conversion, which is different from the conventional copper chromite catalysts.

1.6.3 Nickel-copper based catalysts

Understanding the mechanism of the cleavage of the C-C and C-O bonds which modulates the routes in the glycerol conversion (dehydration, dehydrogenation, and hydrogenolysis) is the key to control the selectivity to target products such as hydroxyacetone and lactic acid.

In a bifunctional catalyst, the metal species serves both hydrogenation and dehydrogenation functions in the whole reaction process [84, 85]. The cleavage of C-C bonds is proposed to occur on the metal species, while the cleavage of C-O occurs through dehydration on the acid sites [86]. Dehydrated species formed on acid sites can migrate to metal sites where they undergo hydrogenation-dehydrogenation reactions [87]. In this way, repeated cycling of dehydration and hydrogenation-dehydrogenation [87] in the presence of H_2 can lead to heavier alkanes over catalysts containing metals (e.g., Ni or Cu) and acidic supports (e.g., γ–Al_2O_3).

The replacement of noble metal catalysts with cheap and abundant metals is an important issue. Metals like nickel (Ni) and copper (Cu) are ideal candidates [88]. The Ni/γ-Al_2O_3 catalyst has ability for hydrogenation-dehydrogenation along with its acid properties constitute a determinant bifunctional property which is needed to obtain important secondary chemicals like hydroxyacetone, pyruvaldehyde and acetaldehyde [54].

The main disadvantage of supported Ni catalysts compared with noble metal catalysts arises because of the formation, diffusion and dissolution of carbon in the metal [89]. Ni promotes C-C bond cleavage, providing a source of carbon. The presence of defects in the crystalline structure or low coordination number surface sites, which can be numerous on small particles, may also lead to coke formation [90]. The carbon may be gasified, may encapsulate the surface or may dissolve in the Ni crystallite. So, during coking-based deactivation, carbon is deposited on the active site at the active site/gas

interface forming a layer called encapsulating carbon, which blocks reactant access. Encapsulating carbon causes catalyst deactivation either by blocking the catalyst pores or by complete encapsulation [91]. The dissolved carbon diffuses through the Ni to nucleate and precipitate at the rear of the crystallite. This continuing process leads to the formation of a carbon whisker, which lifts the Ni crystallite from the catalyst surface, and eventually results in fragmentation of the catalyst [91, 92]. At the gas/metal interface, carbon is in the form of a solute dissolved in Ni as a solvent, forming an unstable intermediate of surface nickel carbide (Ni_3C) [91]. There is some uncertainty as to whether Ni_3C is an intermediate in the process of dissolving carbon in Ni [93]. For Ni catalysts, it is believed that carbides are formed as short lived intermediates in the carbon dissolution process. If this is the case, then dissolution of carbon into Ni could be minimized if carbide formation could be avoided [89] since dissolution and precipitation could probably only occur via carbide formation [93, 94]. The deposition of carbon species may place the Ni crystallites in a new support environment; the subsequent change in metal-support interaction may induce changes in activity and selectivity properties.

Regeneration to remove the coke formed on the catalyst surface by oxidation of coke with O_2 or air is typically used in Industry [92, 95]. In air regeneration, oxygen reacts with the deposited carbon to burn it; a mixture of carbon oxides is produced, which could then require a reduction step before using the catalyst again [91]. Zhang and Amiridis [92] used a 16.4 % Ni/SiO_2 catalyst for methane cracking and air oxidation to regenerate the spent catalyst at 823 K. They reported that the catalyst was quickly and fully regenerated using air oxidation. Furthermore, XRD analysis showed that Ni oxide had been formed, requiring reduction of the catalyst before further use for methane cracking. Regarding the effect on catalyst texture, in air regeneration, local hot spots may form, affecting some active sites by cause sintering, decreasing the exposed Ni surface area [91]. Villacampa et al. [96] used a 3 % oxygen stream to fully regenerate a 30 % Ni/Al_2O_3 catalyst. They reported that the catalyst lost its activity after the first regeneration experiment. Villacampa et al. [96] attributed the loss of activity after regeneration with air to active site sintering due to the high temperature generated during oxidation of the deposited carbon.

The introduction of a second metal to the Ni catalyst systems may provide significant changes in the catalytic activity, selectivity and in the formation of coke as compared with the monometallic ones [97, 98]. This is the case for Ni-based bimetallic

catalysts containing Cu, which exhibit significantly different catalytic activity and selectivity compared to Ni monometallic catalysts [97-103]. In previous works [89, 104] were observed that the addition of Cu to Ni catalysts suppress both sintering of the active component and carbon formation on the methane steam reforming.

It is known that unlike Ni, the hydrogenolytic capacity of Cu to cleavage C-C bonds is poor [105-109] . However, Cu is an efficient catalyst for the cleavage of C-O bond, which can dramatically affect the product distribution in glycerol hydrogenolysis.

Ni-Cu is a good example of a bimetallic catalyst system in which the variation of the catalytic activity with composition depends markedly on the type of reaction, thus leading to substantial selectivity effects [20]. The different effects of Cu on Ni in the reaction routes of glycerol (dehydration, dehydrogenation, hydrogenolysis) may be rationalized from the different chemisorbed intermediates that could be involved [110]. The chemisorbed intermediate in hydrogenolysis is probably hydrogen-deficient organic specie which forms a number of bonds with the Ni metal atoms of the catalyst surface. The probability of finding a suitable array or multiple of active metal atoms to accommodate such an intermediate may greatly decrease when the Cu species are dispersed on the Ni catalyst surface. By contrast, the chemisorbed intermediate in the dehydrogenation presumably does not require a site consisting of a number of active metal atoms and it is therefore relatively less sensitive to coverage of the surface with Cu.

In glycerol hydrogenolysis the strength of bonding between the two carbon atoms in the chemisorbed intermediate might be expected. In view of the low ability of Cu relative to Ni to chemisorb a variety of organic compounds, it might reasonably be expected that the addition of Cu to Ni would decrease the strength of adsorption of organic species on the surface. Rupture of the C-C bond would then be inhibited and the deep hydrogenolysis towards CH_4 formation should then decrease.

1.7 Motivation

This research work wishes to contribute with the development of catalysts for the catalytic transformation of glycerol to high value-added chemicals. The attention of the present research is devoted to the glycerol hydrogenolysis over Ni based catalysts.

We want to emphasize the effect of the total number of exposed Ni atoms on the stability and product selectivity in the glycerol hydrogenolysis. The effect of addition of Cu to Ni catalyst is another issue of great interest in the present research work.

The general challenge in the hydrogenolysis of glycerol is the selective control of the cleavage of C-O over C-C bonds. The activity and selectivity of the supported metal catalysts are strongly influenced by the amount of metal employed, the size of the dispersed metal particles, metal–support interactions and the composition of the support [111].

The hydrogenolysis activity of the Group IB metals is much lower than those of Group VIII metals. This must affect the reaction routes in the catalytic transformation of glycerol. The main effect of Cu introduction to the Ni catalysts must be mirrored in the suppression of C-C bond linkage of the glycerol. Upon addition of Cu, dehydration route of glycerol must prevail.

Finally we wish to re-emphasize that the major interest of the present investigation in the glycerol hydrogenolysis with Ni and Ni-Cu catalysts is namely to understand the catalyst structure relationship with the catalytic performance.

1.8 References

[1] L. Prati, P. Spontoni, A. Gaiassi, Top. Catal. 52 (2009) 288-296.
[2] N. Dimitratos, J. A. Lopez-Sanchez, G.J. Hutchings, Top. Catal. 52 (2009) 258-268.
[3] K. Biernat, A. Malinowski, M. Gnat, in: Z. Fang (Ed.), Biofuels - Economy, Environment and Sustainability, 2013, pp. 123-172.
[4] Nature. 444 (2006) 669.
[5] M. Schlaf, Dalton Trans. (2006) 4645–4653.
[6] P. N. R. Vennestrøm, C. M. Osmundsen, C. H. Christensen, E. Taarning, Angew. Chem. Int. Ed. 50 (2011) 10502-10509.
[7] M. Pagliaro, M. Rossi, The Future of Glycerol, The Royal Society of Chemistry, Cambridge, UK, 2010.
[8] C.H. Zhou, J. N. Beltramini, Y. X.Fan, G.Q. Lu, Chem. Soc. Rev. 37 (2008) 527-549.
[9] A. Kazmi, J. Clark, Comprehensive Renewable Energy. 5 (2012) 395-409.
[10] Y. Zheng, X. Chen, Y. Shen, Chem. Rev. 108 (2008) 5253–5277.
[11] M. Goula, N.D. Charisiou, O.A. Bereketidou, World Bioenergy 2012: Conference & Exhibition on Biomass for Energy, Sweden, 2012.
[12] J. ten Dam, U. Hanefeld, ChemSusChem. 4 (2011) 1017– 1034.
[13] A. B. Leoneti, V. Aragão-Leoneti, S.V. Walter, Renewable Energy. 45 (2012) 138-145.
[14] B. N. Zope, D. D. Hibbitts, M. Neurock, R.J. Davis, Science. 330 (2010) 74-78.

[15] A. Villa, G. M. Veith, L. Prati, Angew. Chem. Int. Ed. 49 (2010) 4499-4502.
[16] S. H. Chai, H. P. Wang, Y. Liang, B.Q. Xu, Green Chem. 9 (2007) 1130.
[17] M. Stelmachowski, Ecol. Chem. Eng. S. 18 (2011) 9-30.
[18] T. Werpy, G. Petersen, Pacific Northwest National Laboratory (PNNL) and National Renewable Energy Laboratory (NREL), United States of America, 2004.
[19] A. M. Ruppert, K. Weinberg, R. Palkovits, Angew. Chem. Int. Ed. 51 (2012) 2564 – 2601.
[20] J.H. Sinfelt, Bimetallic catalysts: Discoveries, concepts, and applications, John Wiley & Sons, Inc, United States of America, 1931.
[21] T. Kurosaka, H. Maruyama, I. Naribayashi, Y. Sasaki, Catal. Commun. 9 (2008) 1360–1363.
[22] J. Feng, H. Fu, J. Wang, R. Li, H. Chen, X. Li, Catal. Commun. 9 (2008) 1458–1464.
[23] A. Corma, G. W. Huber, L. Sauvanaud, P. O'Connor, J. Catal. 257 (2008) 163-171.
[24] C. Zhao, I.E. Wachs, Catal. Today. 118 (2006) 332-343.
[25] S. Vollenweider, C. Lacroix, Appl. Microbiol. Biotechnol. 64 (2004) 16.
[26] T.M. Che, US, 1987.
[27] Y. Nakagawa, Y. Shinmi, S. Koso, K. Tomishige, J. Catal. 272 (2010) 191-194.
[28] J. Chaminand, L. Djakovitch, P. Gallezot, P. Marion, C. Pinel, C. Rosier, Green Chem. 6 (2004) 359-361.
[29] T. Miyazawa, Y. Kusunoki, K. Kunimori, K. Tomishige, J. Catal. 240 (2006) 213-221.
[30] T. Miyazawa, S. Koso, K. Kunimori, K. Tomishige, Appl. Catal., A. 329 (2007) 30-35.
[31] M. Balaraju, V. Rekha, P.S.S. Prasad, B.L.A.P. Devi, R.B.N. Prasad, N. Lingaiah, Appl. Catal., A. 354 (2009) 82-87.
[32] L. Gong, Y. Lu, Y. Ding, R. Lin, J. Li, W. Dong, T. Wang, W. Chen, Chin. J. Catal 30 (2009) 1189–1191.
[33] I. Furikado, T. Miyazawa, S. Koso, A. Shimao, K. Kunimori, K. Tomishige, Green Chem. 9 (2007) 582-588.
[34] A. Perosa, P. Tundo, Ind. Eng. Chem. Res. 44 (2005) 8535-8537.
[35] L. B. Råberg, M. B. Jensen, U. Olsbye, C. Daniel, S. Haag, C. Mirodatos, A.O. Sjåstad, J. Catal. 249 (2007) 250-260.
[36] L. Huang, Y.-L. Zhu, H.-Y. Zheng, Y.-W. Li, Z.-Y. Zeng, J. Chem. Technol. Biotechnol. 83 (2008) 1670–1675.
[37] M. Akiyama, S. Sato, R. Takahashi, K. Inui, M. Yokota, Appl. Catal., A. 371 (2009) 60-66.
[38] Y. T. Kim, K-D. Jung, E.D. Park, Appl. Catal. B. 107 (2011) 177– 187.
[39] A. K. Kinage, P. P. Upare, P. Kasinathan, Y. K. Hwang, J.-S. Chang, Catal. Commun. 11 (2010) 620–623.
[40] S. Sato, M. Akiyama, R. Takahashi, T. Hara, K. Inui, M. Yokota, Appl. Catal. A. 347 (2008) 186-191.
[41] S. J. S. Vasconcelos, C. L. Lima, J. M. Filho, A. C. Oliveira, E. B. Barros, F. F. de Sousa, M. G.C. Rocha, P. Bargiela, A.C. Oliveira, Chem. Eng. J. 168 (2011) 656-664.
[42] W.Suprun, M. Lutecki, T. Haber, H. Papp, J. Mol. Catal. A: Chem. 309 (2009) 71-78.
[43] H. Atia, U. Armbruster, A. Martin, J. Catal. 258 (2008) 71-82.

[44] Y. Feng, H. Yin, A. Wang, L. Shen, L. Yu, T. Jiang, Chem. Eng. J. . 168 (2011) 403–412.
[45] M.A. Dasari, P.P. Kiatsimkul, W. R. Sutterlin, G.J. Suppes, Appl. Catal., A. 281 (2005) 225-231.
[46] S. Wang, H. Liu, Catal. Lett. 117 (2007) 62-67.
[47] Z. Huang, F. Cui, H. Kang, J. Chen, X. Zhang, C. Xia, Chem. Mater. 20 (2008) 5090–5099.
[48] C. Montassier, J. C. Ménézo, L. C. Hoang, C. Renaud, J. Barbier, J. Mol. Catal. . 70 (1991) 99-110
[49] E. P. Maris, R.J. Davis, J. Catal. 249 (2007) 328–337.
[50] J. Chaminand, L. Djakovitch, P. Gallezot, P. Marion, C. Pinel, C. Rosier, Green Chem. 6 (2004) 359–361.
[51] I. Gandarias, P.L. Arias, J. Requies, M.B. Güemez, J.L.G. Fierro, Appl. Catal. B. 97 (2010) 248–256.
[52] M. Akizuki, Y. Oshima, The University of Tokyo Japan.
[53] L. Ma, D. He, Z. Li, Catal. Commun. 9 (2008) 2489–2495.
[54] Y. Nakagawa, K. Tomishige, Catal. Sci. Technol. 1 (2011) 179–190.
[55] J. Wang, S. Shen, B. Li, H. Lin, Y. Yuan, Chem. Lett. 38 (2009) 572-573.
[56] T. Miyazawa, S. Koso, K. Kunimori, K. Tomishige, Appl. Catal. A. 318 (2007) 244-251.
[57] T. Miyazawa, S. Koso, K. Kunimori, K. Tomishige, Appl. Catal. A 329 (2007) 30–35.
[58] E.H. E.S. Vasiliadou, I.A. Vasalos, A.A. Lemonidou, Applied Catalysis B: Environmental 92 (2009) 90-99.
[59] J. Feng, J. Wang, Y. Zhou, H. Fu, H. Chen, X. Li, Chem. Lett. 36 (2007) 1274-1275.
[60] E. P. Maris, W. C. Ketchie, M. Murayama, R.J. Davis, J. Catal. 251 (2007) 281–294.
[61] Z. Yuan, P. Wu, J. Gao, X. Lu, Z. Hou, X. Zheng, Catal Lett. 130 (2009) 261-265.
[62] F. Vila, M. López Granados, M. Ojeda, J.L.G. Fierro, R. Mariscal, Catal. Today. 187 (2012) 122-128.
[63] W. Yu, J. Zhao, H. Ma, H. Miao, Q. Song, J. Xu, Appl. Catal., A. 383 (2010) 73–78.
[64] Q. Liu, X. Guo, Y. Li, W. Shen, Langmuir. 25 (2009) 6425-6430.
[65] L. C. Meher, R. Gopinath, S. N. Naik, A.K. Dalai, Ind. Eng. Chem. Res. 48 (2009) 1840–1846.
[66] L. Guo, J. Zhou, J. Mao, X. Guo, S. Zhang, Appl. Catal. A. 367 (2009) 93-98.
[67] R. B. Mane, A. M. Hengne, A. A. Ghalwadkar, S. Vijayanand, P. H. Mohite, H. S. Potdar, C.V. Rode, Catal. Lett. 135 (2010) 141-147.
[68] A. Brandner, K. Lehnert, A. Bienholz, M. Lucas, P. Claus, Top. Catal. 52 (2009) 278–287.
[69] Z. Yuan, J. Wang, L. Wang, W. Xie, P. Chen, Z. Hou, X. Zheng, Bioresour. Technol. . 101 (2010) 7088–7092.
[70] S. R. Schmidt, S. K. Tanielyan, N. Marin, G. Alvez, R.L. Augustine, Top. Catal. 53 (2010) 1214–1216.
[71] W. Yu, J. Zhao, H. Ma, H. Miao, Q. Song, J. Xu, Appl. Catal. A. 383 (2010) 73-78.
[72] N. Ueda, Y. Nakagawa, K. Tomishige, Chem. Lett. 39 (2010) 506-507.

[73] J. H. Sinfelt, J. L. Carter, D. J. C. Yates, J. Catal. 24 (1972) 283–296.
[74] J.H. Sinfelt, Catal. Rev. 3 (1969) 175-205.
[75] J.A. Dalmon, J. Catal. 60 (1971) 325-334.
[76] P. K. Bajpai, N. N. Bakhshi, D.-C. Liu, J.F.C. Mathews, J. Chem. Eng. 60 (1982) 613.
[77] K. C. Khulbe, R.S. Mann, Catal. Rev. Sci. Eng. 24 (1982) 311.
[78] N. Shah, D. Panjala, G. Huffman, Energy Fuels. 15 (2001) 1528.
[79] M. Balaraju, V. Rekha, P. S. Sai Prasad, R. B. N. Prasad, N. Lingaiah, Catal. Lett. 126 (2008) 119-124.
[80] Z. Huang, F. Cui, H. Kang, J. Chen, C. Xia, Appl. Catal. A. 366 (2009) 288-298.
[81] J. Zhou, L. Guo, X. Guo, J. Mao, S. Zhang, Green Chem. 12 (2010) 1835-1843.
[82] A. Bienholz, F. Schwab, P. Claus, Green Chem. 12 (2010) 290-295.
[83] C. Liang, Z. Ma, L. Ding, J. Qiu, Catal. Lett. 130 (2009) 169-176.
[84] L. Jun-Cheng, X. Lan, X. Feng, W. Zhan-Wen, W. Fei, Appl. Surf. Sci. 253 (2006) 766–770.
[85] C.V. Rode, R.B. Mane, A.S. Potdar, P.B. Patil, P.S. Niphadkar, P.N. Joshi, Catal. Today. 190 (2012) 31-37.
[86] Y. Shinmi, S. Koso, T. Kubota, Y. Nakagawa, K. Tomishige, Appl. Catal. B. 94 (2010) 318–326.
[87] G. W. Huber, J.A. Dumesic, Catal. Today. 111 (2006) 119-132.
[88] K. Shimizu, K. Kon, K. Shimura, S.S.M.A. Hakim, J. Catal. 300 (2013) 242–250.
[89] D.L. Trimm, Catalysis Today 37 (1997) 233-238
[90] J. Wei, E. Iglesia, J. Catal. 224 (2004) 370-383.
[91] A. M. Amin, E. Croiset, W. Epling, Int. J. Hydrogen Energy 36 (2011) 2904-2935.
[92] T. Zhang, M.D. Amiridis, Appl. Catal. A. 167 (1998) 161-172.
[93] D.L. Trimm, Catal. Today. 49 (1999) 3-10.
[94] F. Frusteri, L. Spadaro, F. Arena, A. Chuvilin, Carbon. 40 (2002) 1063-1070.
[95] A.S.A. Al-Fatesh, A.A. Ibrahim, A.H. Fakeeha, A.E. Abasaeed, M.R.H. Siddiqui, J. Ind. Eng. Chem. 17 (2011) 479–483.
[96] J.I. Villacampa, C. Royo, E. Romeo, J.A. Montoya, P. Del Angel, A. Monzón, Appl. Catal. A. 252 (2003) 363–383.
[97] P. Li, J.Liu, N.Nag, P.A.Crozier, J. Catal. 262 (2009) 73-82.
[98] F. Bonet, S. Grugeon, L. Dupont, R. Herrera Urbina, C. Guéry, J.M. Tarascon, J. Solid State Chem. 172 (2003) 111–115.
[99] M. Kang, M.W. Song, T.W. Kim, K.L. Kim, Can. J. Chem. Eng. . 80 (2002) 63-70.
[100] T-J. Huang, S.-Y. Jhao, Appl. Catal. A. 302 (2006) 325-332.
[101] R.J. Best, W.W. Russell, J. Am. Chem. Soc. 76 (1954) 838.
[102] M.K. Gharpurey, P.H. Emmett, J. Phys. Chem. 65 (1961) 1182.
[103] Y. Liu, D.Z. Liu, Int. J. Hydrogen Energy. 24 (1999) 351.
[104] C.A. Bernardo, I. Alstrup, J.R. Rostrup-Nielsen. 96 (1985) 517-534.
[105] W.M.H. Sachtler, G.J.H. Dorgelo, R. Jongepier, J. Catal. 4 (1965) 100-102.
[106] T. Takeuchi, O. Takayasu, S. Tanada, J. Catal. 54 (1978) 197-206.
[107] S.D. Robertson, S.C. Kloet, W.M.H. Sachtler, J. Catal. 32 (1975) 234-248.
[108] P.E.C. Franken, V. Ponec, J. Catal. 42 (1976) 398-407.
[109] A. R. Naghash, Z. Xu, T.H. Etsell, Chem. Mater. 17 (2005) 815-821.
[110] D. G. Lahr, B.H. Shanks, Ind. Eng. Chem. Res. 42 (2003) 5467-5472.
[111] I. Czekaj, F. Loviat, F. Raimondi, J. Wambach, S. Biollaz, A. Wokaun, Appl. Catal. A 329 (2007) 68-78.

Chapter 2

Experimental

2.1 Introduction

This chapter focuses on the description of the experimental methods employed in this research work. A description of the catalyst preparation and characterization techniques is presented. Finally, it is shown a description of the set-up catalytic system employed for the hydrogenolysis of glycerol.

2.2 Catalyst preparation

2.2.1 Ni/γ-Al_2O_3 catalysts

Commercial γ-Al_2O_3 was purchased from Degussa and it was calcined at 463 K for 4 h before use. The samples containing 10 wt% of Ni were prepared by incipient wetness impregnation of γ-Al_2O_3 with a 4.8 M $Ni(NO_3)_2.6H_2O$ (Aldrich, 99.999%) aqueous solution. After impregnation, the sample was dried at 373 K for 12 h and then reduced at different temperatures (T_{red}= 623, 723, 823, 923, 993 and 1073 K) in a flow of 20 ml/min with pure H_2 for 4 h. Each resultant material was labeled as NiT_{red} (for instance Ni623).

2.2.2 Ni-Cu/γ-Al_2O_3 catalysts

Commercial γ-Al_2O_3 was purchased from Degussa and it was calcined at 463 K for 4 h before use. The Ni-Cu catalysts containing 10 wt% of total metal loading were prepared by wet co-impregnation of γ-Al_2O_3 with an aqueous solution containing the $Ni(NO_3)_2{\cdot}6H_2O$ and $Cu(NO_3)_2{\cdot}6H_2O$ precursors (Aldrich, 99.999%), which were mixed to obtain the following Ni:Cu molar ratios: 8/1, 4/1, 2/1, 1/1, 1/2, 1/4 and 1/8. It was also prepared the monometallic Ni sample and the monometallic Cu sample. After impregnation, each sample was dried by rotavapor at 373 K for 12 h and it was then reduced at 723 K in a flow of 20 ml/min with pure H_2 for 4 h. Each resultant material was labeled as NiCu atomic ratio (for instance NiCu81, NiCu41, and so on).

2.3 Catalyst characterization

2.3.1 Thermogravimetric analysis (TGA)

The decomposition temperature of the precursors ($Ni(NO_3)_2{\cdot}6H_2O$ and $Cu(NO_3)_2{\cdot}6H_2O$) of the catalysts was investigated by TGA-MS over dried samples after

(co)-impregnation of the Ni and Cu precursors aqueous solution. TGA analyses were recorded in a Sensys evo apparatus from room temperature (RT) to 1173 K, at a heating rate of 10 K/min under a flow of 5 % H_2/Ar. The off-gas was simultaneously analyzed with a Pfeiffer Vacuum QME 220 mass spectrometer (MS).

2.3.2 Temperature programmed reduction (TPR)

TPR determines the number of reducible species present in the catalyst and reveals the temperature at which reduction occurs. An important aspect of TPR analysis is that the sample need not have any special characteristic other than containing reducible metals. The TPR analysis begins by flowing analysis gas (typically hydrogen in an inert carrier gas such as nitrogen or argon) over the sample, usually starting at ambient temperature. While the gas is flowing, the temperature of the sample is increased linearly with time and the consumption of H_2 by adsorption/reaction is monitored. Changes in the concentration of the gas mixture are determined. This information yields the H_2 uptake volume.

The TPR experiments were performed in a ThermoFinnigan (TPD/R/O 1100) apparatus equipped with a thermal conductivity detector (TCD). The quartz tubular reactor containing the sample was placed in the oven for catalyst activation and pre-treated with Ar flowing at 20 ml/min at RT during 5 min. Then, the reactor was changed to the oven for analysis, which was carried out using a 5 % H_2/Ar gas flowing at 50 ml/min by heating from RT to 1173 K with a heating rate of 10 K/min. The evolved species during TPR were monitored by an on-line mass spectrometer Pfeiffer Vacuum QME 220. Soda lime was used as trap in order to stop NO_x gases in the carrier gas before they enter the detector.

2.3.3 Temperature programmed desorption (TPD)

TPD analyses determine the number, type, and strength of active sites available on the surface of a catalyst from measurement of the amount of gas desorbed at various temperatures.

TPD of NH_3 was used to determine the total acidity of the catalysts. The TPD-NH_3 analyses were carried out on a Micromeritics AutoChem II equipped with a TCD detector. Each sample (0.05–0.1 g) was loaded into the sample tube and pretreated by flowing Ar at 353 K during 1 h, and then cooled to RT. The sample was then treated with NH_3 flow (5 % NH_3 in He) at RT for 1 h. The NH_3 desorption was measured by heating the sample from

RT to 1073 K at a rate of 5 K/min in He flow. A flow rate of 50 ml/min was employed for all the gases. The total number of acid sites was calculated by using pulses of a known amount of NH_3.

2.3.4 N_2 -Physisorption

The specific surface areas, cumulative pore volumes and average pore diameters of the samples were measured by the BET method using N_2 adsorption/desorption at 77 K in a Quadrasorb SI, from Quantachrome Instrument. The samples were placed into sample cells with an external diameter of 9 mm (7 mm internal diameter). Each sample was degassed under vacuum at 393 K for 10 h in a Quantachrome FloVac Degasser. Then, the degassed samples were attached to the QUADRASORB *SI* and placed the Dewar flasks containing liquid nitrogen (as coolant) on the lift-drive bases. Nitrogen was used as adsorbate gas for the analysis. The BET specific surface area was calculated from the range P/P_0 = 0.05–0.35 in the adsorption branch while the pore size distribution was calculated from the desorption branch.

2.3.5 H_2- Chemisorption

H_2-chemisorption was performed to determine the total area of the exposed metallic Ni atoms [1]. The analysis was performed using a conventional static method in a Micromeritics ASAP 2010 instrument. The samples were heated in flowing He at 400 K for 1 h; then the He flow was replaced by H_2 flow and the temperature was increased to the correspondent reduction temperature. At this temperature the samples were reduced for 2 h and subsequently out-gassed for 30 min. Finally, the samples were cooled to 310 K and evacuated at 310 K for 30 min. The hydrogen adsorption isotherm was recorded at 310 K. After evacuation at 310 K for 10 min, a second H_2 isotherm was obtained. The chemisorbed H_2 uptake was obtained by extrapolating to zero pressure the linear portion of the isotherm. The number of exposed Ni atoms was calculated assuming spherical particles, the stoichiometry factor of 1 atomic chemisorbed hydrogen per surface Ni atom, a Ni surface area of 0.0649 nm^2 per Ni atom and a Ni density of 8.9 g/cm^3 [1].

2.3.6 Transmission Electron Microscopy (TEM)

Particle size measurements should ideally be performed on a large number of particles on several TEM views taken on different zones of a specimen grid and on several grids corresponding to different samplings of the catalyst batch. Particle size distribution can be established by counting about 1000 particles, either monomodal or bimodal, is narrow enough [2].

In this investigation the TEM study was carried out in a JEOL JEM-2100 instrument (Figure 2.1) operating at an accelerating voltage of 100 kV. The samples were prepared by dispersing the as-prepared catalysts in alcohol and then dropping the suspension on a standard 3 mm holey carbon-coated copper grid and letting the alcohol evaporate at RT. In addition, high-resolution transmission electron microscopy (HRTEM) was carried out for some samples with a JEOL 2010F instrument (from Institut de Tècniques Energètiques in the Universitat Politècnica de Catalunya) equipped with a field emission source with high resolution in 200 kV. The point-to-point resolution was 0.19 nm and the resolution between lines was 0.14 nm.

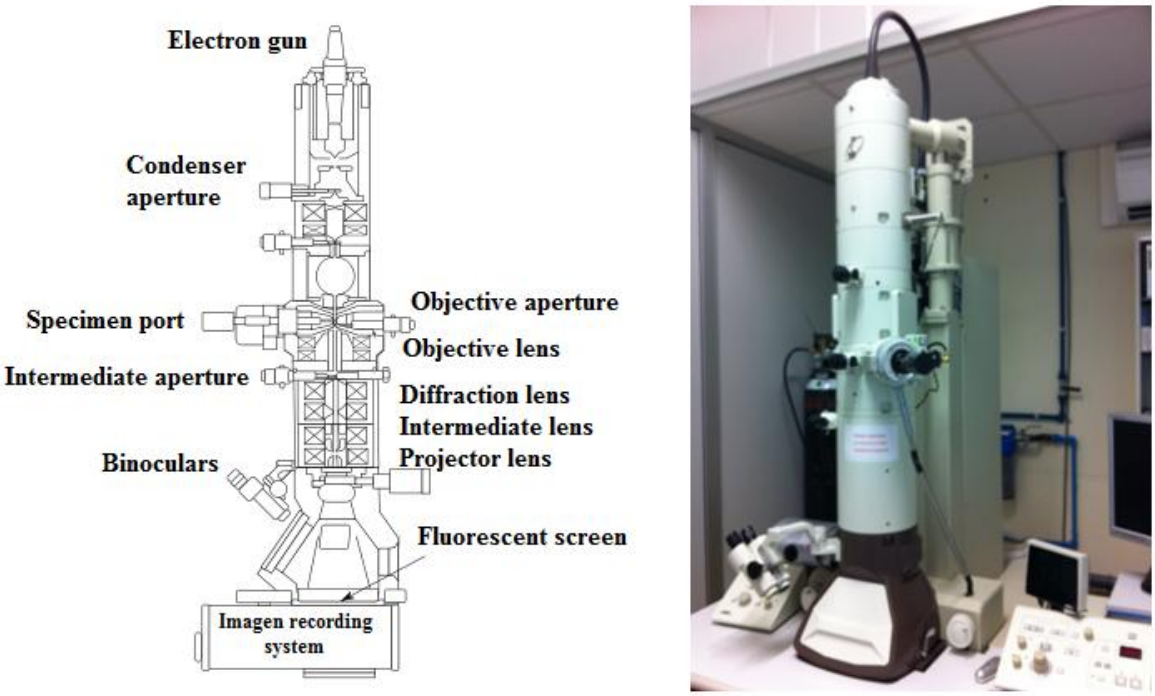

Figure 2.1 JEOL JEM-2100 instrument

2.3.7 X-Ray Diffraction (XRD)

X-rays have wavelengths in the angstrom range, are sufficiently energetic to penetrate solids, and are well suited to probe their internal structure. XRD is a basic tool used to identify bulk phases, to monitor the kinetics of bulk transformations, and to estimate the size of small crystallites. X-ray diffraction is the elastic scattering of X-ray photons by atoms in a periodic lattice. The scattered monochromatic X-rays that are in phase give constructive interference. Diffraction of X-rays by crystal planes allows one to derive lattice spacings by using the Bragg relation (Eq. 2.1), where λ is the wavelength of the X-rays, d is the distance between two lattice planes, θ is the angle between the incoming X-rays and the normal to the reflecting lattice plane, and n is an integer called the order of the reflection [3].

$$n\lambda = 2d\sin\theta; n = 1,2,..... \quad \text{(Eq. 2.1)}$$

If one measures the angles under which constructively interfering X-rays leave the crystal, the Bragg relation gives the corresponding lattice spacings, which are characteristic of a given material. The XRD patterns of a powdered sample is measured with a stationary X-ray source (usually Cu Kα) and a movable detector, which scans the intensity of the diffracted radiation as a function of the angle 2θ between the incoming and the diffracted beams. When working with powdered samples, an image of diffraction lines occurs because a small fraction of the powder particles will be oriented such that by chance a certain crystal plane is at the right angle θ with the incident beam for constructive interference [3].

A relationship between the crystal size and the width of diffraction lines was already recognized by Scherrer in 1918. Scherrer equation (Eq. 2.2) was developed to calculate the crystallite size (L) by XRD radiation of wavelength λ (nm) from measuring full width at half maximum of peaks (β) in radian located at any 2θ in the pattern. Shape factor of K can be 0.62–2.08 and is usually taken as about 0.89 [4].

$$L = \frac{K\lambda}{\beta\cos\theta} \quad \text{(Eq. 2.2)}$$

Since the method rests on the analysis of X-ray diffraction lines, it is restricted to the measurement of the size of crystalline particles. Therefore, XRD can give some information on the dispersion of a supported catalyst only if it is in the form of a separate crystalline phase.

The XRD analysis of the Ni based materials was recorded using a Bruker-AXS D8-Discover diffractometer (Figure 2.2) with parallel incident beam (Göble mirror) and vertical θ-θ goniometer, XYZ motorized stage mounted on an Eulerian cradle, diffracted-beam Soller slits, a 0.2 º receiving lit and a scintillation counter as a detector. The angular 2θ-diffraction range was between 5º and 90º. Spectra were collected with an angular step of 0.05 º at 3 s per step and sample rotation. Cu Kα radiation (λ=1.54056 Å) was obtained from a copper X-ray tube operated at 40 kV and 30 mA.

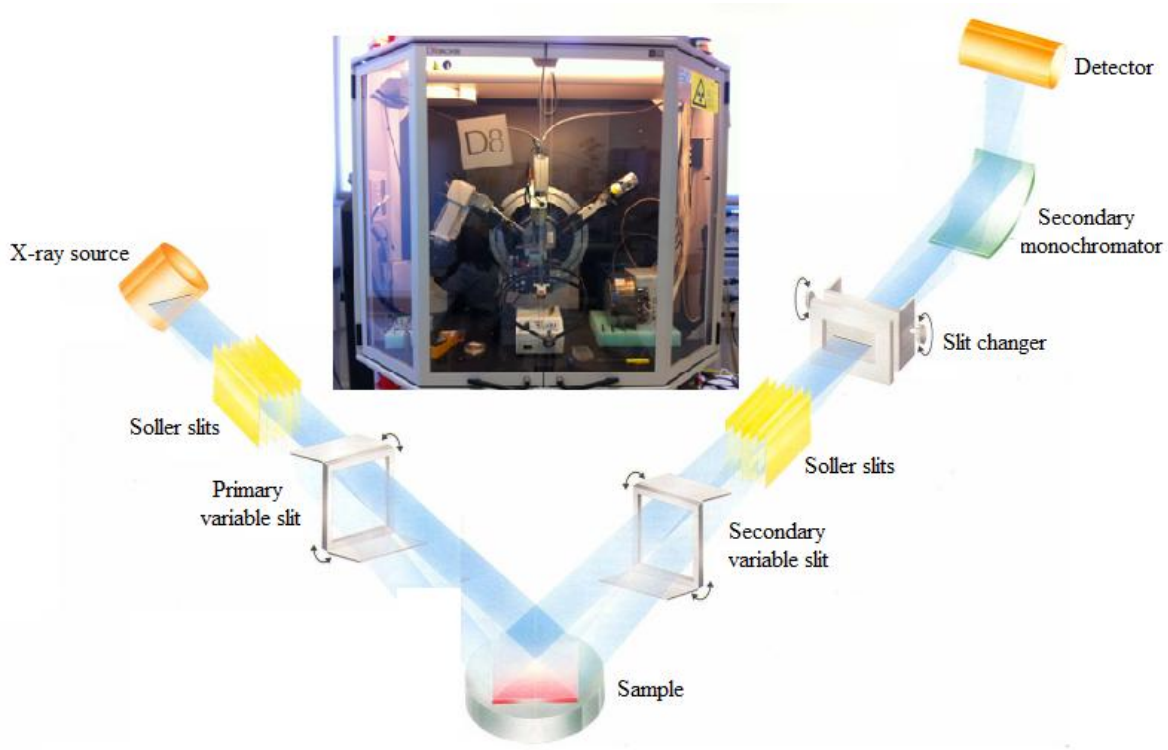

Figure 2.2 Diagram of X-ray diffractometer

For some of the samples, the XRD measurements were made using a Siemens D5000 diffractometer (Bragg-Bentano for focusing geometry and vertical θ-θ goniometer) fitted with a curved graphite diffracted-beam monochromator, incident and diffracted-beam Soller slits, a 0.06 º receiving slit and scintillation counter as detector. The angular

2θ-diffraction range was between 3º and 60º. The samples were dispersed on a Si (510) sample holder. The data were collected with an angular step of 0.03º at 5 s per step and sample rotation. Cu Kα radiation (λ=1.54056 Å) was obtained from a copper X-ray tube operated at 40 kV and 30 mA.

2.3.8 XRD at European Synchrotron Radiation Facility (ESRF)

A great advantage is that X-rays have considerable penetrating power, such that XRD can be used to study catalysts under *in situ* conditions. Using synchrotron radiation as a source of XRD has the following primary advantages [3, 5]:

1. High intensity of the radiation gives better signal-to-noise ratio (intensity is six orders of magnitude better than the conventional tubes).
2. Collection time is significantly shorter (in seconds compared to hours in conventional tubes).
3. It is easy to vary the wavelength of X-rays (than the conventional X-ray tubes which has definite wavelength).
4. A phenomenon by which the scattering efficiency of an element decreases if the energy of the radiation is close to an absorption edge.

Such advantages can lead to identification of broader peaks from smaller particles with better accuracy. More precise *in situ* studies and distinguishing diffraction patterns of the supported particles from that of the support can also be observed [5].

In this investigation *in situ* X-ray diffraction study was carried out at the beam line BM25A of the European Synchrotron Radiation Facility (ESRF, Grenoble, France), experiment MA-1525. In the Figure 2.3 is shown the experimental set-up.

The synchrotron radiation at the ESRF is emitted by very high energy electrons moving inside a ring and consists essentially of X-rays and serves mainly to study the atomic and molecular structure of matter. Samples in pellet shape (1.0 cm diameter and 0.25 cm thickness) were placed in a cell reactor (SPECAC Brillant Spectroscopy) to be analyzed in transmission mode (2×2 mm of beam size). The diffracted X-rays were recorded on an x-axis motorized CCD detector (charge-coupled device) at 34 cm from the sample. The X-ray wavelength used was 0.6199 Å (20 keV) and the Bragg angle was scanned continuously in the range 2θ = 2.2°–22°. The exposition time for the CCD detector

was of 300 s. Approximately 100 mg of the dried sample with $Ni(NO_3)_2 \cdot 6H_2O$ precursor impregnated over γ-Al_2O_3 was placed in a metallic sample holder. The CCD images (ca. 68 scans) were acquired *in situ* while the sample was heated in a 50 ml/min H_2 stream (5 % H_2/He) from 310 K to 1000 K at a rate of 2.5 K/min. Each CCD image was converted into conventional X-ray diffractograms by azimuthal integration (X-ray Oriented Programs, XOP 2.3 Software). Prior to each analysis, the CCD was calibrated by analyzing α-Al_2O_3 (SRM 676) prepared in the same conditions. This analysis was also done for the $Cu(NO_3)_2 \cdot 6H_2O$ precursor impregnated over γ-Al_2O_3.

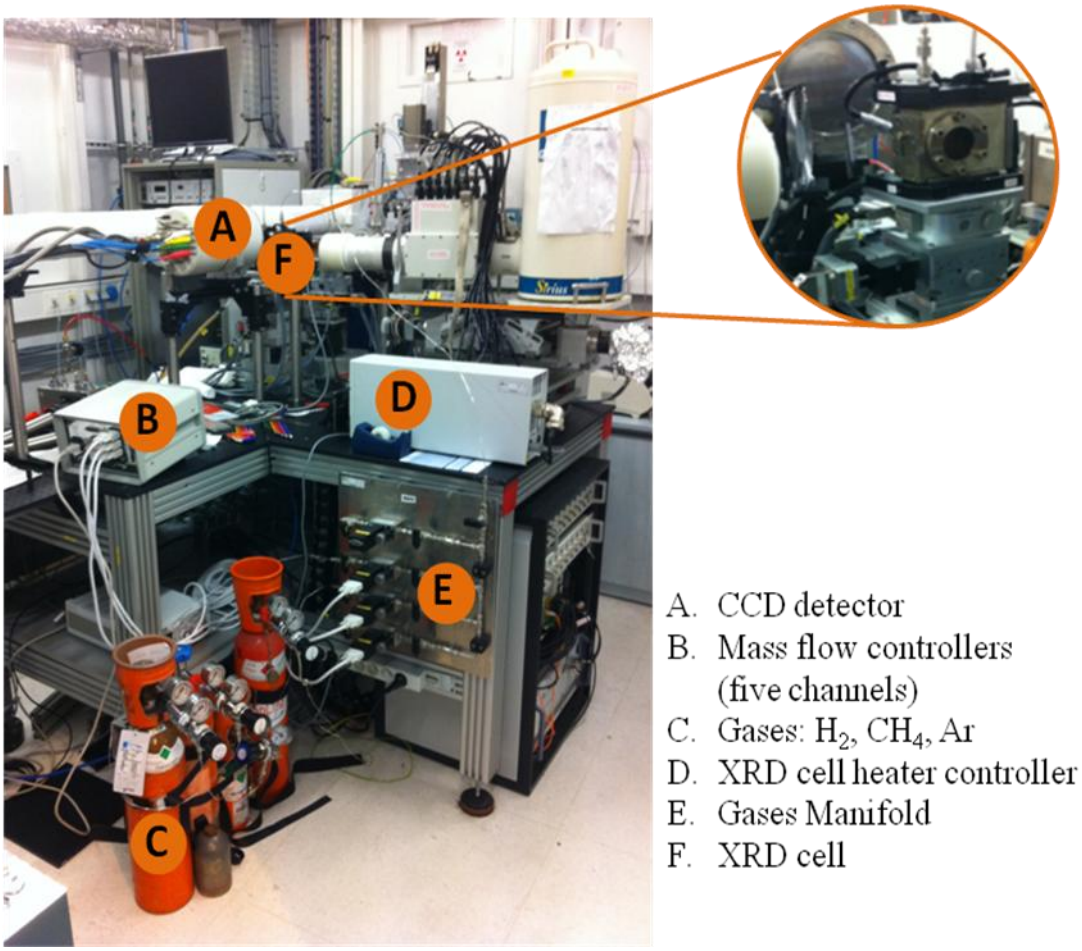

Figure 2.3 Experimental set-up used for *in situ* XRD

2.3.9 X-ray Absorption Spectroscopy (XAS)

The X-ray absorption spectroscopy (XAS) has been proven successful in structure determination for a vast number of systems. X-rays absorption spectroscopies are essentially synchrotron-based techniques. In an X-ray absorption experiment, a sample

of interest is bombarded with X-ray of definite energy. In an actual XAS experiment there are millions of X-rays being absorbed by millions of atoms. When X-rays are absorbed by the atoms occur the excitation or ejection of a core electron. The number of X-rays transmitted (I_t) through a sample is given by the intensity of incident X-rays on the sample (I_0) decreased exponentially by the thickness of the sample (x) and the absorption coefficient (μ) (Lambert-Beer law):

$$I_t(E)=I_0(E)e^{-\mu(E)x} \qquad \text{(Eq. 2.3)}$$

The X-ray absorption coefficient (μ) is the probability for an X-ray to be absorbed by a sample. The μ coefficient is a function of the incident X-ray energy. The probability for absorption increases sharply when the incident X-ray energy equals to the energy required to excite an electron to an unoccupied electron orbital. These steps in the absorption coefficient are termed absorption edges.

For convenient XAS interpretation two regions are often separated: (i) X-ray absorption near edge spectroscopy (XANES) and (ii) extended X-ray absorption fine structure (EXAFS). They differ in the energy of the final electronic state sampled, which is limited to a maximum of about 40 eV–50 eV for XANES and above that point for EXAFS. Figure 2.4 gives an example of an XAS for NiO. Each element has a specific set of absorption edges at the binding energies of its electrons.

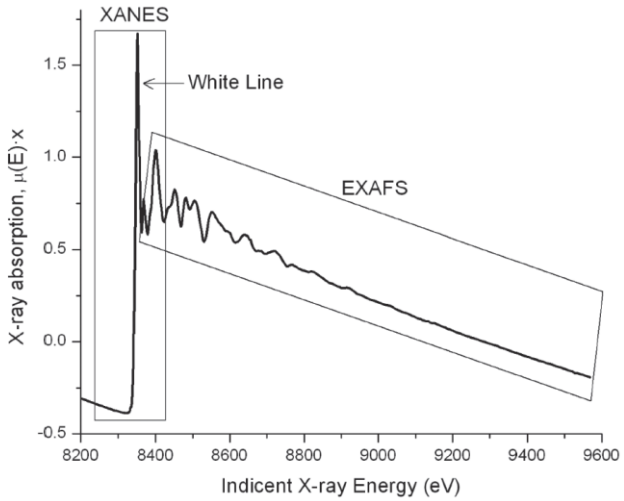

Figure 2.4 The X-ray absorption spectrum of NiO with the XANES region, EXAFS region and while line noted [6]

If an X-rays ejects an electron from an atom (photoelectron), the electron wave can scatter off of nearby atoms returning the original absorbing atom. Interferences between outgoing scattering and incoming backscattering waves result in low frequency oscillations between 50 eV and 100 eV above the absorption edge. These oscillations constitute EXAFS and are of interest as they contain structural and chemical information specific to the scattering atomic shells [7]. In fact, the ejected photoelectron acts as probe of the surrounding environment in a manner similar to electron scattering.

The experimental set-up for XAS used in this work is shown in Figure 2.5.

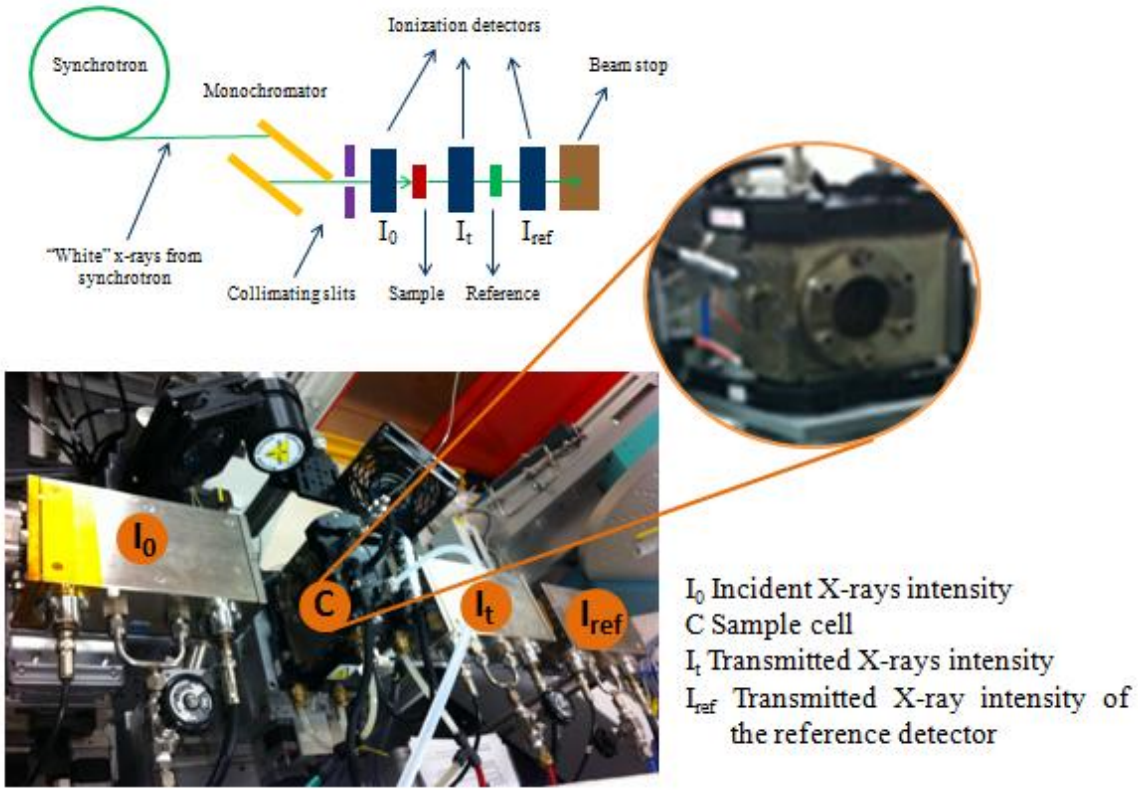

Figure 2.5 Experimental set-up used for XAS analyses

In this investigation, XAS spectra at the Ni K-edge (8,333 eV) and Cu K-edge (8,980 eV) for impregnated samples were measured at the DXAS beamline of the Brazilian Synchrotron Light Laboratory (LNLS, Campinas, Brazil) and at the BM25A beamline of the ESRF.

The sample was first crushed and sieved to particle sizes smaller than 20 μm. A self-supported pellet (60.0 mg of catalyst diluted in 60.0 mg of boron nitride) was prepared and placed inside of the cell.

At the LNLS the cell used was a tubular quartz reactor (20 mm ID and 440 mm X-ray path length), equipped with kapton™ refrigerated windows. XAS spectra were acquired during *in situ* reduction of the sample using 5 % H_2 in He, flowing at 100 ml/min, with heating at a rate of 10 K/min from RT to 973 K.

At the ESRF, the samples were loaded into a cell reactor (SPECAC Brillant Spectroscopy), and they were exposed to a flow of pure H_2 (5 ml/min), while the XAS measurements were taken at six temperatures (RT, 373 K, 473 K, 573, 648 K, and 723 K). The temperature was monitored with a chromel/alumel thermocouple mounted directly on the sample stage.

The intensity of the incident beam was measured with a 20-cm-long ion chamber filled with pure N_2. A 20-cm-long ion chamber was filled with a 60 % Ar/40 % N_2 mixture and placed after the sample to measure the transmitted beam intensity (I_t). A Si(110) crystal was used as a monochromator with a 4×2 mm^2 (H×V) slit. Spectral resolution was about $1x10^{-4}$ eV. The thickness of the samples was adjusted so that the edge jump was 1.0. Pre-edge data were collected in the range of 8200 eV to 8318.6 eV with steps of 10 eV. A step size of 0.05 $Å^{-1}$ was used in the EXAFS region.

The calibration measurements were made with another 20-cm-long Ar-filled ion chamber placed after the standards Ni foil and Cu foil. XAS of the reference compounds, NiO, CuO and Cu_2O, were also recorded under the same conditions. Linear combination analysis was used to find the relative amount of the constituents.

2.3.10 X-ray Photoelectron Spectroscopy (XPS)

Photo emission from solids is one of the methods that can be advantageously used for the characterization of solid substrates especially catalysts and their surfaces. The basic concept of photoelectric effect is that irradiated surfaces eject electrons which will carry information of the surface from where it is being ejected. This forms the basis of the photoelectron spectroscopy [5].

Photoelectron spectroscopy uses monochromatic sources of radiation, the most commonly employed X-ray sources are Mg-Kα (hv = 1253.6 eV) and Al-Kα (hv = 1486.6

eV). In XPS, the photon is absorbed by an atom in a molecule leading to ionization and the emission of a core (inner shell) electron. The kinetic energy distribution of the emitted photoelectrons can be measured using any appropriate electron energy analyzer and a photoelectron spectrum can thus be recorded. The binding energy (BE) of the electron is the difference in energy between the ionized and neutral atoms, for each and every element, there will be a characteristic binding energy associated with each core atomic orbital i.e, each element will give rise to a characteristic set of peaks in the photoelectron spectrum at kinetic energies determined from the photon energy and the respective binding energies. The presence of peaks at particular energies therefore indicates the presence of a specific element in the sample under study. Furthermore, the intensity of the peaks is related to the concentration of the element within the sampled region [5].

XPS is a surface technique as the mean free path of photoelectrons is often the order of a few nanometers in a solid. Electrons originating further below the surface suffer energy loss through collisions and may not even escape the surface. XPS analysis between 2–10 atomic layers, provides a quantitative analysis of the surface composition, the identification of all elements except Hydrogen and Helium present at concentrations greater than 0.1 atomic percent, molecular environment (Oxidation state, bonding with other atoms), etc [8].

In this investigation, the samples for XPS analysis were sent to the Institut de Tècniques Energètiques in the Universitat Politècnica de Catalunya to be analyzed. The XPS spectra were acquired in a VG Escalab 200R electron spectrometer (Figure 2.6) equipped with a hemispherical electron analyzer, operating in a constant pass energy mode, and a non-monochromatic Mg-Kα (hv = 1253.6 eV, 1 eV = 1.603 x 10^{-19} J). X-ray source was operated at 10 mA and 1.2 kV. The angle of the incident photon beam was 45º with respect to the normal of the sample. The background pressure in the analysis chamber was kept below 7x10^{-9} mbar during data acquisition. The binding energy (BE C1s = 284.9 eV) of adventitious C1 was used as reference. A Shirley background subtraction was applied and Gaussian-Lorentzian product functions were used to approximate the line shapes of the fitting components.

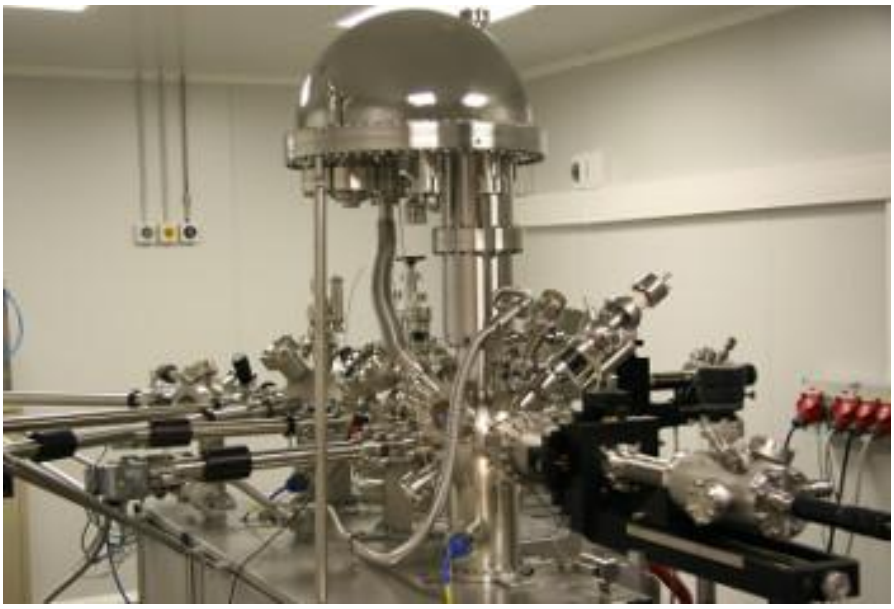

Figure 2.6 Equipment used to carry out XPS experiments at the Institut de Tècniques Energètiques in the Universitat Politècnica de Catalunya

2.3.11 Infrared Spectroscopy (FTIR)

IR is a technique that can be used to identify molecules by analysis of their constituent bonds. Each chemical bond in a molecule vibrates at a frequency characteristic of that bond. A group of atoms in a molecule may have multiple modes of oscillation caused by the stretching and bending motions of the group as a whole. If an oscillation leads to a change in dipole in the molecule then it will absorb a photon that has the same frequency. The vibrational frequencies of most molecules correspond to the frequencies of infrared light. Typically, the technique is used to study organic compounds using light radiation from (4000–400) cm^{-1}, the mid-infrared. A spectrum of all the frequencies of absorption in a sample is recorded. This can be used to gain information about the sample composition in terms of chemical groups present and also its purity [2].

In most spectrometers, electromagnetic radiation passes through the sample under study. The resulting absorptions are analyzed as a function of wavelength. The methods used (transmission, reflection, or emission spectroscopies), the preparation of the samples (e.g., pressing or dilution) and the choice of the cells are determined by the information expected and the type and the transparency in the IR region of the sample. For example, in heterogeneous catalysis, it is important: (a) to know the catalyst properties (framework vibrations, surface species, acidity, oxidation state of the ion, metal dispersion); (b) to

define the interactions between the sorbents and the catalysts (e.g., properties of the surfaces groups, adsorption of acid or basic molecules, adsorption of reagents and products, intermediate species, and modification of the oxidation state) [5].

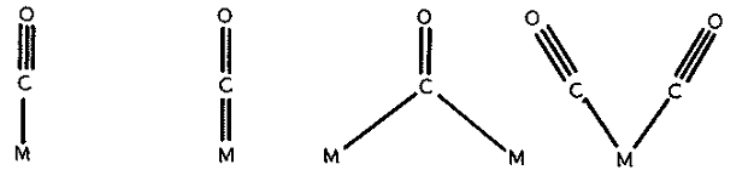

(a) (b) (c) (d)

Figure 2.7 CO adsorbed on metal; (a, b) to a single metal (M) atom, (c) to a pair of metal atoms, (d) two molecules on one metal atom [9]

Carbon monoxide (CO) is a probe molecule used in IR spectroscopy which allows separate monitoring of different species of metals in catalysts. Eischens, Francis, and Pliskin [10] observed spectra of CO adsorbed on metal particles separated from each other by a transparent support such as high-area powdered silica. Their spectra showed that some of the CO was adsorbed linearly to a single metal atom (Figures 2.7a and b) and some in a bridged form to a pair of metal atoms (Figure 2.7c). Later Yang and Garland [11] showed that a proportion of the carbon monoxide molecules may be adsorbed in pairs on the same metals atoms (Figure 2.7d).

CO allows separate monitoring of different species such as Ni^{2+}, Ni^{+}, and Ni^{0} on the surface of supported Ni catalysts. Many data in the literature concerning CO adsorption on metallic Ni show that, in general, the adsorption species at RT can be divided in two groups: (i) reversible and (ii) irreversible adsorption. The irreversible adsorption is also attributed to two different species: linear and bridged CO. If regular crystal planes such (100) and (110) are exposed on the metal surface (big Ni particles), the linear species are observed at ca. 2030 cm^{-1}. In addition, the bands due to bridged species (around 1900 cm^{-1}) are relatively intense. On the contrary, if the surface is "amorphous" (small metal particles) the bands due to linear species are more intense than the bands characterizing bridged species and are detected at higher frequencies (> 2040 cm^{-1}) than the bands of CO linearly adsorbed on regular planes [12]. In Table 2.1 is shown the IR band assignment of CO adsorbed in Ni species.

Table 2.1 IR band assignment of CO adsorbed in Ni species [13]

Adsorption site	IR bands (cm^{-1})
(i) $Ni^0(CO)_x$ subcarbonyls on defect sites (ii) Carbonyls on isolated Ni^0 sites in vicinity of oxide phase (unreduced Ni^{n+} or support)	2100 – 2070
Linear Ni^0-CO species	2065 – 2025
Bridged carbonyls on partially oxidized surfaces	1970
Bridged carbonyls	1950 – 1910
Ni_3CO and Ni_4CO	Below 1890

The IR measurements were carried out on a Vertex-70 (Bruker) spectrometer (Figure 2.8) equipped with a MCT detector, operating at 4 cm^{-1}. The *in situ* infrared cell used was a 2¾ in six-way stainless steel cube equipped with KBr windows. The cell is connected to a gas handling/pumping station and through both leak and gate valves to a quadruple mass spectrometer (UTI 100C). The catalyst was pressed onto a fine tungsten mesh, which, in turn was mounted onto a copper sample holder assembly attached to ceramic feedthroughs of a 1.33 inch flange. The sample temperature was monitored through a chromel/alumel (K-type) thermocouple spot-welded to the top center of the tungsten mesh. The sample could be heated resistively to ~1000 K and cooled with liquid nitrogen to ~90 K. Prior to the IR measurements the sample was heated to 773 K and kept at that temperature for about 2 h to ensure the complete removal of water from the catalyst. FTIR spectra of adsorbed CO were acquired from *in situ* reduced (at 773 K) samples at ~ 300 K. All the samples were reduced at 773 K two times. First for 30 min, then for 10 min in ~0.5 Torr of H_2. The cell was evacuated between the reduction steps and after the second reduction step. The base pressure of the IR cell following the reduction with H_2 was less than 5×10^{-8} Torr. CO adsorption measurements on the reduced samples were carried out at ~ 300 K sample temperature. Prior to each spectral series acquisition, a background spectrum was taken of the clean, freshly reduced sample. For each sample stepwise CO adsorption was performed until the final CO pressure in the cell reached 0.350 Torr for the Ni, 0.2 Torr for the Cu and 0.350 Torr for the Ni/Cu sample. After equilibration the cell was evacuated for 10 min at 300 K (in order to remove weakly held CO) and the FTIR spectrum of strongly adsorbed CO was recorded. At the conclusion of each spectral acquisition the sample was heated in vacuum: the Ni sample to 650 K (IR at every 50 K at

RT), the Cu sample to 400 K, and the Ni/Cu bimetallic sample to 600 K and the desorbing CO was followed by the mass spectrometer.

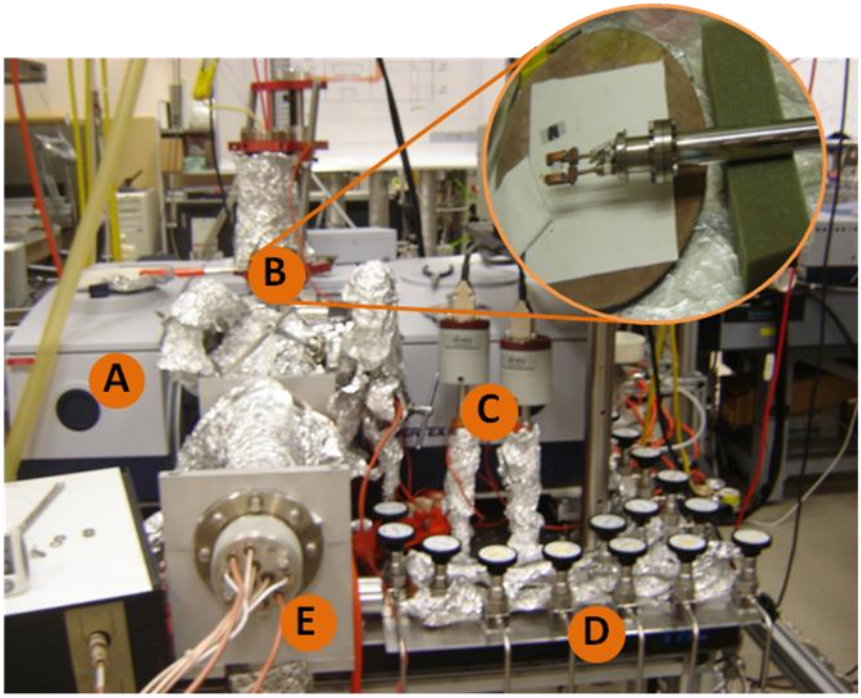

A. Mattson Research Series 1 FT-IR instrument
B. Sample Holder
C. Baratron Capacitance Manometer
D. Reservoirs of probe molecules
E. Mass spectrometer

Figure 2.8 FTIR experimental set-up

2.3.12 Raman Spectroscopy (Raman)

Raman scattering is named after the Indian scientist C.V. Raman who discovered the effect in 1928. If light of a single colour (wavelength) is shone on a material, most scatters off with no change in the colour of the light (Rayleigh scattered light). However a tiny fraction of the light (normally about 1 part in 10 million) exchanges energy with vibrations in the material and is scattered with a slightly different colour (Raman scattered) because of its changed energy. Scattering occurs when an electromagnetic wave encounters a molecule, or passes through a lattice. When light encounters a molecule, the vast majority of photons (>99.999%) are elastically scattered; this Rayleigh scattering has the same wavelength as the incident light. However, a small proportion (<0.001 %) will

undergo inelastic (or Raman) scattering where the scattered light undergoes a shift in energy; this shift is characteristic of the species present in the sample.

The general aim of Raman spectroscopy is to analyze the Raman scattered light and infer from it as much as possible about the chemistry and structure of the material. The Raman Effect is complementary to infrared spectroscopy. Molecular vibrations are sampled in both techniques, however different fundamental selection rules regarding the activity of specific vibrations results in the spectra of each giving different information. More specifically infrared spectroscopy requires a dipole moment change through the vibration, whilst Raman requires a change in polarisability. Micro-Raman instruments usually consist of (Figure 2.9):

- A monochromatic light source (normally a laser)
- A means of shining the light on the sample and collecting the scattered light (often this is a microscope)
- A means of filtering out all the light except for the tiny fraction that has been Raman scattered (often holographic 'notch' or dielectric 'edge' filters)
- A device (such as a diffraction grating) for splitting the Raman scattered light into component wavelengths, i.e. a spectrum.
- A light-sensitive device for detecting this light (normally a CCD camera)
- A computer to control the instrument and the motors and analyses and store the data

In this investigation, Raman spectra of the spent catalysts were obtained by using a Renishaw spectrometer with a CCD camera of 400×578. Approximately, 10 mg of each sample was placed on a microscope slide and placed on the stage (inside microscope enclosure), and was excited using an Ar laser operating at 514.5 nm and a power of 2 mW (used at 50 %). An objective x20 was used. Each measurement was run in cycle mode (3 accumulations) to increase the strength of the Raman signal, in a range from (100 to 2000) Raman shift/cm^{-1}, and the exposure time was 40 s. In the Figure 2.9 is shown a diagram of the system.

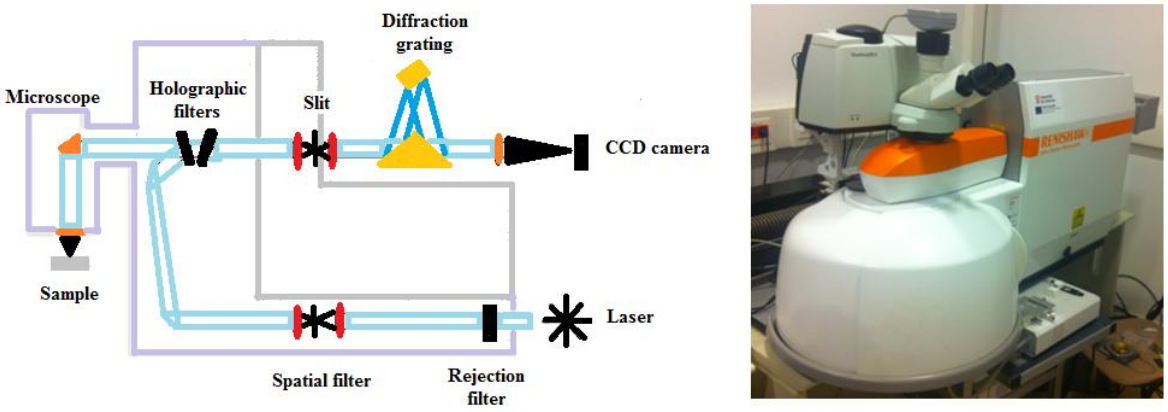

Figure 2.9 Diagram of the Raman spectrometer

2.3.13 Temperature programmed oxidation (TPO)

TPO examines the extent to which a catalyst can be re-oxidized. Generally, TPO analyses are used to measure the degree of reduction of certain oxides. Usually the sample is pretreated and the metal oxides are reduced to the base metal, typically with a gas mixture of hydrogen with either nitrogen or argon. Then the reactant gas, typically (2–5) % oxygen with helium, is applied to the sample in pulses or, alternatively, as a steady stream. The furnace heats the sample tube and sample according to the user-selected temperature program. The oxidation reaction occurs at a specific temperature. The Auto-Chem II 2920 measures the uptake of oxygen.

In this investigation the amounts of coke deposited on the used catalysts were determined by TPO. These tests were carried out with a Sensys Evo apparatus. TPO profiles were obtained from approximately 20 mg of sample, placed in a quartz reactor (ID= 0.5 cm, length = 10 cm) and heated from 303 K to 1023 K at a rate of 10 K/min in air flow. The CO_2 produced was quantified on-line using a Pfeiffer Vacuum QME 220 mass spectrometer.

2.4 Experimental set-up employed for the catalytic conversion of glycerol

A simplified diagram of the experimental set-up is shown in the Figure 2.10. The catalytic conversion of glycerol was carried out in gas phase in a quartz fixed bed down flow reactor at 573 K for 6 h. Gas flow rates were controlled by unit mass flow controllers.

The feed gas composition during reaction was 5 % H_2 in Ar (CARBUROS METALICOS). Pure glycerol (Sigma-Aldrich, 99.0 %) was used to prepare an aqueous

solution of glycerol (3 v/v %). This solution was pumped by a syringe pump with flow of 3.5 ml/h and injected into the reactive gas. Previous to entrance to the reactor the reactive mixture was preheated at 573 K. Hydrogen/Glycerol molar ratio of 10 was used in all experiments. Typically 100 mg of sample in the form of pellets, with size ranging 2 mm – 3 mm, were loaded in the quartz reactor, which is placed in an oven coupled with temperature control system; it was heated to the desired temperature.

The condensed products were trapped in an ice bath condenser and analyzed by HPLC every 20 min of reaction in a high performance liquid chromatography (HPLC, Agilent technologies 1100 series) equipped with a ICSep ICE-COREGEL 87H3 Column serial Nº 12525124, a diode-array detector (DAD) and a refractive index detector (RID). The mobile phase was deionized and filtered water with pH controlled to 2.2 by addition of sulfuric acid with flow of 0.6 ml/min and a pressure of 5 MPa. The temperature of the HPLC column was 313 K and 50 min of analysis for each chromatogram.

The gaseous products were continuously analyzed by an on-line gas chromatograph equipped with a Flame Ionization Detector (FID) and a HP-Plot Q column (polystyrene-divinylbenzene stationary phase, 30 m×0.32 mm×20 μm). Helium was used as the carrier gas at a flow of 19 ml/min. The operational temperatures of the GC for the injection port, column oven, and detector were 523 K, 473 K and 523 K, respectively. Also, a total organic carbon (TOC) analyzer was used to check the carbon balance. The TOC analyses were performed on a Shimadzu TOC-5000A using high purity air (pressure of 400–500 kPa and flow rate of 150 ml/min) and a furnace temperature of 953 K.

Also, some qualitative analyses were carried out using a Hewlett Packard 5890 Series II Gas-Chromatograph equipped with an HP 6890 Automatic Injector and a FID. The compounds were separated on an Agilent 19091F-433 HP-FFAP (polyethylene glycol stationary phase; 30 m×0.25 mm×0.25 μm) fused-silica capillary column. Instrumental conditions were: injector temperature: 493 K, detector temperature: 553 K, carrier gas: helium at 1.5 ml/min. The FID gas flow rates were: hydrogen 40 ml/min and air 400 ml/min. Mass spectra were acquired in the electron impact mode (ionization energy, 70 eV, source temperature 503 K) at 5 scan/s, using full scan with a mass acquisition from m/z 15 to 550.

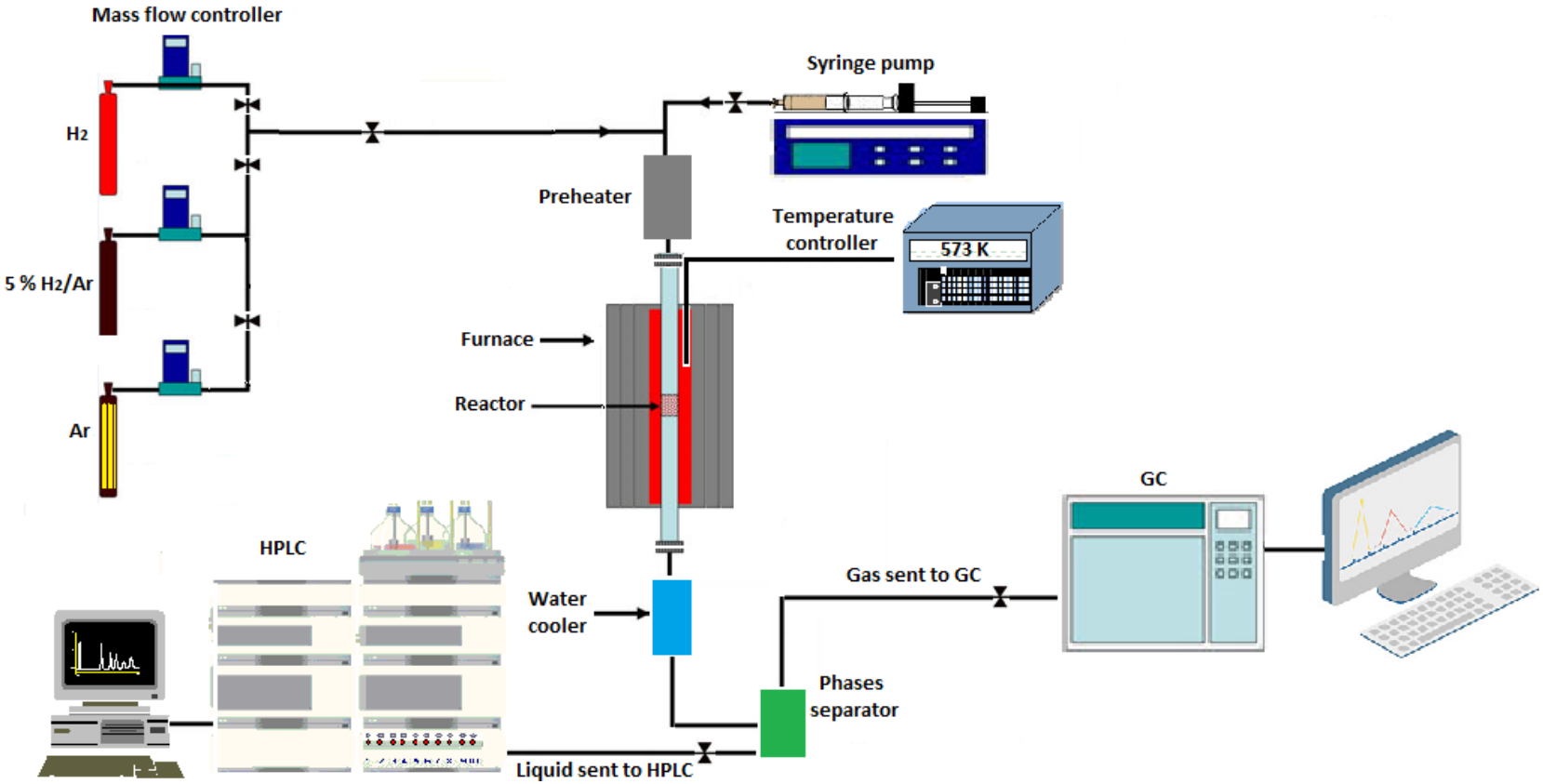

Figure 2.10 Schematic representation of the experimental set-up employed for the hydrogenolysis of glycerol

The identification of the dihydroxyacetone was performed by derivatization. The derivatization protocol was as following:

1. 100 µl of the sample in a 2 ml vial was submitted to liofilization for 8 h until the sample dry.
2. Add 30-40 µl of the derivatizant (MSTFA), stir for10 minutes and finally the resultant mixture was aged for 1 hour under stirring.
3. Change the resultant mixture in a vial containing an inert solvent.
4. Analysis by GC-MS.

2.5 References

[1] J. R. Anderson, K.C. Pratt, Introduction to Characterization and Testing of Catalysts, Academic Press, New York, 1985.
[2] B. Imelik, J.C. Vedrine, Catalyst Characterization: Physical Techniques for Solid Materials, United States of America, 1994.
[3] J.W. Niemantsverdriet, Spectroscopy in Catalysis: An Introduction, 2 ed., Federal Republic of Germany, 2000.
[4] A. Monshi, M. R. Foroughi, M.R. Monshi, World Journal of Nano Science and Engineering. 2 (2012) 154-160.
[5] B. Viswanathan, S. Kannan, R.C. Deka, Catalysts and Surfaces: Characterization Techniques, Oxford, U.K, 2010.
[6] S. D. Kelly, D. Hesterberg, B. Ravel, in: A. L. Ulery, L.R. Drees (Eds.), Methods of Soil Analysis: Part 5- Mineralogical Methods, Soil Science Society of America, Madison, USA, 2008.
[7] J. Anderson, M. Fernández, Supported Metals in Catalysis, Singapore, 2005.
[8] F. Delannay, Characterization of Heterogeneous Catalysts, United States of America, 1984.
[9] D.N. Kendall, Applied Infrared spectroscopy Reinhold Publishing Corporation, New York, 1966.
[10] R. P. Eischens, S. A. Francis, W.A. Plisk, J. Phys. Chem. 60 (1956) 194-201.
[11] A. C. Yang, G. C. W, J. Phys. Chem. 61 (1957) 1504.
[12] K. Hadjiivanov, M. Mihaylov, D. Klissurski, P. Stefanov, N. Abadjieva, E. Vassileva, L. Mintchev, J. Catal. 185 (1999) 314-323.
[13] M. Mihaylov, O. Lagunov, E. Ivanova, K. Hadjiivanov, Top. Catal. 54 (2011) 308-317.

Chapter 3

Conversion of glycerol over Ni/ γ-Al_2O_3 catalysts

3.1 Introduction

This chapter presents an experimental study on conversion of glycerol in gas phase over Ni/γ-Al_2O_3 catalysts. Different reduction temperatures of the Ni samples were used as parameter to evaluate its effect on the catalytic performance. Initially, the structure of the fresh catalysts was characterized using several techniques such as TPD-NH_3, TGA-MS, TPR, XRD, N_2-physisorption, H_2-chemisorption, TEM, XANES, and FTIR of adsorbed CO.

The conversion of glycerol with each catalyst (Ni623, Ni723, Ni823, Ni923, Ni993 and Ni1073) was studied. The reaction was carried out at atmospheric pressure in the presence of 5 % H_2/Ar flow in a fixed bed reactor. The conversion of the glycerol was defined as follows:

$$Conversion\ of\ \text{glycerol}\ (\%) = \frac{Moles\ of\ glycerol\ reacted}{Initial\ moles\ of\ glycerol}\ x\,100 \qquad \text{Eq. 3.1}$$

And, the selectivity to each product was defined as selectivity based on carbon, where:

$$Selectivity\ (\%) = \frac{Moles\ of\ carbon\ in\ specific\ product}{Moles\ of\ carbon\ in\ all\ \ products}\ x\,100 \qquad \text{Eq. 3.2}$$

The experimental results of glycerol conversion and selectivity to different products obtained are discussed. Then, a general reaction pathway for glycerol conversion is proposed.

After reaction, the used catalysts were also characterized by TPO-MS, Raman, XPS, FTIR of adsorbed CO, and HRTEM in order to determine the deactivation sources of the catalysts during the conversion of glycerol.

Finally, it was studied the regeneration process of the catalysts. The Ni723 sample was chosen as a representative material for regeneration test. After 6 h of reaction the Ni723 sample was regenerated in air flow (50 ml/min) from RT to 723 K at 5 K/min and kept at 723 K for 4 h. The catalyst was then purged with Ar flow and reduced under H_2 flow at 723 K for 4 h. The regeneration process was applied in three reaction cycles.

The main results obtained are presented and discussed in this chapter.

3.2 Characterization of the fresh catalysts

3.2.1 Thermal decomposition of $Ni(NO_3)_2{\cdot}6H_2O$ impregnated over γ-Al_2O_3

The $Ni(NO_3)_2{\cdot}6H_2O$ impregnated over γ-Al_2O_3 sample was characterized by TGA-MS, *in situ* XRD and XANES, as shown in Figure 3.1. The main decomposition of $Ni(NO_3)_2{\cdot}6H_2O$ under H_2/Ar occurs below 620 K with a constant release of water between 350 K and 550 K and intense evolution of water between 550 K and 620 K (m/z =18). Furthermore, the presence of N_2O (m/z =44) and NO_2 (m/z =46) between 520 K and 620 K, as well as some traces of oxygen (m/z= 32), are also observed (Figures 3.1a and b).

The sample was also monitored by TPR (Figure 3.1c). A sharp band of hydrogen consumption is observed between 520 K and 620 K which corresponds to the decomposition of nickel nitrate precursor to NiO species, in accordance with previous work [1-4]. In addition, a broad band between 600 K and 1000 K (Figure 3.1c) is probably due to the reduction of NiO species to metallic Ni.

Figure 3.1d shows the XRD patterns of the impregnated $Ni(NO_3)_2{\cdot}6H_2O$ over γ-Al_2O_3 reduced *in situ* under a flow of H_2. Two prominent reflections which could be assigned to $(Ni(OH)_2(NiOOH)_{0.167})_{0.857}$ (Jamborite, ICDD 89-7111) are evident in the diffractogram when the dried sample was heated from RT to about 600 K. These two peaks correspond to the (003) and (006) planes of the Jamborite phase. Indeed, Sietsma et al. [3] observed that nickel nitrate hydroxide with composition $Ni_3(NO_3)_2(OH)_4$ was formed on SBA-15 that had been impregnated with $[Ni(OH_2)_6](NO_3)_2$ aqueous solution. Consequently, the presence of other nitrate phases not detected by XRD should not be discarded. Thus, *in situ* XRD shows that the total decomposition of the Jamborite phase occurs around 600 K in agreement with TGA-MS and TPR. The broad peaks in the TPR profile (Figure 3.1c) between 600 K and 1000 K indicate the reduction of NiO species with different interaction with the support [4-6]. The broad TPR signal with a shoulder at 740 K can be attributed to reduction of NiO species which are weakly bound to γ-Al_2O_3, while the shoulder at around 800 K should be assigned to reduction of NiO species with strong interaction with the γ-Al_2O_3 (Figure 3.1c).

The Ni K-edge temperature resolved XANES spectrum and the distribution of Ni species with temperature for the *in situ* reduction of $Ni(NO_3)_2{\cdot}6H_2O$ impregnated over γ-Al_2O_3 are shown in Figures 3.1e and f, respectively. The white line (WL) is not affected by

the increase in temperature between RT and 650 K, indicating no reduction of NiO species to metallic Ni. Between 650 K and 920 K, the WL decreases with increasing temperature, indicating formation of metallic Ni. The WL intensity keeps constant above 920 K, suggesting that all NiO was converted to metallic Ni. The XRD patterns (Figure 3.1d) show peaks for metallic Ni above 800 K, corresponding to planes (111) and (200) (ICDD 4-0850). The XRD measurements also reveal reflections corresponding to γ-Al_2O_3 phase (ICDD 79-1558) and α-Al_2O_3 (ICDD 46-1212).

Figure 3.1g shows the change in the diffracted area with reduction temperature for the components detected in the Ni/γ-Al_2O_3 sample; the dates were extracted from Rietveld refinements. It can be seen that the diffracted area of the Jamborite phase decreases as the reduction temperature increases until its total decomposition around 620 K. Furthermore, Figure 3.1g shows that around 650 K starts to appear the Ni phase and its diffracted area increases until around 950 K. The diffracted area of the support is not affected by temperature.

Based on TGA-MS, TPR, XANES and *in situ* XRD, it is established that decomposition of $Ni(NO_3)_2{\cdot}6H_2O$ impregnated over γ-Al_2O_3 occurs between 350 K and 620 K with formation of NiO species, which are finally reduced to metallic Ni between 650 K and 920 K. In addition, TGA result shows that the total weight loss for the sample is close to the theoretical value of 26.5 % for complete decomposition of $Ni(NO_3)_2{\cdot}6(H_2O)$ into metallic Ni [7, 8]. In Table 3.1 is shown a summary of the results of the formation of metallic Ni by reduction of NiO species obtained by XANES (Figure 3.1f), reaching 100 % of reduction above 920 K.

3.2.2 N_2-physisorption

The N_2-physisortion results of the samples are depicted in Table 3.1. The γ-Al_2O_3 support presents a surface area of 113 m^2/g and pore volume of 0.20 cm^3/g. The introduction of Ni on the γ-Al_2O_3 produces a decrease in the surface area and pore volume of the support, suggesting that the impregnation with Ni species presumably lead to partial pore blockage in the support by Ni species crystallites [4]. For instance, the Ni623 sample presents a surface area of 100 m^2/g and pore volume of 0.17 cm^3/g against 113 m^2/g and 0.2 cm^3/g of the γ-Al_2O_3.

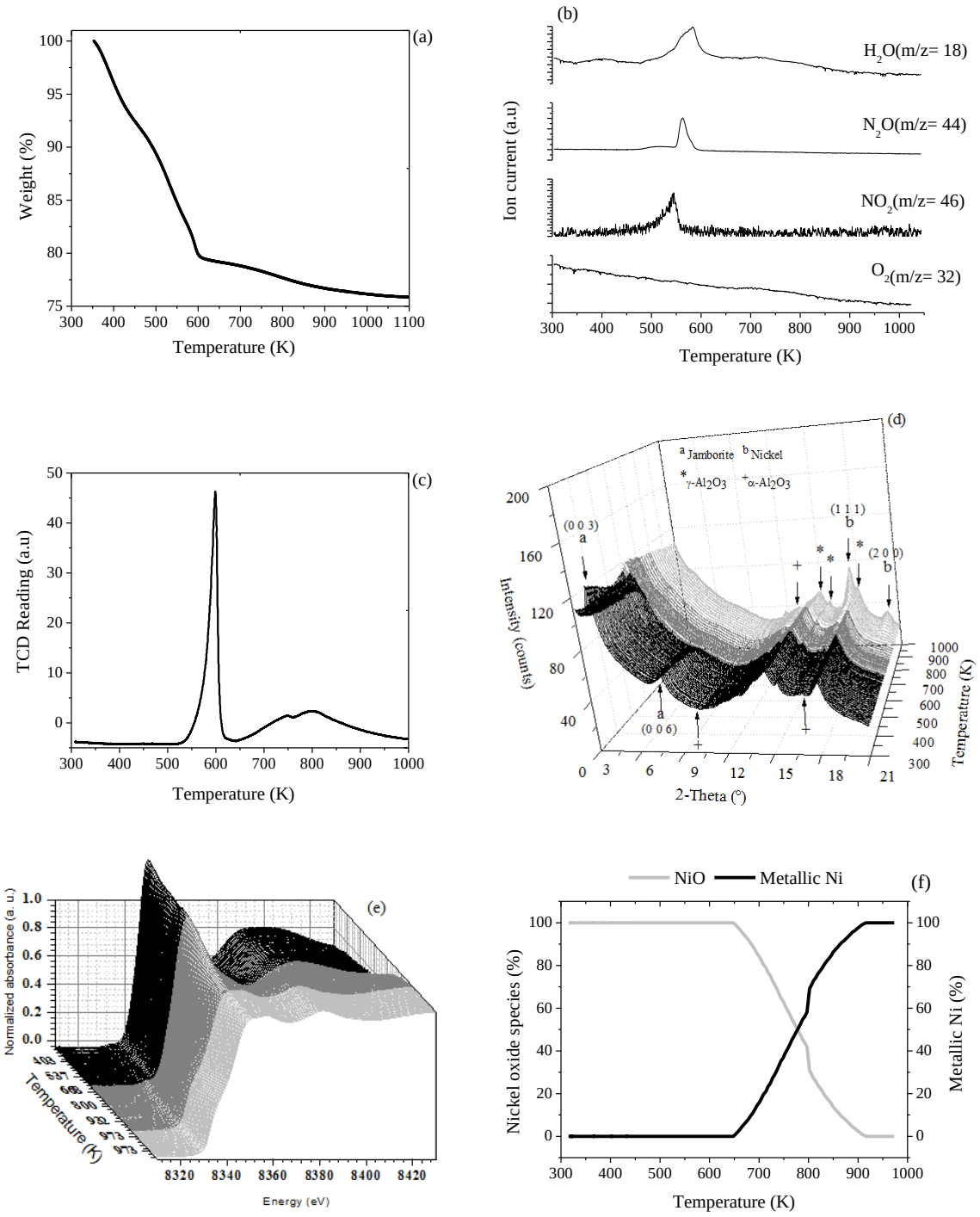

Figure 3.1 Thermal decomposition of nickel (II) nitrate hexahydrate impregnated on γ-Al_2O_3: (a) thermogravimetric analysis; (b) MS results obtained from the off gas during thermal treatment, (c) H_2-TPR analysis, (d) *in situ* XRD, (e) XANES, (f) Degree of reduction of Ni and (g) Quantitative phases analysis extracted from Rietveld refinement

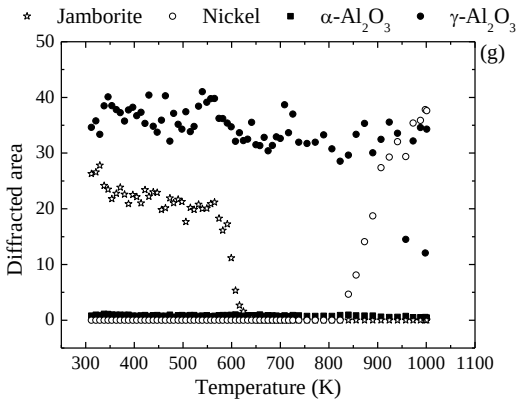

Figure 3.1 (continuation) Thermal decomposition of nickel (II) nitrate hexahydrate impregnated on γ-Al_2O_3: (a) thermogravimetric analysis; (b) MS results obtained from the off gas during thermal treatment, (c) H_2-TPR analysis, (d) *in situ* XRD, (e) XANES, (f) Degree of reduction of Ni, and (g) Quantitative phases analysis extracted from Rietveld refinement

Additionally, as the reduction temperature pre-treatment of the Ni/γ-Al_2O_3 samples is increased there is a decrease in surface area from 113 m^2/g to 74 m^2/g compared with the pure γ-Al_2O_3 support, as shown in Table 3.1. The effect of the reduction temperature on the surface area is remarkable in Ni993 and Ni1073 samples.

Table 3.1 Results of N_2-physisorption and XANES of the fresh Ni/γ-Al_2O_3 catalysts

Sample	S_{BET} (m^2/g)	Pore volume (cm^3/g)	Pore size (nm)	XANES	
				NiO (%)	Ni (%)
γ-Al_2O_3	113	0.20	4.54	-	-
Ni623	100	0.17	4.54	100	0
Ni723	99	0.17	4.54	75.1	24.9
Ni823	94	0.18	4.75	22.4	77.6
Ni923	93	0.19	4.75	0	100
Ni993	79	0.18	5.44	0	100
Ni1073	74	0.17	5.44	0	100

The N_2 adsorption-desorption isotherms of the Ni supported on γ-Al_2O_3 are shown in Figure 3.2a. All Ni catalysts exhibit the type IV isotherm according to the Brunauer-Deming-Deming-Teller (BDDT) classification, which exhibits the condensation and evaporation step characteristic of mesoporous materials. All isotherms at low equilibrium pressures are reversible, whereas at higher equilibrium pressures they exhibit a hysteresis loop of the H3 type [9]. This type of hysteresis loop indicates the presence of slit-shaped

mesopores or pores with narrow necks and wide bodies. The pore diameter distribution curves of the samples are shown in Figure 3.2b. All the samples present a pore diameter in the range between 4.5 nm and 5.5 nm.

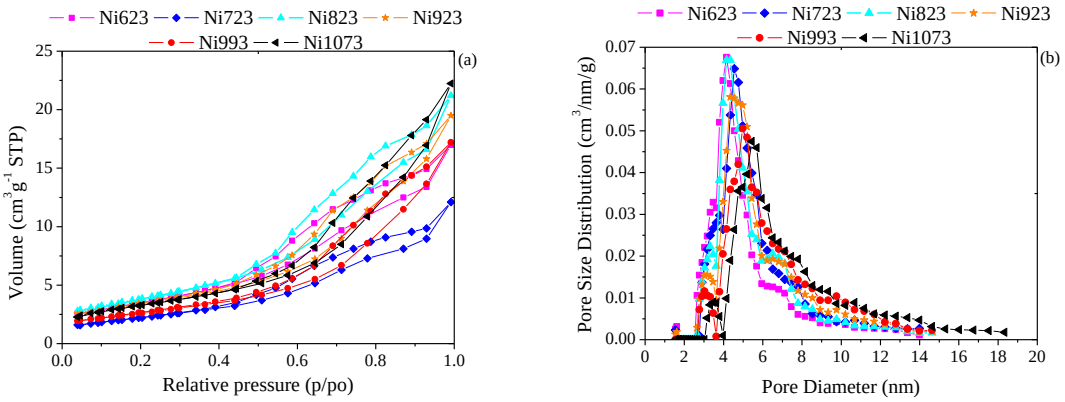

Figure 3.2 (a) N_2-physisorption isotherms and (b) Pore size distribution of the fresh Ni/γ-Al_2O_3 samples

3.2.3 Conventional X-ray diffraction

The XRD patterns of the fresh Ni/γ-Al_2O_3 samples are shown in Figure 3.3. Two distinct crystallographic phases are observed, which correspond to metallic Ni (ICDD 4-0850), and the corresponding γ-Al_2O_3 phase (ICDD 79-1558) of the support. In these diffractograms, the α-Al_2O_3 phase is not observed, probably due to the low concentration of this phase and the smaller brilliance of the diffractometer. The NiO phase (Bunsenite, ICDD 47-1049) is not detectable in any samples. It can be seen that the metallic Ni diffraction peaks are broad and of low intensity, indicating that the Ni metal particles are highly dispersed on the γ-Al_2O_3 support in the fresh catalysts.

The peaks at around 2θ = 37.5º, 45.7º and 66.7º are assigned to γ-Al_2O_3 phase. The other broad peaks at around 2θ = 44.5º and 51.8º are associated with metal Ni phase [4, 10], which are observed for samples treated above 823 K. The highest intensity peak observed at 2θ = 44.5 º is attributed to Ni (111) and the peak at 2θ = 51.8 ° corresponds to Ni (200). It is noteworthy that the metallic Ni peak became more intense as the reduction temperature increased, indicating an increase in the Ni particle size by sintering. The spinel $NiAl_2O_4$ crystalline phase (ICDD 10-339) is not detected in any sample by XRD.

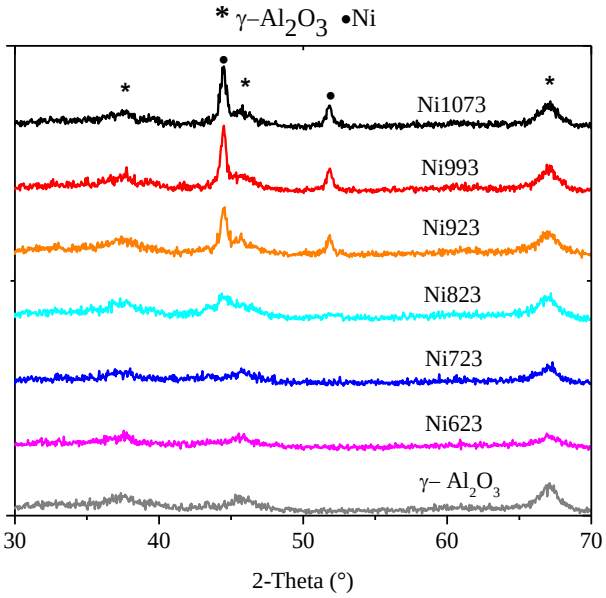

Figure 3.3 X-ray diffraction patterns of the fresh Ni/γ-Al_2O_3 catalysts

3.2.4 TEM

The morphology and the metal particle size of the fresh Ni/γ-Al_2O_3 catalysts were characterized by TEM (Figure 3.4a). The particle size was measured directly from TEM images at different randomly selected regions for each sample. It can be seen that the shape and density of Ni crystallites distributed over γ-Al_2O_3 changed with the pre-treatment temperature.

The Ni particle size distributions of the fresh catalysts are shown in Figure 3.4b. The Ni catalyst reduced at 723 K contains small Ni particles with sizes ranging between 4 nm and 10 nm. As the reduction temperature increases, the Ni particles become larger, with mean diameter at about 10 nm and 20 nm for samples Ni823 and Ni993, respectively. However, when temperature was further increased, larger Ni particles (about 30 nm) with a broader size distribution were observed. In Table 3.2 is shown the mean particle size of each fresh sample.

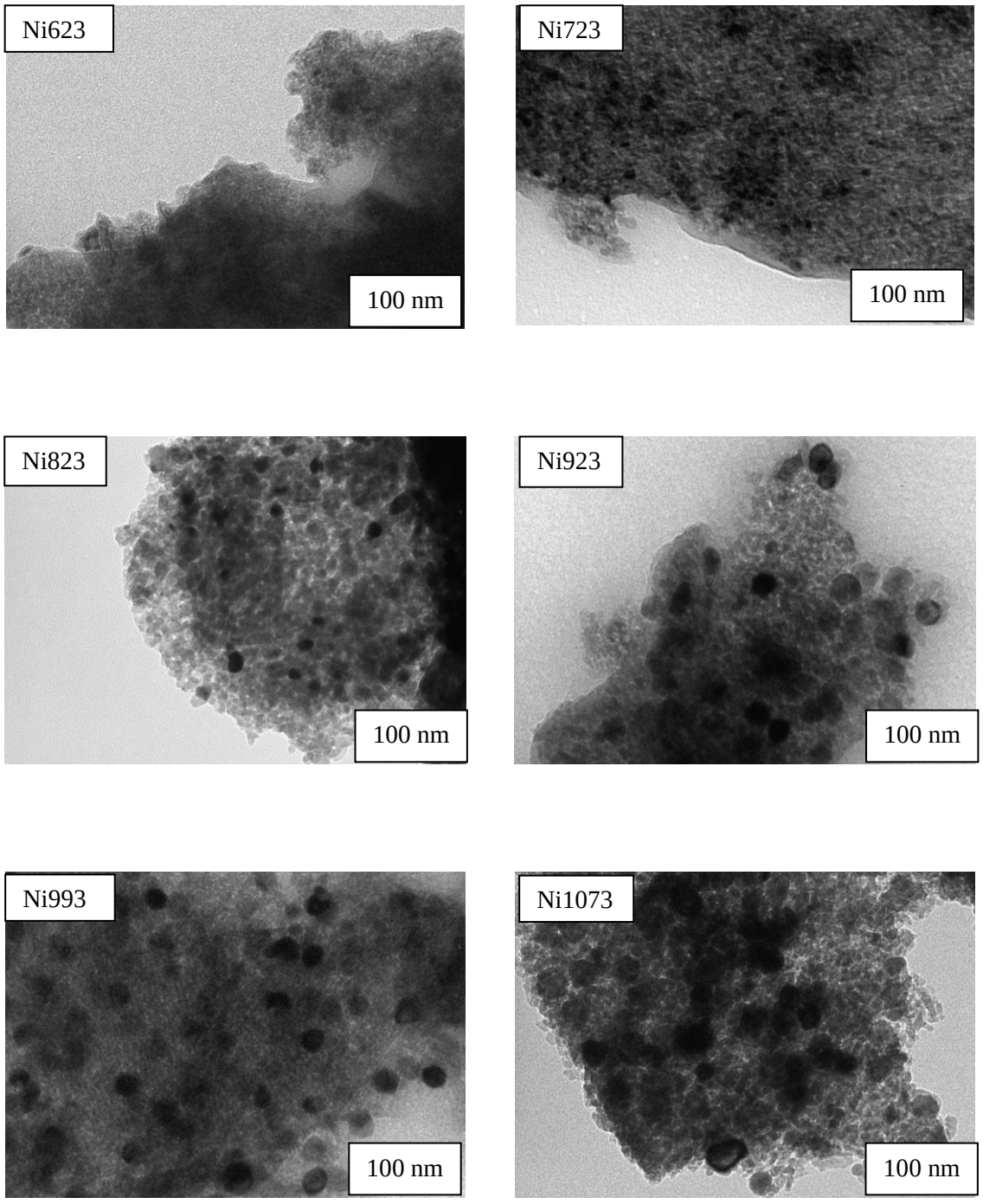

Figure 3.4(a) TEM images of the fresh Ni/γ-Al_2O_3 samples

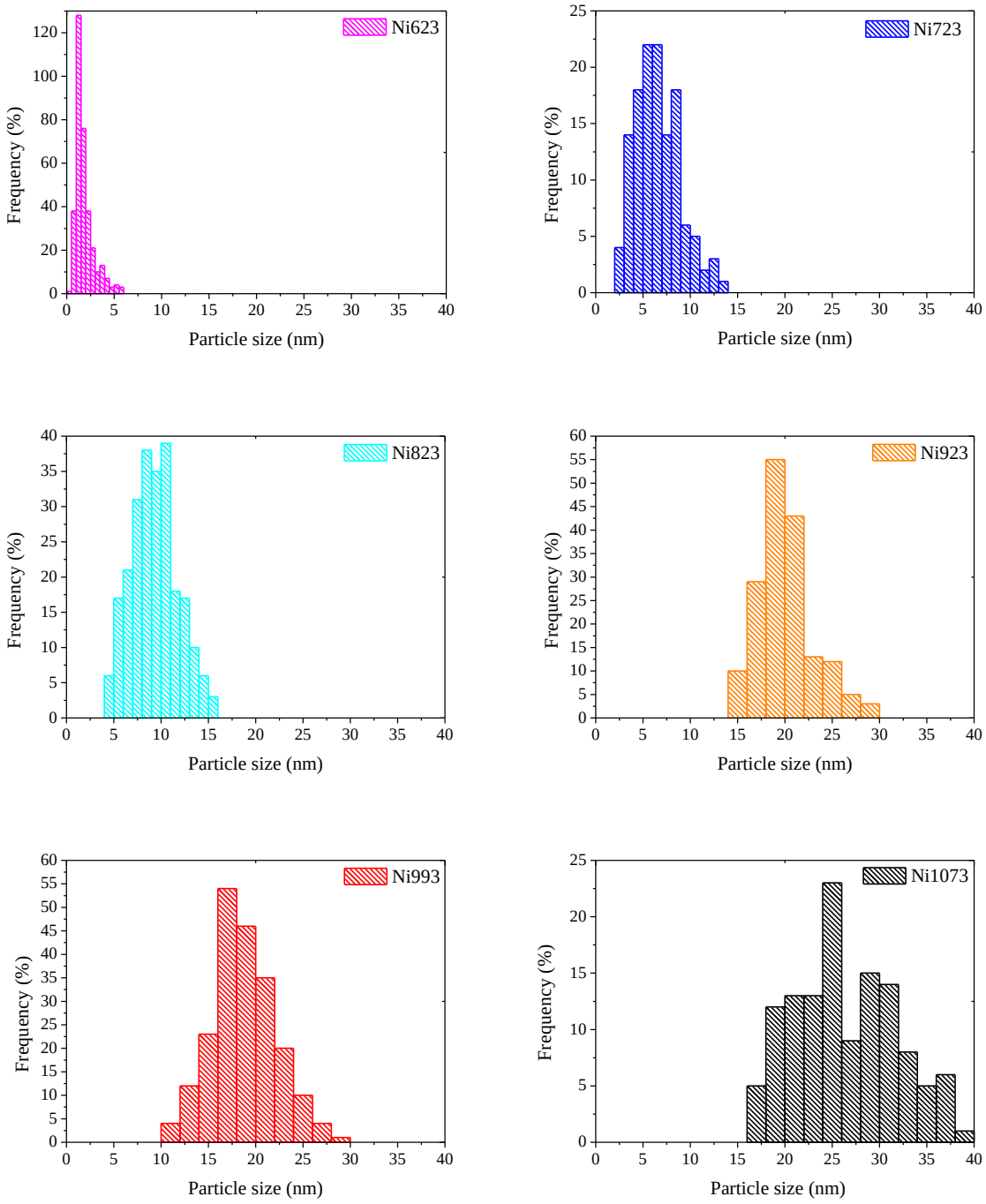

Figure 3.4(b) Nickel particle size distribution of the fresh Ni/γ-Al_2O_3 samples

3.2.5 H_2-Chemisorption

Table 3.2 shows the number and percentage of exposed Ni atoms, as determined by H_2-chemisorption. The Ni623 sample has fewer exposed Ni atoms than the Ni723 sample (3.4 % and 33 %, respectively), suggesting that Ni species present in the first sample was slightly reduced due to low reduction temperature, in agreement with XANES and TPR results. On the other hand, a loss of exposed Ni atoms is observed with increasing reduction temperature from 723 K to 1073 K (Table 3.2). The Ni1073 sample shows the lowest percentage of exposed Ni (around 0.7 %). A plausible explanation is that sintering is extensive at high reduction temperatures [6, 11]. The sintering of Ni particles on alumina is correlated to the bond strength between the metal particle and the support.

Table 3.2 Results of TPD-NH_3, H_2-chemisorption, and TEM of Ni/γ-Al_2O_3 and γ-Al_2O_3 samples

Sample	TPD-NH_3 ($\mu mol/g_{sample}$)			Number of exposed Ni atoms	TEM[b] (nm)
	Total	350-550 K	550-900 K		
Ni623	273.1	42.7	230.4	3.53×10^{18} (3.4 %)[a]	1.4
Ni723	205.4	69.6	135.9	3.43×10^{19} (33 %)[a]	6.0
Ni823	198.8	68.7	130.2	1.28×10^{19} (12 %)[a]	9.0
Ni923	159.5	37.0	122.5	7.11×10^{18} (6.9 %)[a]	19.0
Ni993	185.0	66.5	118.6	6.40×10^{18} (6.2 %)[a]	20.0
Ni1073	195.3	70.7	124.7	7.67×10^{17} (0.7 %)[a]	25.0
γ-$Al_2O_3$623	160.8	35.4	125.4	-	-
γ-$Al_2O_3$723	181.8	47.2	134.6	-	-
γ-$Al_2O_3$823	174.0	46.5	127.6	-	-
γ-$Al_2O_3$923	168.6	42.9	125.7	-	-
γ-$Al_2O_3$993	157.0	47.0	110.0	-	-
γ-$Al_2O_3$1073	163.4	48.1	115.3	-	-

[a] Values in the brackets are dispersion, [b] Mean particle size

3.2.6 NH_3-TPD

The NH_3-TPD profiles of the fresh catalysts show two main desorption regions, at 350 K–550 K and at 550 K–900 K, indicating the existence of two kinds of regions having different acid strengths (Table 3.2). The lower desorption temperature region is attributed to desorption of NH_3 bridge-bound to penta-coordinated aluminium (weak Lewis acidic sites), while the higher temperature region to desorption of terminally bound NH_3 on tri-coordinated aluminium (strong Lewis acid sites) [10]. The amount of desorbed ammonia

was highest for Ni623 and lowest for Ni923 with the respectively values of 273.6 μmol NH_3/g_{sample} and 159.5 μmol NH_3/g_{sample}.

NH_3-TPD analysis was also carried out on γ-Al_2O_3 submitted to the different reduction temperatures employed for each catalyst. The alumina support also reveals the presence of the two desorption temperature regions attributed to weak and strong acid Lewis sites. The NH_3 desorbed values of the support (Table 3.2) are very similar, regardless the reduction temperature used. A slight decrease of the strong acid sites is observed at higher reduction temperatures. However, the Ni incorporation produces a strong increase in the acid sites, mainly for the Ni623 sample. This is probably due to the presence of some NiO and nitrogen oxide species produced during the decomposition of the nickel nitrate.

In general, the introduction of Ni species increase the total acidity compared with the correspondent bare alumina. The amounts of desorbed NH_3 measured by volumetric adsorption are depicted in Table 3.2 for all the samples. The surface acidity was calculated as total acidity and expressed per μmol of NH_3 desorbed per gram of sample.

3.3 Catalytic conversion of glycerol

The catalytic performance of the Ni/γ-Al_2O_3 catalysts submitted to different reduction temperatures was evaluated in the conversion of glycerol under atmospheric pressure and 573 K. Blank tests using the same reaction conditions and either an empty or charged reactor with γ-Al_2O_3 show no glycerol conversion. This suggests that neither the homogeneous gas phase glycerol decomposition nor the γ-Al_2O_3 support contributed to the observed activity of the Ni catalysts. Markedly low activity for glycerol reaction is observed when the Ni/γ-Al_2O_3 sample is calcined without reduction.

The main products in the condensable phase observed during conversion of glycerol are: hydroxyacetone, pyruvaldehyde, pyruvic acid, lactic acid, lactide, EG, acetaldehyde, methyl lactate, traces of different products such as 1,2-PDO, methyl pyruvate, acetone, propanal, 2-propanol (2-PO), 1-propanol (1-PO), methanol, formic acid, acetic acid, and furan derivatives. Previous works about glycerol conversion reported that the furan compounds are the result of a catalytic cyclisation of hydroxyacetone [12]. The major products detected in the gas phase are CH_4, acetaldehyde, and traces of formaldehyde, propanal and acetone. Some compounds were also identified by GC-MS, in

appendix B is shown an example of chromatogram (Figure B.2) for one of our products solution, and in Table B.1 is shown each compound identified and the retention time.

The main products formed can be classified into two main groups: compounds with 3 carbon atoms (C3) and lower (C< 3). In the first group, dehydration and dehydrogenation products such as hydroxyacetone, pyruvaldehyde, pyruvic acid, and lactic acid, are obtained. In addition some lactide (C6) is formed by dimerization of lactic acid. The other group can be attributed to hydrogenolysis products (C < 3) such as CH_4 and acetaldehyde. Methyl lactate and methyl pyruvate are also formed, probably by esterification reaction between methanol with pyruvic acid and lactic acid, respectively. Methanol is formed in the glycerol hydrogenolysis step.

The effect of bifunctional metal-acid properties of the catalysts can be seen in two main routes presented in Scheme 3.1: (i) the hydrogenolysis of glycerol to CH_4 and acetaldehyde and (ii) dehydration-dehydrogenation to the production of hydroxyacetone, pyruvaldehyde, pyruvic acid, methyl lactate and lactide.

In the case of glycerol hydrogenolysis, the number of exposed Ni atoms determined the production of CH_4 and acetaldehyde. The metal property is remarkable especially to the Ni723 sample which presents the highest number of exposed Ni atoms (3.43×10^{19}, see Table 3.2), inducing the presence of the hydrogenolysis route. On the other hand, the acid property is remarkable especially for the Ni623 sample which presents the highest acidity (273.1 $\mu mol/g_{sample}$, see Table 3.2) among all samples and it favored the formation of hydroxyacetone and suppressed the formation of CH_4. Similar to Ni623 sample, the Ni1073 sample also exhibits poor hydrogenolytic capacity but in this case is due to the presence of large Ni particles which conferred the lowest number of exposed Ni atoms with a value of 7.67×10^{17} (Table 3.2).

It is important to note that esterification products such as methyl lactate and methyl pyruvate are observed when both routes of hydrogenolysis and dehydration-dehydrogenation are present. Since Ni1073 sample presents the poorest hydrogenolytic capacity, esterification products are not observable.

The catalytic performance for the Ni/γ-Al_2O_3 samples reduced at different temperatures is shown in Figure 3.5. It shows a decrease in glycerol conversion with time on stream. The deactivation is more pronounced for the Ni623 sample. The Ni623 catalyst

has the largest amount of stronger Lewis acid sites (273.1 μmol/g_{sample}) and the lowest amount of reduced Ni compared with the other samples (Table 3.2).

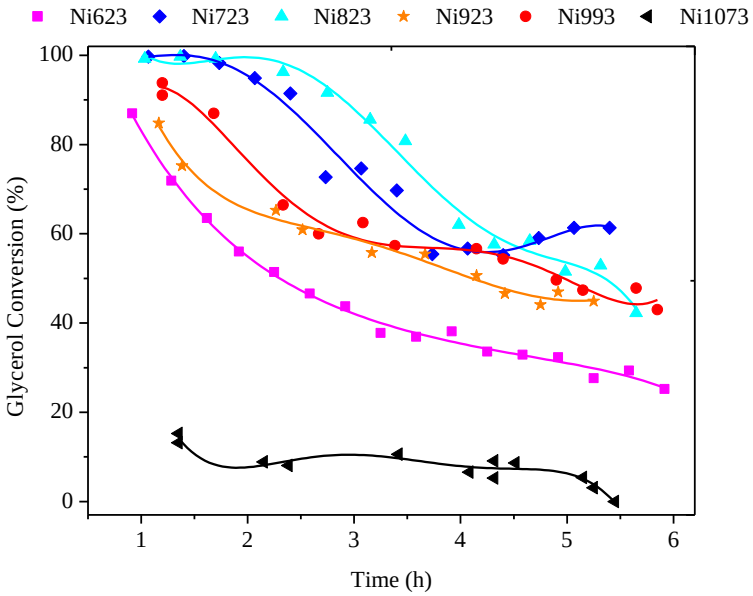

Figure 3.5 Catalytic performance of the Ni/γ-Al_2O_3 samples in function of time of reaction

The comparative selectivity profiles of the different products obtained for the Ni/γ-Al_2O_3 samples reduced at different temperatures are shown in Figure 3.6. In general, the Ni623, Ni723, Ni823, Ni923 and Ni993 samples exhibited similar tendency in product distribution. The catalyst deactivation shown in Figure 3.5 affected the selectivity of all these five samples during the glycerol conversion. The selectivity to hydrogenolysis products such as CH_4 decreases meanwhile the products of dehydration and dehydrogenation increases. For the first four samples the selectivity to CH_4 is about 100 % initially, and for the Ni993 sample it is about 70 %, and then decreases progressively to about 10 %–20 % after 3 h of reaction. Upon raising the reaction time to 6 h, the CH_4 selectivity remains unchanged. The decrease in CH_4 selectivity is accompanied by an increased of other products such as hydroxyacetone, pyruvaldehyde, pyruvic acid, lactide and EG. For example, the selectivity to hydroxyacetone presented by the Ni623, Ni723, Ni823, Ni923 and Ni993 at 50 % glycerol conversion is 20.1 %, 15.1 %, 17.4 %, 14.6 % and 12.7 %, respectively, as shown in Figure 3.6.

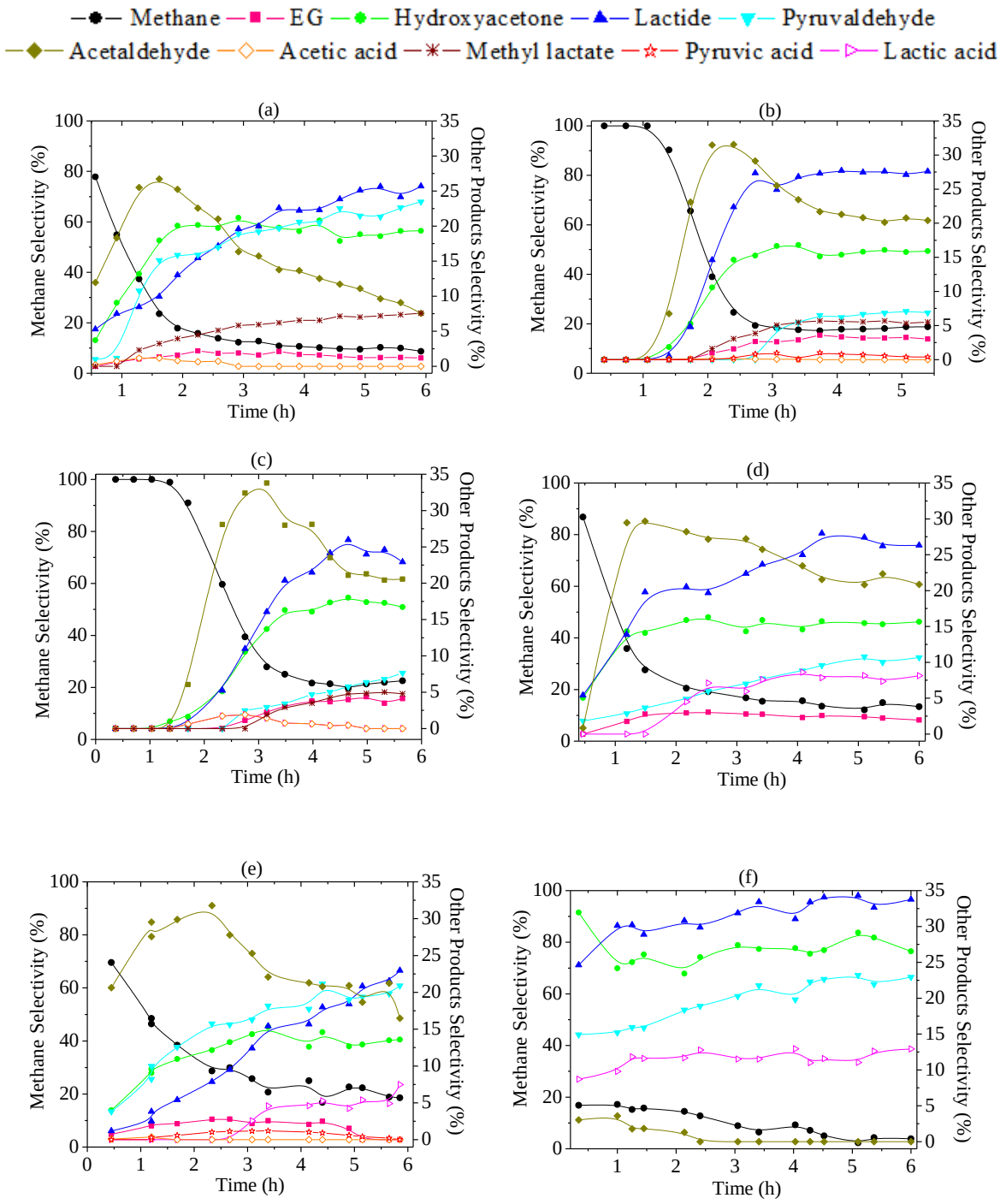

Figure 3.6 Time-on stream product selectivity in glycerol conversion over (a) Ni623, (b) Ni723, (c) Ni823, (d) Ni923, (e) Ni993 and (f) Ni1073

The selectivity to acetaldehyde increases in the first hours, until eventually reaches a maximum and starts to decrease throughout the reaction. For instance, for the Ni723 sample, the selectivity to acetaldehyde increases from 0 % to 31.5 % with raising reaction

time from 1 h to 3 h, and then decreases until 20.4 % at the end of the reaction. During this period of time, the selectivities towards pyruvaldehyde, EG and lactide changes from 0 % to 4.6 %, 2.6 % and 24.9 %, respectively. The lower selectivity is to pyruvic acid, rising to approximately 1.0 % with the increase in reaction time.

The Ni623 and Ni1073 samples have selectivity values for CH_4 of 8.7 % and 3.8 %, respectively, which are lower than those obtained for Ni723, Ni823, Ni923 and Ni993 samples (18.8 %, 22.6 %, 13.3 % and 18.6 %) at 6 h of reaction, respectively (Figure 3.6). The Ni623 and Ni1073 present the lower number of exposed Ni atoms with values of 3.53×10^{18} and 7.67×10^{17}, respectively (Table 3.2). The low selectivity to CH_4 observed for Ni623 sample may be attributed to the low reduction degree of Ni, as shown by H_2-chemisorption (Table 3.2) and XANES (Table 3.1) and larger Ni particles in the case of the Ni1073 (Table 3.2). The increase in the reduction temperature modulates the degree of reduction and sintering of the Ni species affecting the hydrogenolytic capacity of the Ni samples. Table 3.2 shows that Ni723 and Ni823 samples have the higher number of exposed Ni atoms, respectively, leading to higher hydrogenolytic capacity. Indeed the Ni723 sample has the lowest selectivity to pyruvaldehyde at 6 h of reaction, due to its higher hydrogenolytic capacity. At the same time, as noted in Table 3.1 by XANES analysis, the percentage of NiO progressively decreases with the reduction temperature and above 920 K Ni particles are totally reduced.

Even with the progressive decrease in the number of exposed Ni atoms observed above 823 K, the Ni923 and Ni993 samples still present similar CH_4 selectivity values to those obtained for the Ni723 and Ni823 samples (Figure 3.6). The total reduction of Ni species in the Ni923 and Ni993 samples may supply active sites for hydrogenolysis at the expense of the loss in the number of exposed Ni atoms. However, further increase in the reduction temperature above 1000 K causes extensive sintering of the Ni particles as revealed by the TEM results (Figure 3.4 and Table 3.2), becoming less selective to CH_4. Indeed markedly behavior is found for the Ni1073 sample, as shown in Figure 3.6f, which exhibits a stable product distribution with time-on-stream and absence of deactivation.

The deactivation strongly influences the product distribution with time-on-stream during the glycerol conversion. There is a compromise between the reduction temperature pre-treatment employed with stability and catalytic performance. Previous works [2, 4] have reported deactivation in the glycerol hydrogenolysis reaction attributing it to a

number of factors like oxidation of metallic species promoted by the presence of water, sintering of the active metallic phase, and presence of carbon species on the catalytic surface.

3.4 Reaction pathway

Hydroxyacetone, pyruvaldehyde, lactic acid and EG were used as reactants under the same operation conditions performed for the catalytic conversion of glycerol in order to investigate the reaction pathway. The conversion and selectivity obtained during catalytic tests of glycerol, hydroxyacetone, pyruvaldehyde, lactic acid and EG at 4 h of reaction are shown in Table 3.3 for the Ni723 sample.

The glycerol conversion found at 4 h of reaction is about 57 % (column 2, Table 3.3). Acetaldehyde, EG, hydroxyacetone, lactic acid, lactide, CH_4, pyruvaldehyde, methyl lactate and pyruvic acid are the main products, with respective selectivities of 21.3 %, 3.3 %, 15.4 %, 1.9 %, 27.7 %, 17.8 %, 6.2 %, 5.6 % and 0.8 % at 4 h of reaction. Traces of furan derivatives are also detected in the liquid products.

In addition, we have also studied the conversion of glycerol using the Ni723 catalyst under Ar flow (column 3, Table 3.3). The conversion under Ar atmosphere is slightly lower than that observed under H_2 flow as shown in Table 3.3 (46 % and 57 %, respectively). The products are similar to those obtained under H_2 atmosphere, however an increase in the selectivity to lactic acid, lactide, pyruvaldehyde and methyl lactate is observed, mainly at expenses of acetaldehyde and CH_4. This indicates that the dehydration and dehydrogenation routes prevail over the hydrogenolysis route.

The total suppression of CH_4 formation is clearly observed when the Ni catalyst is previously calcined at 723 K instead of reduced as shown in Table 3.3 at column 4. Starting with the Ni catalyst at oxidized state the conversion is very low (9 %) at 4 h of reaction whereas hydroxyacetone, lactic acid, lactide and pyruvaldehyde are the main products. CH_4 and acetaldehyde formation are completed suppressed, suggesting that dehydration and dehydrogenation routes can occur on oxidized Ni while hydrogenolysis are favored on metallic Ni.

Table 3.3 Product selectivity of the main products from the catalytic conversion of glycerol with Ni723 sample at 4 h of reaction

Column 1	**Column 2**	**Column 3**	**Column 4**	**Column 5**	**Column 6**	**Column 7**	**Column 8**
Reactant	Glycerol	Glycerol	Glycerol	Hydroxyacetone	Pyruvaldehyde	Lactic acid	EG
Molar ratio H_2/reactant	10	0 [a]	10 [b]	10	10	10	10
Conversion (%)	57	46	9	16	71	30	100
Selectivity (%)							
Acetaldehyde	21.3	3.4	-	11.2	16.1	2.0	-
Acetic acid	-	-	-	-	5.4	2.1	-
Ethylene glycol	3.3	-	-	-	-	-	-
Hydroxyacetone	15.4	16.5	29.5	-	13.2	9.1	-
Lactic acid	1.9	6.0	12.2	61.0	15.2	-	-
Lactide	27.7	36.6	35.4	13.7	-	7.1	-
Methane	17.8	9.6	-	14.0	9.7	18.4	100
Pyruvaldehyde	6.2	14.9	22.8	-	-	-	-
Methyl lactate	5.6	12.9	-	-	30.3	-	-
Pyruvic acid	0.8	-	-	-	10.1	61.2	-
Mass balance [c] (%)	91	87	92	90	100	100	100

[a] Argon atmosphere, [b] NiO catalyst, [c] TOC, HPLC and GC analysis

The main products obtained when hydroxyacetone is employed as reactant (column 5, Table 3.3) are lactic acid, lactide, acetaldehyde and CH_4. Based on previous works the acetaldehyde and the CH_4 can be obtained from the catalytic C-C bond cleavage of hydroxyacetone [13]. The hydroxyacetone can also be dehydrogenated towards pyruvaldehyde, which finally may give lactic acid (LA) by an intramolecular Cannizzaro reaction [14] and lactide, which is a cyclic dimmer obtained from lactic acid.

Hydroxyacetone, lactic acid, methyl lactate, pyruvic acid, acetic acid, acetaldehyde and CH_4 are the major products during catalytic conversion of pyruvaldehyde with correspondent selectivity of 13.2 %, 15.2 %, 30.3 %, 10.1 %, 5.4 %, 16.1 % and 9.7 % (column 6, Table 3.3). These results suggest that hydroxyacetone may be formed not only from direct dehydration of glycerol but also from the hydrogenation of pyruvaldehyde.

When lactic acid is employed as reactant (column 7, Table 3.3), the main products obtained are hydroxyacetone, lactide, pyruvic acid, acetic acid, acetaldehyde and CH_4 Concerning the products from EG (column 8, Table 3.3), the only product observed is CH_4. The most severe deactivation is reached when the hydroxyacetone is used as test molecule, showing a conversion of 16 % at 4 h of reaction.

Taking into account all the previously catalytic results stated in Table 3.3, it is possible to propose a general reaction pathway for glycerol conversion (Scheme 3.1). Glycerol is consumed by dehydration reaction to form hydroxyacetone. The hydroxyacetone is dehydrogenated to form pyruvaldehyde. The results show that pyruvaldehyde can be hydrogenated to form hydroxyacetone, which is hydrogenated in a trace level towards 1,2-PDO. The formation of 1,2-PDO by the metal-acid bifunctional catalyst system is explained by the mechanism where the acid function plays a role of dehydration reaction and the metal catalyzes the hydrogenation reaction [14].

On the other hand, pyruvaldehyde can be converted to lactic acid either via a Cannizzaro reaction [14] or via oxidation to pyruvic acid which can further hydrogenate forming lactic acid in a reverse reaction. Finally the lactic acid undergoes dimerization to form lactide. Additionally, the pyruvic acid can esterify with methanol forming methyl pyruvate in a minor level. Methyl lactate is also detected that can be produced by esterification between methanol and lactic acid. Methanol is formed in the direct hydrogenolysis step of glycerol. The methyl pyruvate can also hydrogenate to methyl lactate.

Acrolein, 3-hydroxypropanal, and 1,3-PDO are not detected in our experimental conditions. The preferable formation of hydroxyacetone to 3-hydroxypropanal is probably due to the thermodynamic stability of hydroxyacetone [15]. Another route observed in the glycerol conversion is related to EG formation. However, EG is not detected in the experiments when hydroxyacetone, pyruvaldehyde and lactic acid are reactants, suggesting that EG is formed by direct hydrogenolysis of glycerol.

CH_4 and acetaldehyde are also obtained in the glycerol conversion reaction. The first can be obtained by progressive steps of hydrogenation of pyruvaldehyde and hydroxyacetone, and simultaneously also by direct hydrogenolysis of glycerol. Methanol is observed at trace level, which may be produced from the direct hydrogenolysis of glycerol, undergoing degradation towards CH_4 and esterification of pyruvic acid and lactic acid forming methyl pyruvate and methyl lactate, respectively.

Both CH_4 and acetaldehyde are also obtained when hydroxyacetone, pyruvaldehyde and lactic acid are used as reactants. The acetaldehyde may be obtained from the C-C cleavage of the hydroxyacetone as has been already mentioned by previous works [13]. Acetaldehyde afterwards is oxidized in minor extension to acetic acid. Traces of formaldehyde and formic acid are also detected, which may come from the cleavage of hydroxyacetone. Formic acid is formed by oxidation of formaldehyde. Acetone and propanal are also detected as trace products, derived probably by dehydration of 1,2 PDO. The observed traces of 2-PO and 1-PO may originate during the hydrogenation of acetone and propanal, respectively.

3.5 Characterization of the used catalysts

The formation of carbonaceous deposits is an undesired side reaction [16]. It has previously been demonstrated that the deactivation of Ni-supported catalysts by carbon deposits is due to both the presence of carbonaceous residues and of partially dehydrogenated and dehydrated species [4, 17]. The deposited carbon may have different structures, orders, morphologies and reactivity depending on reaction conditions and on the structure of the catalyst [18]. Polymeric, filamentous and graphitic carbon can be formed on the catalyst [19, 20]. The deactivation of the Ni/γ-Al_2O_3 catalysts during the conversion of glycerol can be assigned to a number of factors, as hinted by the characterization of the used samples.

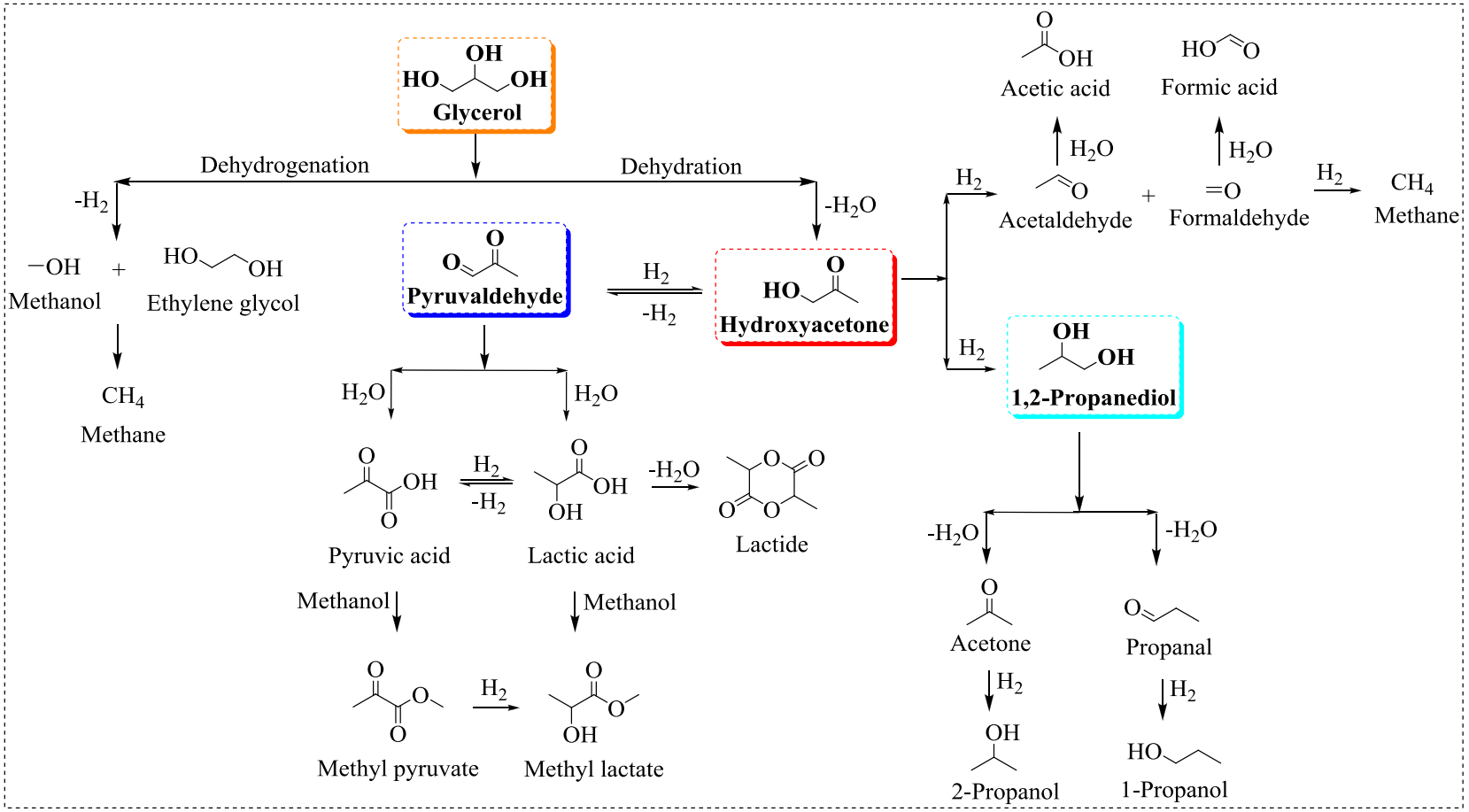

Scheme 3.1 Proposed general reaction pathway for glycerol conversion over the Ni/γ-Al_2O_3 catalysts

The textural properties measured by N_2-physisorption of fresh (Table 3.1) and used catalysts (Table 3.4) are similar, suggesting that the deactivation may not be dependent on the changes in surface area, pore volume, and pore size of the catalyst during the catalytic conversion of glycerol.

Table 3.4 Results of N_2-physisorption and TPO of the used Ni/γ-Al_2O_3 catalysts

Sample	S_{BET} (m^2/g)	Pore volume (cm^3/g)	Pore size (nm)	TEM [a] (nm)	TPO (wt% C)	I_D/I_G
Ni623	89	0.13	4.15	3.0	5.97	1.71
Ni723	99	0.15	4.54	6.0	5.75	1.59
Ni823	95	0.17	4.54	9.0	1.88	1.41
Ni923	91	0.18	4.75	21.0	1.69	2.80
Ni993	71	0.16	5.44	21.0	1.53	1.98
Ni1073	70	0.15	5.44	22.0	0.74	4.51

[a] Mean particle size

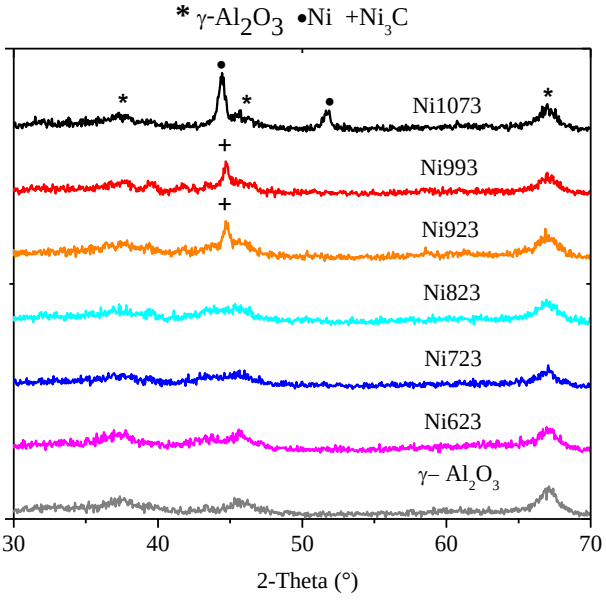

Figure 3.7 X-ray diffraction patterns of the used Ni/γ-Al_2O_3 catalysts

XRD shows differences between fresh (Figure 3.3) and used catalysts (Figure 3.7). Only the γ-Al_2O_3 phase is observed in the XRD patterns of the Ni623, Ni723 and Ni823 samples. In sample Ni1073, the Ni metallic phase is also discerned. Nickel carbide (Ni_3C, ICDD 6-697) is observed for the used Ni923 and Ni993 samples (Figure 3.7). Previous work [21] observed the formation of Ni_3C during reaction between diethyl ether and

hydrogen. Therefore, deactivation observed during glycerol conversion could be attributed to formation of Ni_3C. Wang et al. [22], mentioned that the transformation from Ni to Ni_3C is easy during dry reforming, and metallic Ni catalysts are more active than those of Ni_3C, and therefore, the phase transformation from Ni to Ni_3C will reduce the activity, on the Ni_3C surfaces, coke is more likely to form [23].

TEM of the used samples reveal no variation in the Ni particle size distribution (Figure 3.8a and b) with respect to the fresh samples (Figure 3.4a and b). The sintering process is not observed for the Ni samples during the reaction, suggesting that it is not responsible for the catalyst deactivation.

TPO analyses of the used Ni/γ-Al_2O_3 samples in Figure 3.9 show a broad peak together with a shoulder, where two distinct temperatures are observed. The low temperature peak at around 550 K is attributed to CO_2 coming from the oxidation of intermediary species and superficial carbon, carbon formations or adsorbed species close to the metallic particles [8, 19, 43] . The high-temperature TPO peak (e.g., 610 K) is associated with the oxidation of more structured carbon (filaments) and/or carbon or adsorbed species deposited on the solids [19]. However, these peaks could indicate the oxidation of similar carbon deposits. As the reduction temperature increases, the peaks have a lesser intensity, indicating minor carbon deposition.

The amounts of carbon deposition on used Ni/γ-Al_2O_3 catalysts determined by TPO are shown in Table 3.4. As the reduction temperature of pre-treatment increases, less carbon is formed on the catalyst. The used Ni623 contained the highest amount of coke (5.97 wt%) and the used Ni1073 the lowest (0.74 wt%). TPO and catalytic activity results show that deposition of carbon species on the surface of the catalyst decreases greatly the availability of the required active centers and consequently depress the overall activity [24, 25]. Therefore, carbon deposition on the catalyst during the catalytic conversion of glycerol is also a source of the observed deactivation.

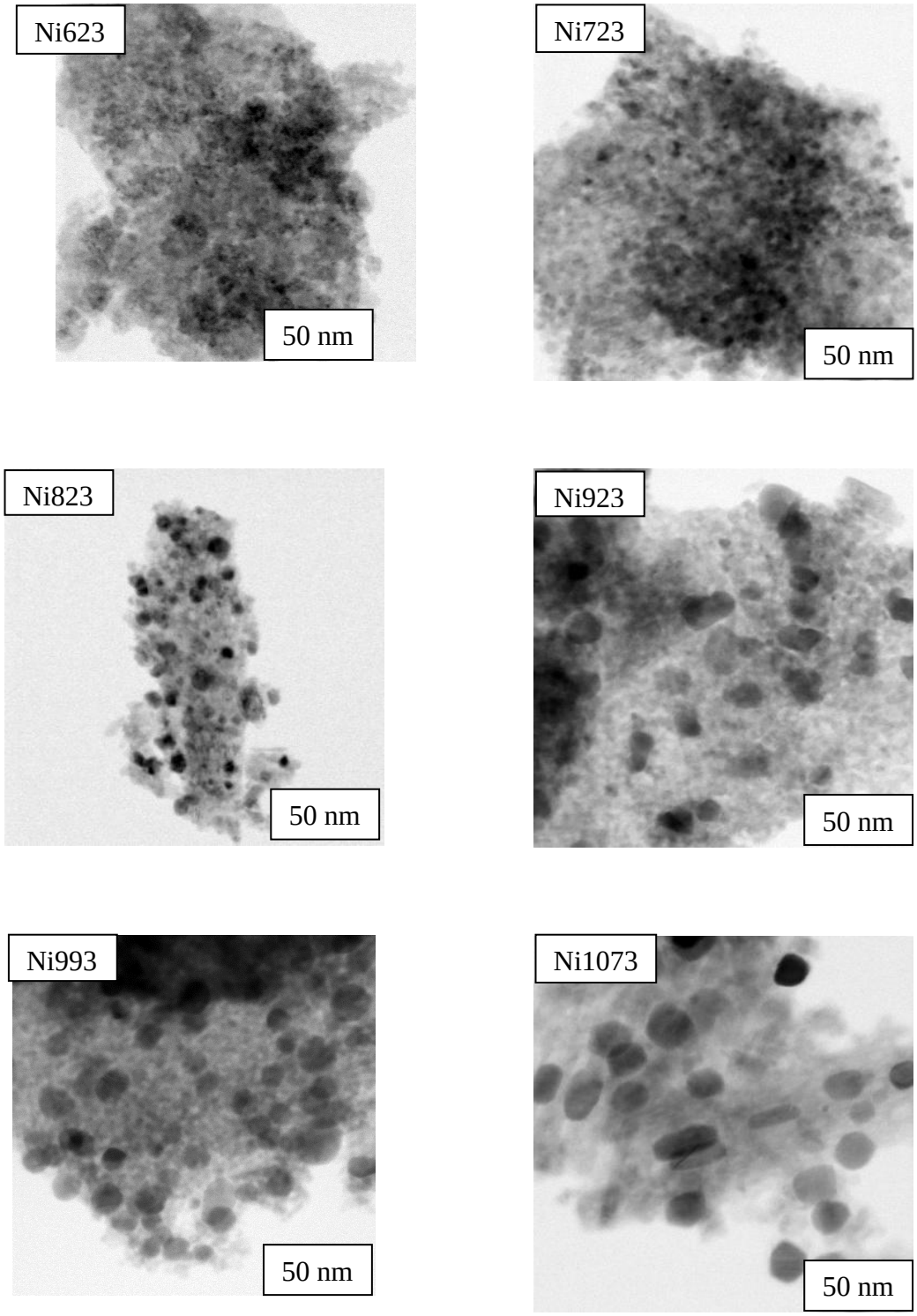

Figure 3.8(a) TEM images of the Ni/γ-Al_2O_3 used samples

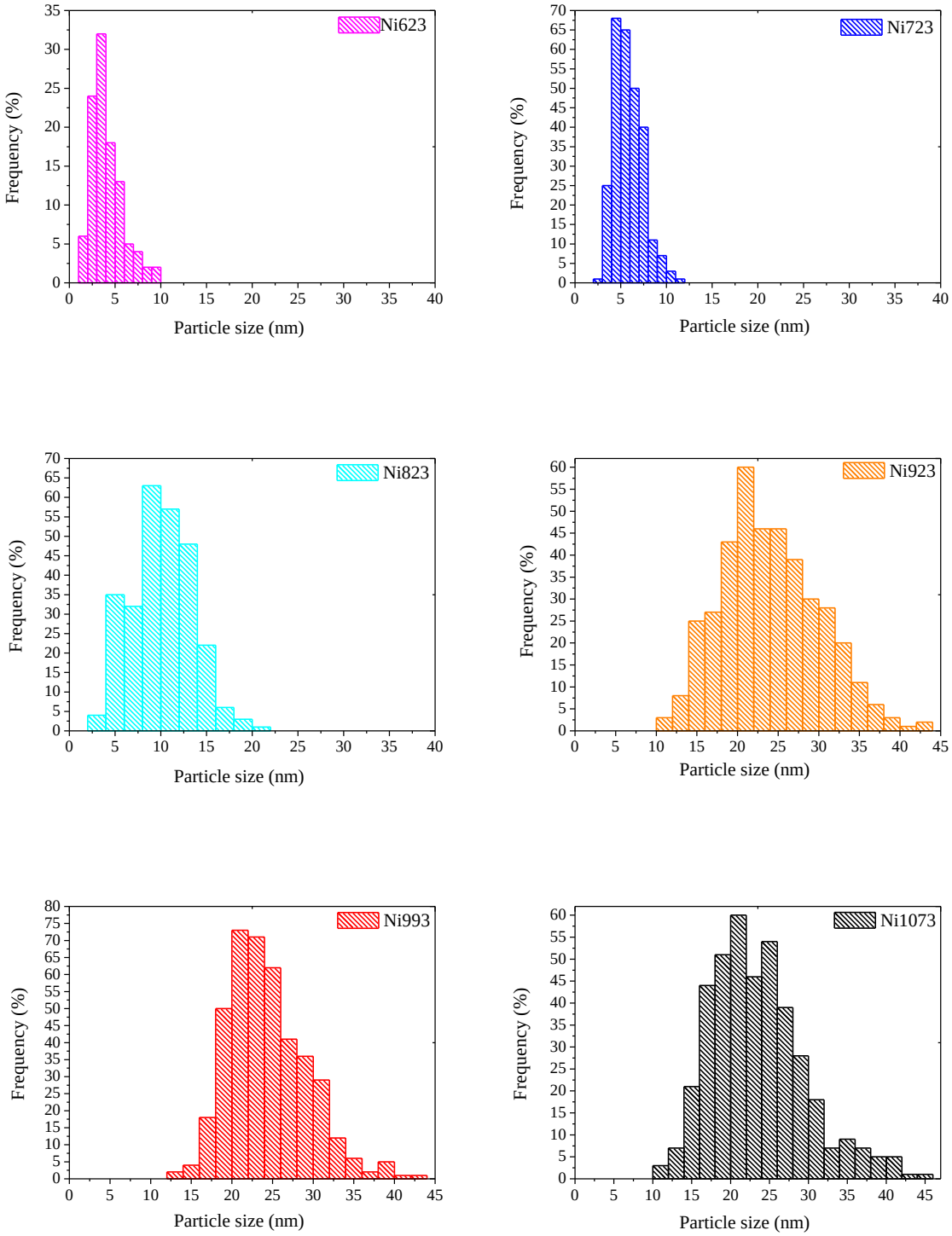

Figure 3.8(b) Nickel particle size distributions of the used Ni/γ-Al_2O_3 samples

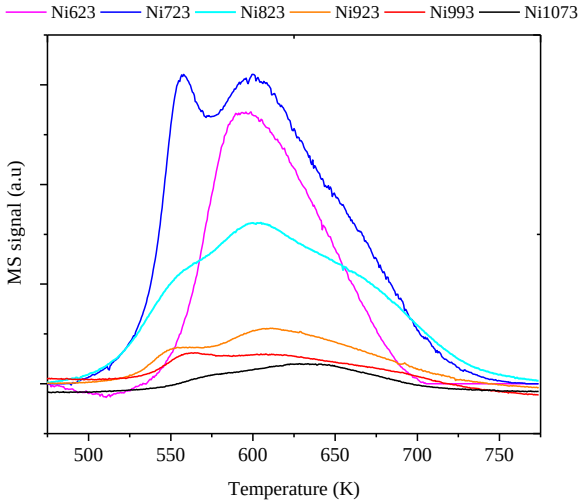

Figure 3.9 TPO profiles of the used Ni/γ-Al_2O_3 samples

The quantification of the total acid sites obtained by NH_3-TPD analysis is expressed in Table 3.2. The Ni623 presents the higher amount of acid sites among all catalysts, as well as the higher amount of carbon deposited on the catalyst, suggesting that the carbon on the catalyst is formed during dehydration reactions on the acid sites. In addition, except for the Ni1073 sample, all catalysts show high selectivity to CH_4 at the beginning of the reaction (Figure 3.6), suggesting that glycerol is degraded to form lower-molecular alcohols and gases via hydroxyacetone and direct hydrogenolysis of glycerol (Scheme 3.1). Atia et al. [26] observed catalyst deactivation during dehydration of glycerol on heteropolyacid catalysts and they attributed it to the blocking of the catalyst surface by carbon, which was related to the catalyst acidity and pore size. Similarly, Vasiliadou and Lemonidou [27] observed deactivation by carbon during glycerol hydrogenolysis on Cu catalysts.

The effect of the total acidity on the catalytic performance must be pointed out, particularly for the Ni623 sample. Its total acidity of 273 μmol NH_3/g_{sample} is the highest one. Indeed, as based on Figure 3.5 it is possible to distinguish that the deactivation for this sample is the most severe among all samples. This sample has also the highest level of carbon deposition (5.97 wt%) as determined by TPO (Table 3.4). In contrast, the total acidity among the other samples recorded in Table 3.2 varied by less than 10 %. Then, the acid sites contribute to the formation of carbon by the dehydration route.

Some contribution of metallic Ni to the formation of carbon by hydrogenolysis could be expected. This is remarkable for Ni723 sample which presents the higher number of exposed Ni atoms. It is well known that carbon deposition is also a consequence of the ability of the Ni to break the C-C bond producing CH_4 by hydrogenolysis reaction. Also, the carbon deposition on the catalyst depends on the Ni particles size (Table 3.2). Larger Ni particles produce lower amount of carbon deposition. The highest reduction temperature employed for the Ni1073 sample induced Ni sintering, resulting in loss of exposed Ni atoms and therefore it decreased the hydrogenolysis routes and formation of carbon on the catalyst, as can be observed in Table 3.4. Therefore, Ni particles size plays an important role in the glycerol conversion.

Raman spectroscopy was performed on the used catalysts in order to investigate the carbon formed on the samples. It is known that light absorption by carbon depend on the compounds present in the reaction medium and on the deactivation conditions [28].

Raman spectra (Figure 3.10) in the range of 300 cm^{-1} to 800 cm^{-1} show signals that can be contribution of NiO vibrations, specially for the Ni623 sample that shows a peak between 400 cm^{-1} and 600 cm^{-1}, and the Ni723 sample that shows a peak between 300 cm^{-1} and 450 cm^{-1}. In addition, another signal at around 730 cm^{-1} is assigned to NiO as it was proved by Mendoza et al. [29]. Raman spectra in the high wavenumber region display two bands centered at about 1347 $cm^{-1}$and 1590 cm^{-1}, which are associated with the defect and graphite modes, e.g., D-band and G-band, respectively [30].

According to previous works [30-32], the D-band is associated to the disorder-induced vibration of C-C bond and the G-band is related to the C-C vibration of the carbon material with a sp^2 orbital structure. These findings suggest that the carbon species found on the surface of Ni-based catalysts consist of non-deactivating carbon (amorphous carbon) and deactivating carbon (graphitic carbon), respectively. In addition, Ni_3C formed could be attributed to the fact that at the gas/metal interface, carbon is in the form of a solute dissolved in Ni as a solvent, forming an unstable intermediate of surface nickel carbide [23].

The ratios of the intensities of D and G bands (I_D/I_G) were calculated as the ratio of their peak areas. The results are shown in Table 3.4 and they indicate that amorphous carbon deposition on the solid is too high. For the samples reduced at temperatures above 823 K, the intensity of both bands became weak, although the same features observed at

other temperatures remained, which is sound proof that elevated temperatures deteriorate the catalyst due to fast carbon deposition on the solid surface. The intensity of these bands correlates well with the amount of deposited carbon determined by TPO.

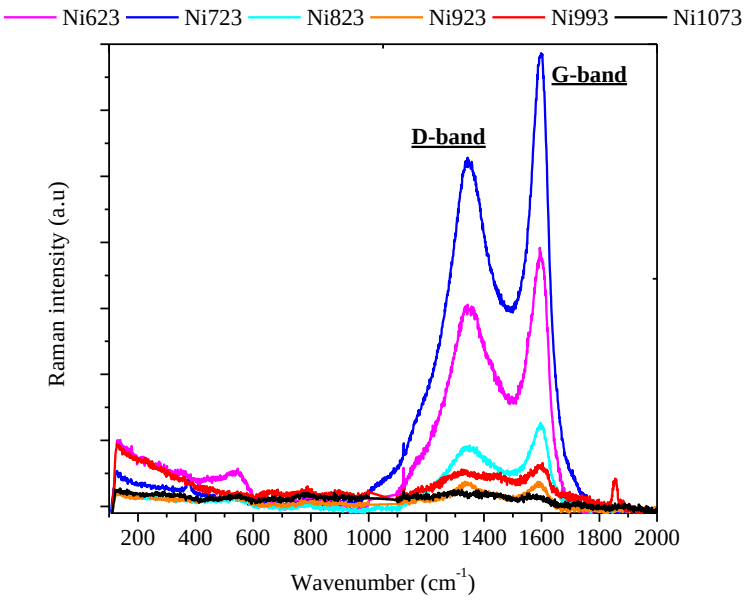

Figure 3.10 Raman spectra of the used Ni/γ-Al_2O_3 catalysts

The carbon deposition during the initial time on stream is important in the investigation because the catalytic activity greatly decreased during the first 2 h of reaction, as shown in Figure 3.5. The effect of time on stream on carbon deposition was investigated for the Ni723 sample in order to get insights into this deactivation process. Carbon deposition was evaluated in different periods of reaction (1 h, 2 h, and 3 h). The XPS and TPO results presented in Table 3.5 reinforce the evidence of carbon species over Ni/γ-Al_2O_3 used materials. By comparing the amount of carbonaceous species deposited on the used catalysts by TPO, it is observed in Table 3.5 that the Ni723 catalyst has less carbonaceous deposits after 1 h of reaction than 2 h and 3 h, suggesting that the deposit accumulates. As the reaction time increases from 1 h to 6 h, the carbonaceous deposits increase from 3.65 wt% to 5.75 wt%.

Table 3.5 Surface atomic ratio determined by XPS and TPO results of the used Ni723 sample after different times of reaction

Time of reaction (h)	Surface atomic ratio by XPS			TPO (wt% C)
	Ni/Al	C/Ni	C/Al	
0 h	0.13	1.30	0.17	-
1 h	-	-	-	3.65
2 h	0.14	2.08	0.28	4.39
3 h	0.12	3.45	0.40	5.57
4 h	-	-	-	5.21
6 h	0.30	10	2.9	5.75

The Ni723 used sample was also evaluated by XPS to provide information about the oxidation state and chemical environment of the elements present on the surface of the catalyst (Table 3.5). During 6 h of reaction, the C/Ni atomic ratio clearly increases, changing from 2.08 after 2 h of reaction to 10 after 6 h of reaction. This indicates a progressive increase in the carbonaceous species over Ni producing some deactivation of the catalyst (Figure 3.5). A similar tendency is noted for the C/Al atomic ratio indicating an accumulation of carbonaceous deposits over alumina as the reaction progresses. The Ni/Al atomic ratio increases from the fresh condition compared with the used catalysts after 6 h of reaction, reinforcing the idea that carbonaceous deposits accumulate more over the surface of the support than over the metal particle.

It was performed HRTEM analysis of the used Ni923 sample in order to contribute with the determination of the catalyst composition after reaction. HRTEM shows that the used Ni923 sample is composed of 6 nm–10 nm Al_2O_3 crystallites and 15 nm–20 nm Ni-containing particles (Figure 3.11a). Both kinds of particles are crystalline. Lattice-fringe analysis and Fourier Transform (FT) images reveal spots at 1.76 Å and 2.04 Å in particle labeled “a”, which are ascribed to (200) and (111) crystallographic planes of metallic Ni, respectively. On the other hand, particle labeled “b” exhibits lattice fringes at 3.50 Å, which are ascribed to (110) planes of NiO. Therefore, both Ni and NiO phases are present.

In some cases these two phases occur in separate particles, but in most cases, however, they appear intimately mixed within the same particle. Figure 3.11b, for example, shows a particle with highly inhomogeneous contrast. Its FT image reveals the presence of spots at 2.04 Å and 2.42 Å, which correspond to (111) crystallographic planes of Ni and NiO, respectively. Figure 3.11b also shows the occurrence of carbon deposition around this particle. The carbon phase is poorly-defined and close to amorphous carbon.

Lattice fringes are hardly seen, but a tentative spacing larger than 3.9 Å can be measured (much larger than that of graphitized carbon). Carbon deposition is also evident over the Al_2O_3 support.

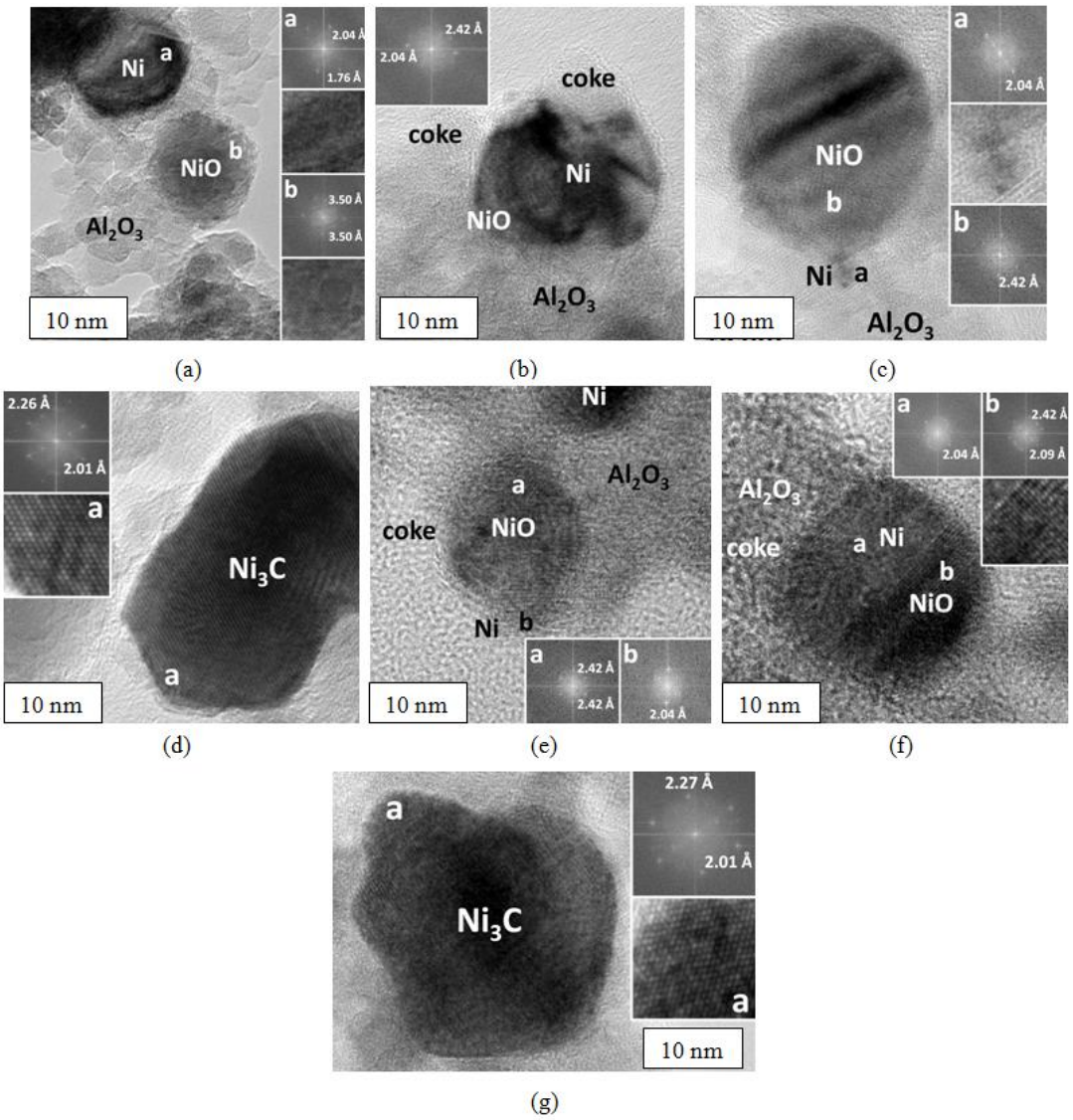

Figure 3.11 HRTEM images of used Ni923 catalyst. Fourier transform images are included

Figure 3.11c shows a NiO particle exhibiting (111) crystallographic planes at 2.42 Å (labeled "b") and lattice fringes at 2.04 Å (labeled "a"), characteristic of the (111) crystallographic planes of metallic Ni. Exactly the same situation is observed in Figure 3.11(d). In this case, particle "a" corresponds to NiO (spots in the FT image at 2.42 Å), and

the small particle labeled "b" attached to it shows the characteristic lattice spacing at 2.04 Å of metallic Ni. A thin layer of carbonaceous deposits is also observed. A last example is depicted in Figure 3.11e. Again, both NiO and Ni are identified in the same particle. Area labeled "a" shows lattice fringes at 2.04 Å corresponding to (111) crystallographic planes of metallic Ni, whereas area labeled "b" shows spots at 2.09 Å and 2.42 Å, which are ascribed to (200) and (111) crystallographic planes of NiO.

Furthermore, Figure 3.12 shows the XPS spectrum of the Ni723 sample after 6 h of reaction. The Ni 2p core-level is composed of two components, Ni $2p_{3/2}$ and Ni $2p_{1/2}$ (which result from the spin orbital splitting) and shake up satellites. The Ni $2p_{3/2}$ core level spectra shows primary satellite peaks at around 862.5 eV due to shake-up electrons. Wherever the lines shape of the Ni $2p_{3/2}$ and Ni $2p_{1/2}$ peaks are unsymmetrical and broad. In the surface of the Ni723 sample after 6 h of reaction, Ni appears in XPS spectra in two forms: one corresponds to metallic Ni and has the line of Ni $2p_{3/2}$ level at 852.3 eV and the second form corresponds to ionic nickel (Ni^{+2}), with binding energies of about 855.1 eV, due to superficial NiO [33, 34]. The presence of NiO could be another source of deactivation of the Ni catalyst as mentioned in section 3.4, the conversion of glycerol was very low (9 %) at 4 h of reaction when it was started with the Ni catalyst at oxidized state (instead of reduced).

Therefore, the deactivation observed for the Ni catalysts seem not only is related with the carbonaceous deposition. The deactivation could also be due to the oxidation of the metallic Ni phase, as it is revealed by HRTEM and XPS, which could be promoted by the presence of water vapor in the reaction medium [35]. The steam quickly oxidizes the Ni metal deactivating it [36]. Iriondo et al. [37] founded that XPS analyses of Ni catalysts indicate that the main reason for the observed deactivation phenomena can be ascribed to the gradual change of the Ni state under reaction conditions from metallic to oxidize with formation of surface oxidized species.

The deactivation of the Ni species due to its reoxidation was observed by Wen et al. [38], who found that the Ni atoms are highly susceptible to oxidation by water excess at low temperatures, since the oxidized Ni is inactive for the glycerol aqueous-phase reforming (APR) at low temperature. Their results were in good agreement with El Doukkali et al. [39]. Shabaker et al. [40] reported that reduced Ni particles lose catalytic activity due to oxidation by interactions with water during APR reaction. This Ni

reoxidation can be related to the aggressive hydrothermal conditions due to the presence of high quantity of water, which performs as oxidizing agent during the glycerol APR process.

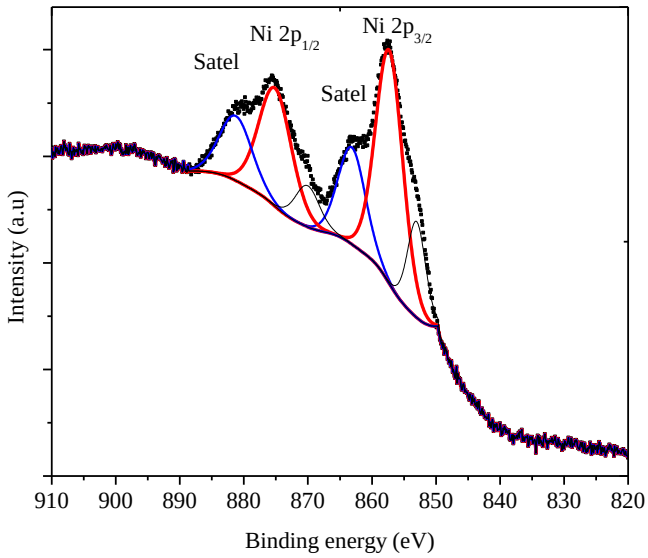

Figure 3.12 XPS spectra of Ni723 sample after 6 hours of reaction

Carbonaceous deposition is also observed by HRTEM to occur both over the Ni-containing particle as well as over the γ-Al_2O_3 support. Large particles exceeding 30 nm in size are observed. These large particles are difficult to characterize by HRTEM due to their thickness (electron opacity), but at the outer rim it is possible to obtain lattice fringe images. Figure 3.11f and g show two of these large particles. In Figure 3.11f, the inset shows the area labeled "a" at high magnification, where it can be observed an excellent crystalline nature. The Fourier Transform image (FT) corresponding to the area "a" shows sharp spots at 2.01 Å and 2.26 Å, which correspond to (113) and (110) crystallographic planes of Ni_3C. A similar analysis is performed in Figure 3.11g. Therefore, there is no doubt that, in addition to small Ni and NiO particles, there are also Ni_3C crystals. These Ni_3C particles are large and very well crystallized, as observed by XRD (Figure 3.7). Ni and NiO particles are less crystalline and smaller, making their analysis by XRD more difficult. By HRTEM, Ni, NiO and Ni_3C are detected.

Therefore, based on all results obtained, coke formation, transformation of Ni phase to Ni_3C, as well as oxidation of the Ni phase during the reaction, seems to be the

responsible of the deactivation of Ni-containing catalyst employed in the hydrogenolysis of glycerol. This is illustrated in Figure 3.13.

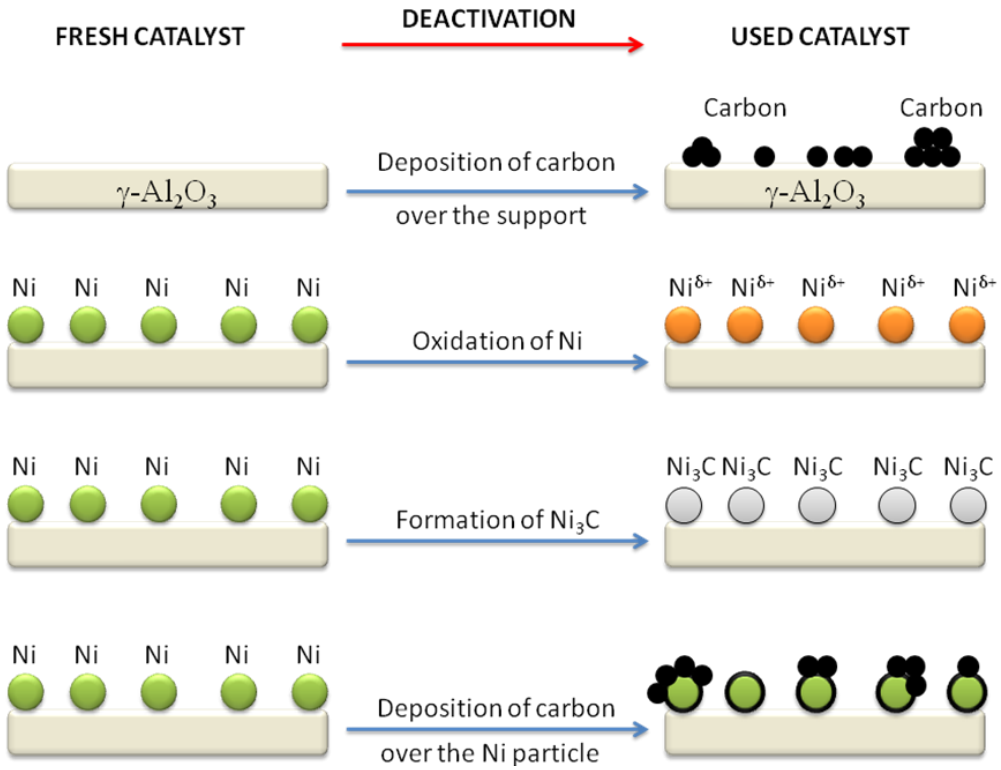

Figure 3.13 Diagram of deactivation sources of the Ni/γ-Al_2O_3 catalysts

3.6 Regeneration

The Ni723 sample was used as a representative sample for further studies about the regeneration process of the Ni/γ-Al_2O_3 catalysts. Figure 3.14 shows the conversion of glycerol and selectivity profiles of the different products, obtained in the catalytic transformation of glycerol over the Ni723 sample for three hydrogenolysis cycles. The selectivity to deep hydrogenolysis products such as CH_4 decreases with time of reaction whereas dehydration-dehydrogenation products (such as hydroxyacetone) increase with time.

For the first cycle (Figure 3.14b), initially the selectivity to CH_4 is about 100 % and with further time of reaction it decreases progressively to about 20 % remaining unchanged with further reaction time. The selectivity to acetaldehyde reaches a maximum in the first hours of reaction and starts to decrease until about 15 % at 6 h of reaction. The selectivity to hydroxyacetone increases from 6.2 % to 14.5 % between 2 h and 4 h of reaction.

Selectivities during this period towards pyruvaldehyde, lactide and lactic acid change from 2.0 % to 6.7 %, 6.4 % to 19.4 % and 0 % to 0.7 %, respectively. Products of esterification such as methyl lactate are also observed. Figure 3.14a for the first cycle shows that the Ni sample suffers deactivation, the glycerol conversion decreases from 100 % to about 60 % upon raising the reaction time to 6 h.

The catalytic performance of the Ni catalyst was tested after cycles of regeneration (oxidation-reduction steps). The activity lost in the catalyst after 6 h of reaction due to deactivation is fully recovery back by regeneration. After three runs it is observed that the decrease in activity is similar with that of the first run. Figure 3.14 shows that the catalyst regeneration by oxidation-reduction steps at 723 K is sufficient to regain full catalytic activity. The product distribution and glycerol conversion just before the deactivation process and after regeneration are similar in trend of conversion and selectivity, since the catalyst recovered the conversion of a highly active surface after regeneration.

Deactivation occurred during all reaction cycles (Figure 3.14). The deactivation observed in the course of the reaction is attributed to Ni oxidation [40], deposition of carbon [22, 41, 42], and formation of Ni_3C [23], as was mentioned before. This is reinforced by our HRTEM, XRD and FTIR of adsorbed CO analyses. Figure 3.15a and b illustrate the HRTEM image of the catalyst after reaction. It can be seen that the sample after reaction contains metallic Ni particles of about 3 nm–6 nm. Some particles are clearly covered by carbonaceous deposits. In the Figure 3.15a is observed a particle with the label "a" which contains a ring at 3.5 Å in the FT image. This value corresponds to the spacing of carbon which is clearly surrounding the particle. Indeed Figure 3.15 reveals that carbon species are deposited over Ni and alumina surfaces. For solid acid catalysts, the carbon species are deposited on the strongest acid sites [43]. The particle spacing at 2.3 Å and 2.1 Å (Figure 3.15a) correspond to the planes (110) and (006) of the Ni_3C, respectively. There are other metal particles showing spaced 2.0 Å. These may be Ni_3C corresponding to the plane (113) but also to the plane (111) of the metallic Ni. Previous work dedicated on the adsorption of CH_4 at 573 K on SiO_2 supported Ni catalysts concluded that carburizing of Ni catalysts with CH_4 results in the formation of surface carbide. The chemisorption of CH_4 was found to be dissociative according to the reaction $CH_4+7Ni \rightarrow Ni_3C$ [44].

The regenerated Ni/γ-Al_2O_3 catalyst is different. In this case the metal particles are somewhat smaller, between 2 nm and 5 nm (Figure 3.15c, d, and e). The HRTEM analysis

reveals planes at 2.0 Å, so that the particles can be Ni_3C or Ni. However, what is clear is that the oxidation treatment virtually eliminates the deposited carbon species [42].

The absence of carbon and the slight decrease in particle size suggest that the Ni_3C species are decomposed and metallic Ni species are obtained after the oxidation-reduction regeneration process. Catalytic sites blocked by chemisorbed carbon species such as by carbide surface species is generally reversibly in hydrogen or oxygen atmosphere [25]. According of previous findings, the combustion of the amorphous carbon is around 573 K [45], and Ni_3C decomposes at above 623 K [46] into metallic Ni and free carbon ($Ni_3C \rightarrow 3Ni + C$) [47].

The XRD patterns of each step of regeneration for the Ni catalyst are presented in Figure 3.16 (Ni923 sample). After reaction it is observed that carbinding of Ni occurred (Figure 3.16a). It is important to mention that during the oxidation process the Ni_3C disappears forming a NiO phase (Figure 3.16b) which, after reduction, forms again the Ni phase (Figure 3.16c). The regeneration process was applied in between each catalytic cycle. The regeneration process was repeated for two cycles with the catalyst being fully reactivated in all cases (Figure 3.14). As already mentioned for the results in Table 3.3, when the used Ni catalyst is activated by calcination without the reduction step, it results in low catalytic activity. Thus, the reduction step is crucial to activate the Ni sites.

The effect of the catalytic transformation of glycerol on the Ni catalyst surface was investigated by FTIR of adsorbed CO at RT and at 100 K as shown in Figure 3.17. It presents the spectra recorded at RT and 100 K of the fresh and used Ni samples upon successive addition of CO increments and evacuation. At first glance, CO adsorption can be observed in different zones both in the fresh and used samples (Ni723). The C-O stretching modes of surface Ni^{+2}-CO compounds are usually observed at 2220 cm^{-1}–2180 cm^{-1} [48]. The absorption bands of linear Ni^{+}-CO complexes are in general detected at lower frequencies (2160 cm^{-1}–2110 cm^{-1}) [49]. Generally the frequency band at 2100 cm^{-1}–2000 cm^{-1} can be assigned to linear adsorbed CO on metallic Ni species. The low frequency band at 2000 cm^{-1}–1800 cm^{-1} is attributed to two or three fold bridge adsorbed CO on metallic Ni species [50]. The bands at 1879 cm^{-1}–1796 cm^{-1} are attributed to Ni_3CO and Ni_4CO species [51].

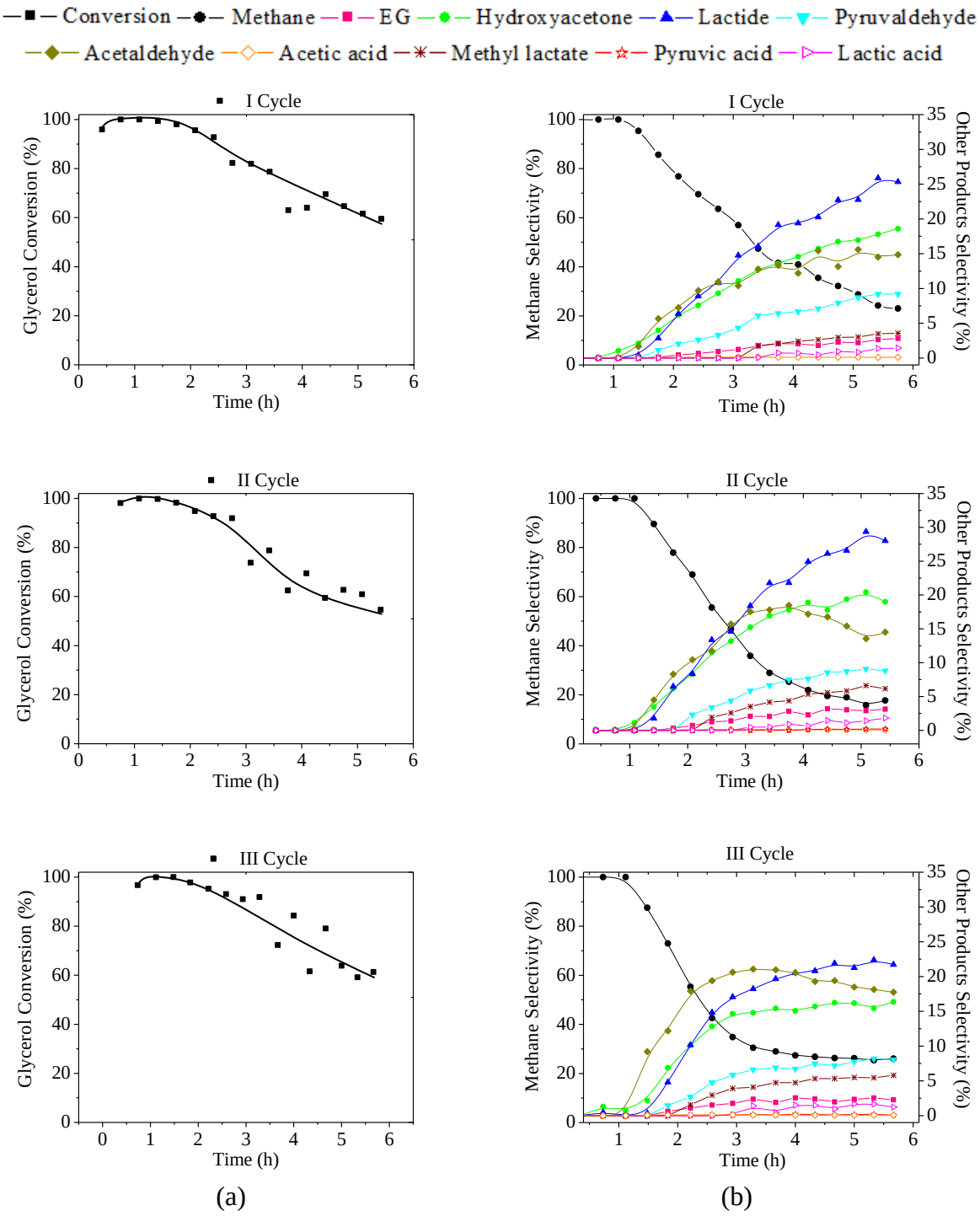

Figure 3.14 (a) Catalytic behaviour, and (b) Time-on stream product selectivity in glycerol conversion of the Ni723 catalyst for three cycles of regeneration

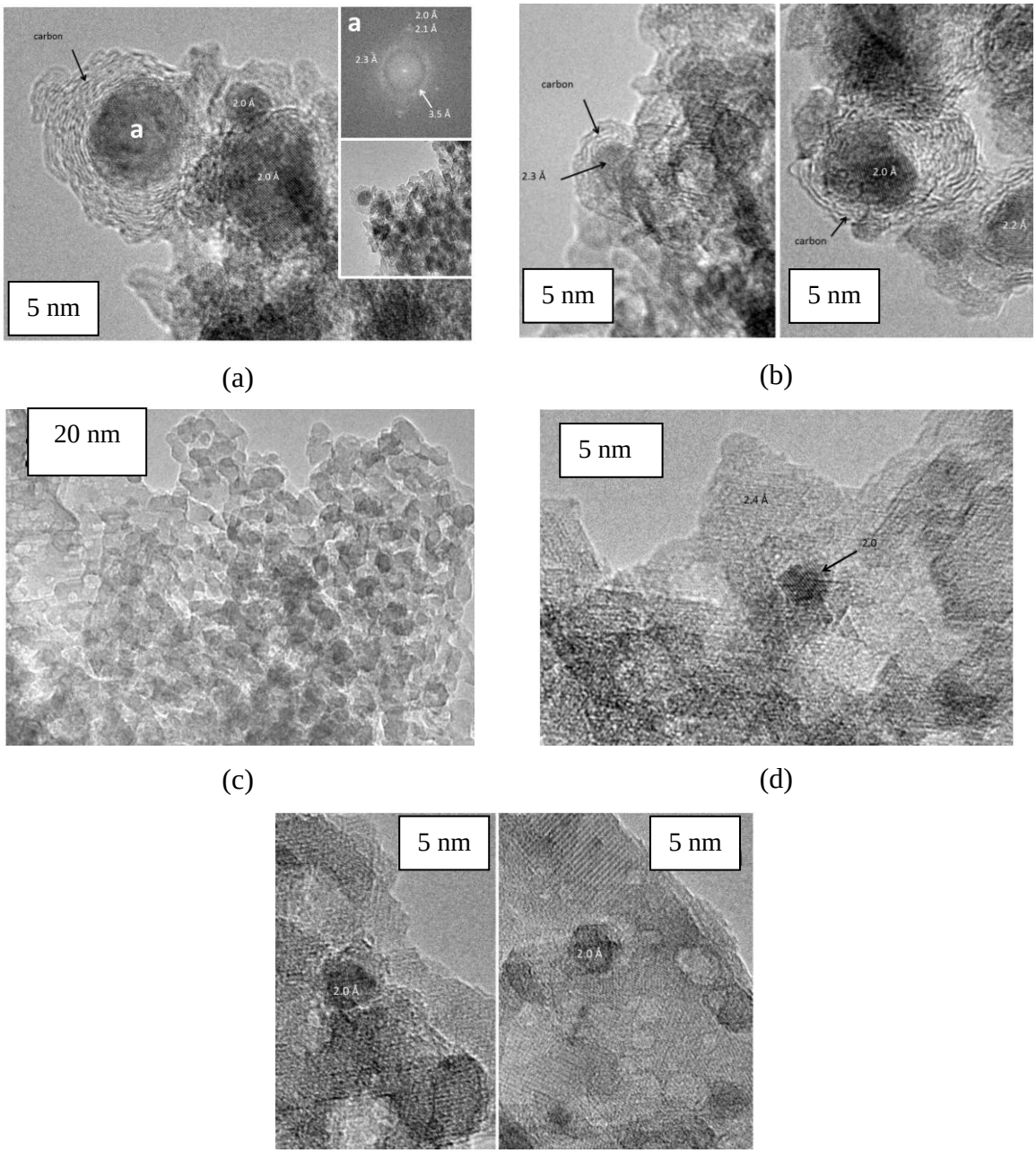

Figure 3.15 HRTEM images of the Ni723 catalyst: (a, b) after reaction, and (c, d, e) after regeneration process. Fourier transform images are included

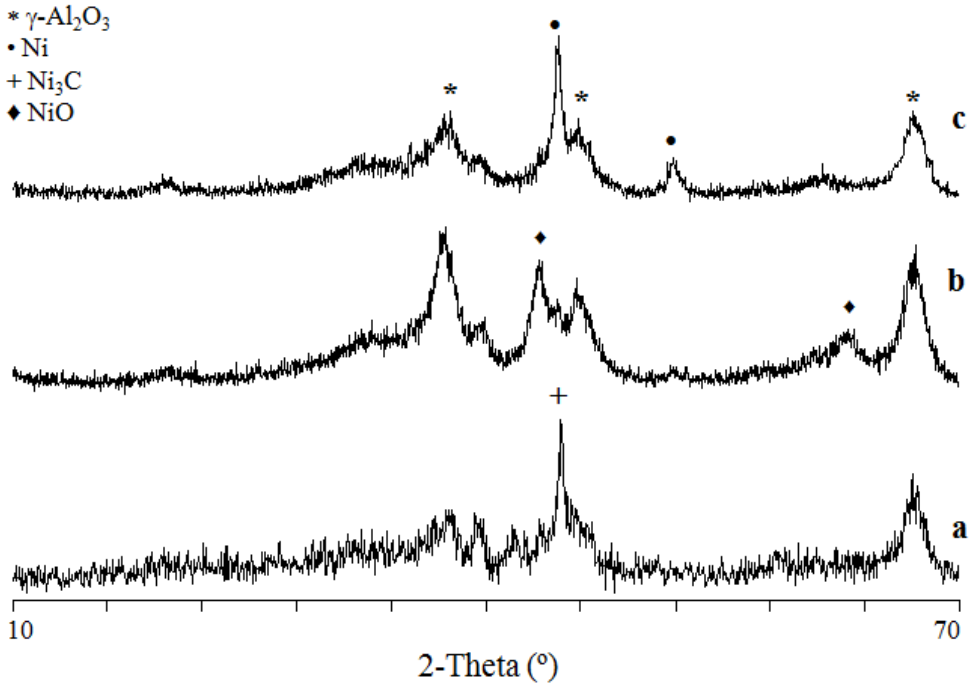

Figure 3.16 XRD patterns of the Ni923 catalyst in the regeneration process, (a) after reaction, (b) after oxidation and (c) after reduction

FTIR of adsorbed CO at RT of the fresh Ni723 sample is depicted on Figure 3.17a. Upon increasing CO equilibrium pressure to 0.062 Torr, there are CO adsorption features observed at 2184 cm^{-1}, 2130 cm^{-1}, 2072 cm^{-1}, 2049 cm^{-1}, 1955 cm^{-1}, 1910 cm^{-1} and 1791 cm^{-1}.

The bands at 2184 cm^{-1} and 2130 cm^{-1} are attributed to CO polarized by Ni^{2+} ions. The band at 2184 cm^{-1} is typical physisorbed CO and it disappears easily upon evacuation. The observed band at 2072 cm^{-1} is ascribed to subcarbonyl species, and the band at 2049 cm^{-1} can be related to linear Ni^0-CO species [50] in agreement with Blackmond and Ko [52].

IR bands at 2072 cm^{-1} and 2049 cm^{-1} could be associated to CO interaction with unsaturated surface Ni atoms located on different crystallographic Ni planes (terraces and steps and/or corners, respectively). The bands at 1955 cm^{-1} and 1910 cm^{-1} can be assigned to one CO molecule bridged bounded to Ni atoms. The band at 1791 cm^{-1} is attributed to Ni_3CO and Ni_4CO species (nickel carbonyl species) [51].

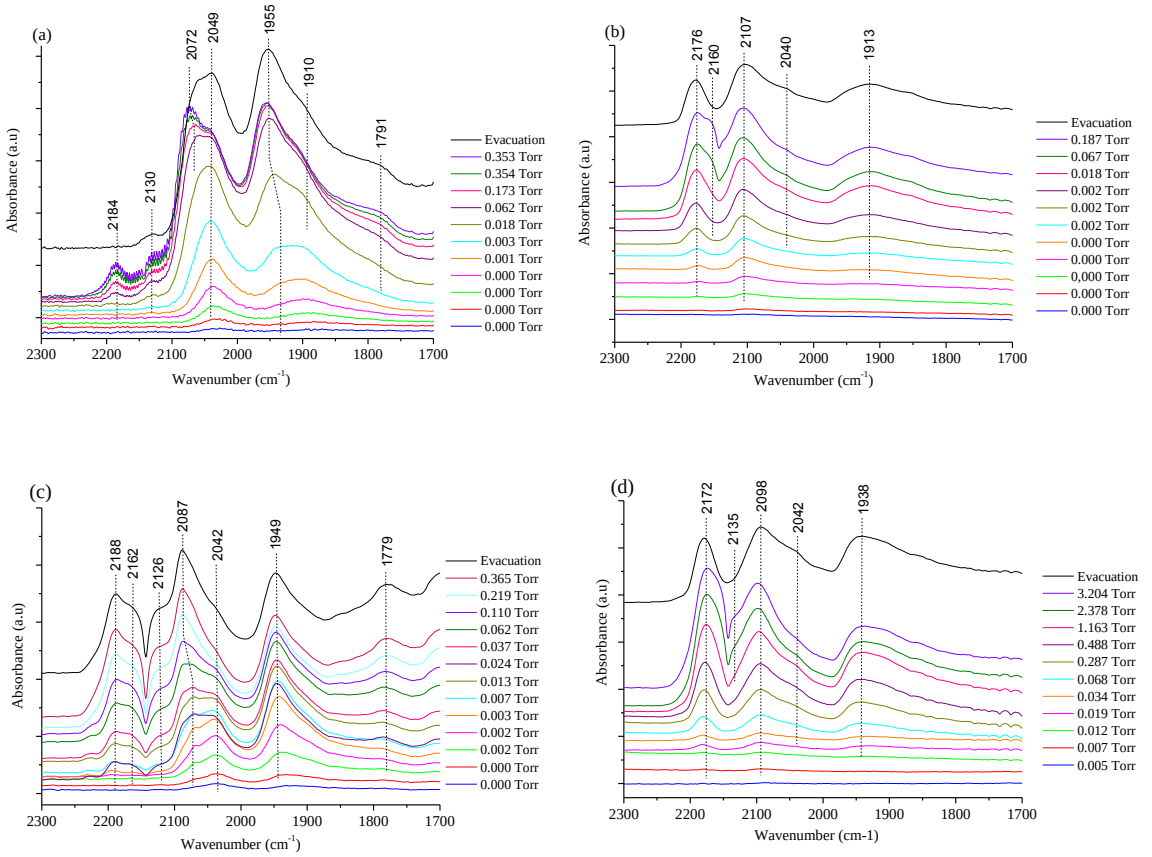

Figure 3.17 Infrared spectra recorded at RT and 100 K on the fresh and used Ni723 sample upon successive addition of CO increments and evacuation: (a) fresh RT, (b) fresh 100 K, (c) used RT, (d) used 100 K

There is no clear change in the IR spectra with a further increase in the equilibrium CO pressure up to 0.352 Torr as shows Figure 3.17. After evacuation in UHV, the band at 2184 cm^{-1} is more easily removed during evacuation process indicating that is weakly adsorbed CO. In addition, after pumping down to UHV, the CO band at 2072 cm^{-1} the atop CO stretching peak shifts to smaller wavelengths, and meanwhile it is observed the bands at 2049 cm^{-1} and 1955 cm^{-1} which can be ascribed to linear Ni^0-CO and CO bridged species, respectively.

The FTIR spectra at 100 K of the fresh Ni723 catalyst (Figure 3.17b) clearly reveal CO on Ni^{+2} and Ni^{+} adsorption species together with linear Ni^0-CO and CO bridged species. The spectra obtained at 100 K of the fresh Ni723 sample reveal bands at 2200 cm^{-1}–2100 cm^{-1} which indicates that in the starting condition the fresh Ni723 catalyst is

partially oxidized. This is in agreement with the degree of reduction obtained by our XANES results of the fresh material (Figure 3.1). Upon evacuation theses species are observed as shown in the black curve in Figure 3.17b.

The adsorption of CO at RT and 100 K of the used Ni723 catalyst are expressed by the FTIR spectra in the Figure 3.17c and d, respectively. Based on Figure 3.17c and d, the nature of the Ni catalyst sites were not altered after the catalytic transformation of glycerol. Essentially the linear, bridge and nickel carbonyl species are observed in the catalyst surface after reaction.

3.7 Conclusions

The catalytic conversion of glycerol in gas phase and atmospheric pressure has been investigated over Ni/γ-Al_2O_3 catalysts. The catalysts were prepared with nickel nitrate and pre-treated with hydrogen in the range of 623 K–1073 K. These different reduction temperatures were applied to study their effects on the catalytic performance. The Ni/γ-Al_2O_3 catalysts were characterized before and after catalytic reaction.

The stability, selectivity and activity were modulated by the reduction conditions. Our findings indicated that the Ni particle size combined with the acidity modulated the catalytic performance of the Ni catalyst. The bifunctional metal-acid property of the catalysts regulated the routes of the reactions and the stability of the catalysts. Metallic Ni species are evolved in the hydrogenolysis route. NiO sites are related with dehydration of glycerol.

Several routes of glycerol transformation such as dehydration, dehydrogenation and hydrogenolysis were observed giving different products (see Scheme 3.1). Deep hydrogenolysis route to produce CH_4 prevails in the first period of time of reaction. As the reaction time progresses, dehydration-dehydrogenation products start to appear. The main products obtained were hydroxyacetone, pyruvaldehyde, pyruvic acid, lactic acid, lactide, acetaldehyde and methane. The number of exposed Ni atoms and the degree of reduction of the NiO species affected the hydrogenolysis reaction of glycerol to CH_4 affecting the catalytic stability.

The catalyst was deactivated by coke formation. Raman analysis revealed two types of carbonaceous deposits over the used samples: on the Ni species and on the support.

FTIR of adsorbed CO on the fresh and used Ni723 catalyst revealed that the nature of the catalytic sites is not altered by the carbon deposition.

The oxidation of metallic Ni in the course of reaction was also considered a source of deactivation. Ni oxide species promote dehydration routes. Dehydration, which takes place on the acid sites, is the manly route related to the generation of carbon deposition and to the observed catalyst deactivation. Another source of deactivation was due to carbiding of Ni to form Ni_3C.

Total regeneration of used Ni catalyst after the glycerol transformation was achieved by oxidation-reduction steps at 723 K without changing the structure. XRD and HRTEM reveals that the oxidation step produces the transformation of Ni_3C into NiO, and the reduction step transform the NiO phase to metallic Ni which is crucial to activate the Ni sites.

3.8 References

[1] I. Chen, D.W. Shiue, Ind. Eng. Chem. Res. 27 (1988) 429-434.
[2] I. Chen, S. Lin, D. Shiue, Ind. Eng. Chem. Res. 27 (1988) 926-929.
[3] J. R.A. Sietsma, H. Friedrich, A. Broersma, M. Versluijs-Helder, A. Jos van Dillen, P. E. de Jongh, K.P.d. Jong, J. Catal. 260 (2008) 227–235.
[4] G. Li, L. Hu, J.M. Hill, Appl. Catal. A. 301 (2006) 16-24.
[5] J.T. Richardson, M. Lei, B. Turk, K. Forster, M.V. Twigg, Appl. Catal. A. 110 (1994) 217-237.
[6] S. Velu, S.K. Gangwal, Solid State Ionics. 177 (2006) 803 – 811.
[7] W. Brockner, C. Ehrhardt, M. Gjikaj, Thermochim. Acta. 456 (2007) 64–68.
[8] S. Yuvaraj, L.F. Yuan, C. T.Huei, Y. C.Tih, J. Phys. Chem. B. 107 (2003) 1044-1047.
[9] K. Sing, D. Everet, R. Haul, L. Moscou, R. Pierotti, J. Rouquerol, T. Siemieniewska, Pure Appl. Chem. 57 (1985) 603-619.
[10] J. Lif, I. Odenbrand, M. Skoglundh, Appl. Catal. A. 317 (2007) 62-69.
[11] C.H. Bartholomew, R.J. Farrauto, J. Catal. . 45 (1976) 41-53.
[12] W.Suprun, M. Lutecki, T. Haber, H. Papp, J. Mol. Catal. A: Chem. 309 (2009) 71-78.
[13] A. Corma, P. J. Miguel, A.V. Orchilles, J. Catal. 145 (1994) 171-180.
[14] F. Auneau, C. Michel, F. Delbecq, C. Pinel, P. Sautet, Chem. Eur. J. 17 (2011) 14288-14299.
[15] Y. Nakagawa, K. Tomishige, Catal. Sci. Technol. 1 (2011) 179–190.
[16] M. Neuber, S Ernst, H. Geerts, P. J. Grobet, P. A. Jacobs, G. T. Kokotailo, J. Weitkamp, Stud. Surf. Sci. Catal. 34 (1987) 567.
[17] M. J. F. M. Verhaak, A. J. Van Dillen, J.W. Geus, J. Catal. 143 (1993) 187-200.
[18] J. Guo, H. Lou, X. Zheng, Carbon 45 (2007) 1314.
[19] J. R. Anderson, M. Boudart, Catalysis: Science and Technology, Springer-Verlag, Berlin, 1984.

[20] C.H. Bartholomew, J.B. Butt, Catalyst Deactivation, Elsevier Science, Amsterdam, 1991.
[21] D. A. Whan, C. Kemball, Trans. Faraday Soc. 64 (1968) 1102-1112.
[22] Z. Wang, X.-M. Cao, J. Zhu, P.Hu, J. Catal. 311 (2014) 469-480.
[23] A. M. Amin, E. Croiset, W. Epling, Int. J. Hydrogen Energy 36 (2011) 2904-2935.
[24] P. Forzatti, L. Lietti, Catal. Today 52 (1999) 165-181.
[25] C.H. Bartholomew, Appl. Catal. A. 212 (2001) 17-60.
[26] H. Atia, U. Armbruster, A. Martin, J. Catal. 258 (2008) 71-82.
[27] E.S. Vasiliadou, A.A. Lemonidou, Appl. Catal., A. 396 (2011) 177–185.
[28] Y.T. Chua, P.C. Stair, J. Catal. 213 (2003) 39-46.
[29] L. Mendoza, R. Baddour-Hadjean, M. Cassir, J.P. Pereira-Ramos, Appl. Surf. Sci. 225 (2004) 356–361.
[30] F. F. de Sousa, H. S. A de Sousa, A. C. Oliveira, M. C. Junior, A. P. Ayala, E.B. Barros, B. C. Viana, J. M. Filho, A.C. Oliveira, Int. J. Hydrogen Energy. 37 (2012) 3201-3212.
[31] A.C. Ferrari, B. Kleinsorge, G. Adamopoulos, J. Robertson, W.I. Milne, V. Stolojan, L.M. Brown, A. LiBassi, B.K. Tanner, J. Non-Cryst. Solids. 266-269 (2000) 765-768.
[32] A. C. Ferrari, J. Robertson, Phys. Rev. B. 61 (2000) 14095-14107.
[33] F. Loviat, I. Czekaj, J. Wambach, A. Wokaun, Surf. Sci. 603 (2009) 2210-2217.
[34] I. Czekaj, F. Loviat, F. Raimondi, J. Wambach, S. Biollaz, A. Wokaun, Appl. Catal. A 329 (2007) 68-78.
[35] J. Bedia, R. Barrionuevo, J. Rodríguez-Mirasol, T. Cordero, Appl. Catal. B. 103 (2011) 302-310.
[36] D. Li, Y. Zhan, K. Nishida, Y. Oumi, T. Sano, T. Shishido, K. Takehira, Appl. Catal. A. 363 (2009) 169- 179.
[37] M. El Doukkali, A. Iriondo, J. F. Cambra, P.L. Arias, Top. Catal. (2014).
[38] G. Wen, Y. Xu, H. Ma, Z. Xu, Z. Tian, Int. J. Hydrogen Energy. 33 (2008) 6657-6666.
[39] A.I. M. El Doukkalia, P.L. Arias, J. Requies, I. Gandaríasb, L. Jalowiecki-Duhamel, F. Dumeignil, Applied Catalysis B: Environmental 125 (2012) 516– 529.
[40] J.W. Shabaker, D.A. Simonetti, R.D. Cortright, J.A. Dumesic, J. Catal. 231 (2005) 67-76.
[41] Y. Zhang, G. Xiong, S. Sheng, W. Yang, Catal. Today. 63 (2000) 517-522.
[42] T. Zhang, M.D. Amiridis, Appl. Catal. A. 167 (1998) 161-172.
[43] Y. T. Kim, K-D. Jung, E.D. Park, Appl. Catal. A. 393 (2011) 275-287.
[44] E.G.M. Kuijpers, A. K. Breedijk, W. J. J. van der Wal, J.W. Geus, J. Catal. 72 (1981) 210-217.
[45] H.S.A.d. Sousa, A. N. da Silva, A. J. R. Castro, A. Campos, J. M. Filhob, A.C. Oliveira, Int. J. Hydrogen Energy. 37 (2012) 12281-12291.
[46] J.-W. Snoeck, G. F. Froment, M. Fowle, J. Catal. 169 (1997) 240-249.
[47] L. J. E. Hofer, E. M. Cohn, W.C. Peeble, Bureau of Mines, Bruceton, Pennsylvania 1949, pp. 1161-1169.
[48] K. Hadjiivanov, Catal. Rev. -Sci. Eng. 42 (2000) 71-144.
[49] K. Hadjiivanov, G.N. Vayssilov, Adv. Catal. . 47 (2002) 307.
[50] J.W.C. Liberatori, R.U. Ribeiro, D. Zanchet, F.B. Noronha, J.M.C. Bueno, Appl. Catal. A. 327 (2007) 197-204.

[51] M. Mihaylov, O. Lagunov, E. Ivanova, K. Hadjiivanov, Top. Catal. 54 (2011) 308-317.
[52] X. Zhu, Y-p. Zhang, C.-j. Liu, Catal. Lett. 118 (2007) 306-312.

Chapter 4

Influence of copper on nickel-based catalysts in the hydrogenolysis of glycerol

4.1 Introduction

In Chapter 3, we have studied the conversion of glycerol in gas phase over Ni based catalyst [1]. We have proposed a general reaction pathway for glycerol conversion. Several routes of glycerol transformation such as dehydration, dehydrogenation and hydrogenolysis were observed producing mainly hydroxyacetone, pyruvaldehyde, pyruvic acid, methyl lactate, lactide, acetaldehyde and CH_4. Undesired side reaction such as coke formation was observed on Ni/γ-Al_2O_3 catalysts. Coking was the major cause of catalyst deactivation in the glycerol conversion. The use of bimetallic catalysts can be an alternative to control the selectivity and minimize the catalytic deactivation. The introduction of a second metal to the Ni catalyst system may provide significant changes in the catalytic activity and selectivity as compared with the monometallic one [2, 3]. The present chapter is devoted to study the effect of Cu introduction into Ni/γ-Al_2O_3 catalyst in the glycerol conversion.

Catalysts with different Ni/Cu atomic ratios were prepared and tested (See 2.2.2). Physical and chemical properties of the fresh Ni-Cu samples were examined by TGA-MS, TPR, XRD, HRTEM, XANES, FTIR of adsorbed CO, NH_3-TPD, XPS, N_2-physisorption, and H_2-chemisorption.

The catalytic conversion of glycerol was studied. The reaction was carried out at the same conditions as was mentioned in Chapter 3. A general reaction pathway for glycerol conversion over Ni-Cu catalysts is proposed.

Finally, the used catalysts were characterized by N_2-physisorption and XRD. Also, the carbon content in the used samples was studied by Raman analysis and quantified by TPO. The main results from all experimental stages mentioned above are presented and discussed in this chapter.

4.2 Characterization of the fresh catalysts

4.2.1 Thermal decomposition of $Ni(NO_3)_2{\cdot}6H_2O$ and $Cu(NO_3)_2{\cdot}6H_2O$ co- impregnated over γ-Al_2O_3 under H_2 flow

The decomposition temperature of metal nitrate precursors was investigated by TGA-MS over dried samples after impregnation. The DTG profiles in Figure 4.1a shows that the main decomposition of metal nitrate precursors occurred at about 600 K with an

evolution of N_2O (m/z =44) (Figure 4.1b) and NO_2 (m/z =46) (Figure 4.11c) species between 450 K and 600 K, as well as the consumption of H_2 (m/z= 2) (Figure 4.1d).

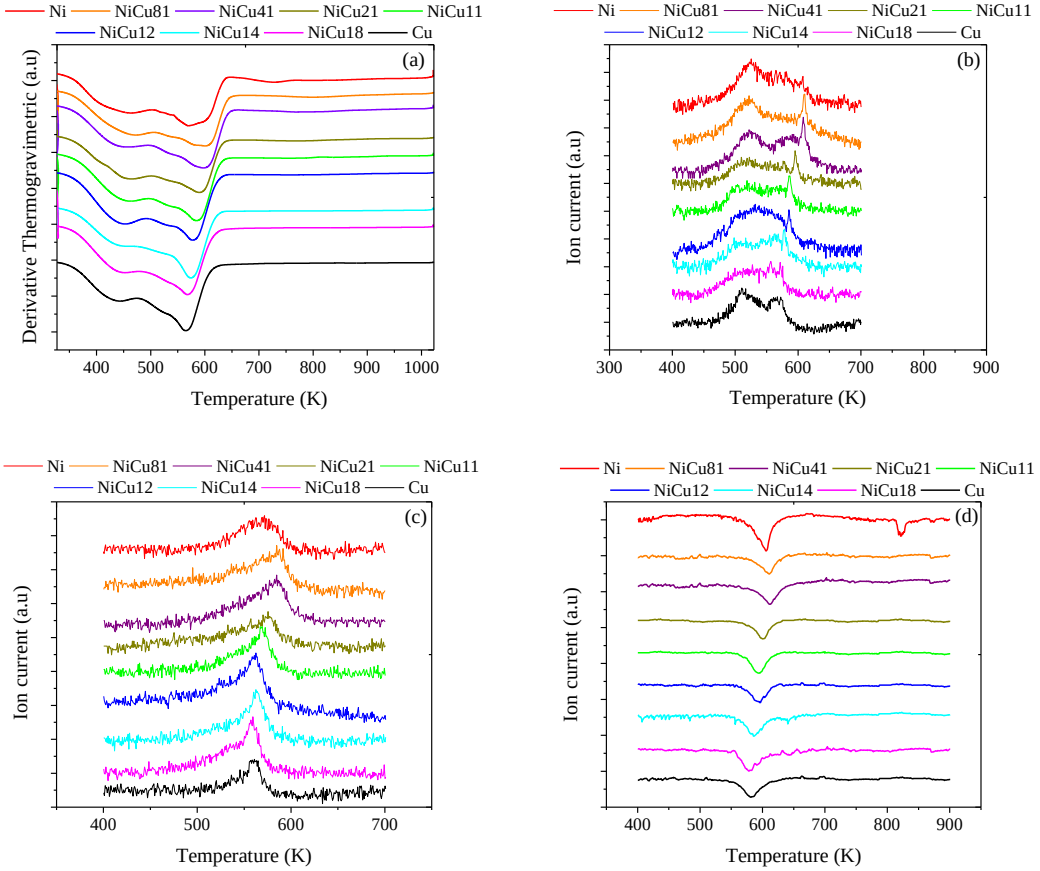

Figure 4.1(a) DTG profiles of the decomposition of metal nitrate precursors, (b) evolution of N_2O (m/z = 44), (c) evolution of NO_2 (m/z = 46), and (d) consumption of H_2 (m/z = 2)

Figure 4.2 shows the XRD patterns of the impregnated copper nitrate precursor over γ-Al_2O_3 under *in situ* reduction with flow of H_2. The *in situ* XRD shows that the total decomposition of the copper nitrate phase occurs below 600 K in agreement with TGA-MS. In Figure 4.2a are evident two main reflections assigned to $Cu_2(OH)_3NO_3$ (Gerhardite, ICDD 14-687) when the dried sample is heated from RT to about 550 K, suggesting that the $Cu(NO_3)_2{\cdot}6H_2O$ is converted to $Cu_2(OH)_3NO_3$. Then, in Figure 4.2b is observed that $Cu_2(OH)_3NO_3$ is decomposed to Cu oxides species around 550 K and the Cu oxides species are reduced to metallic Cu at about 600 K.

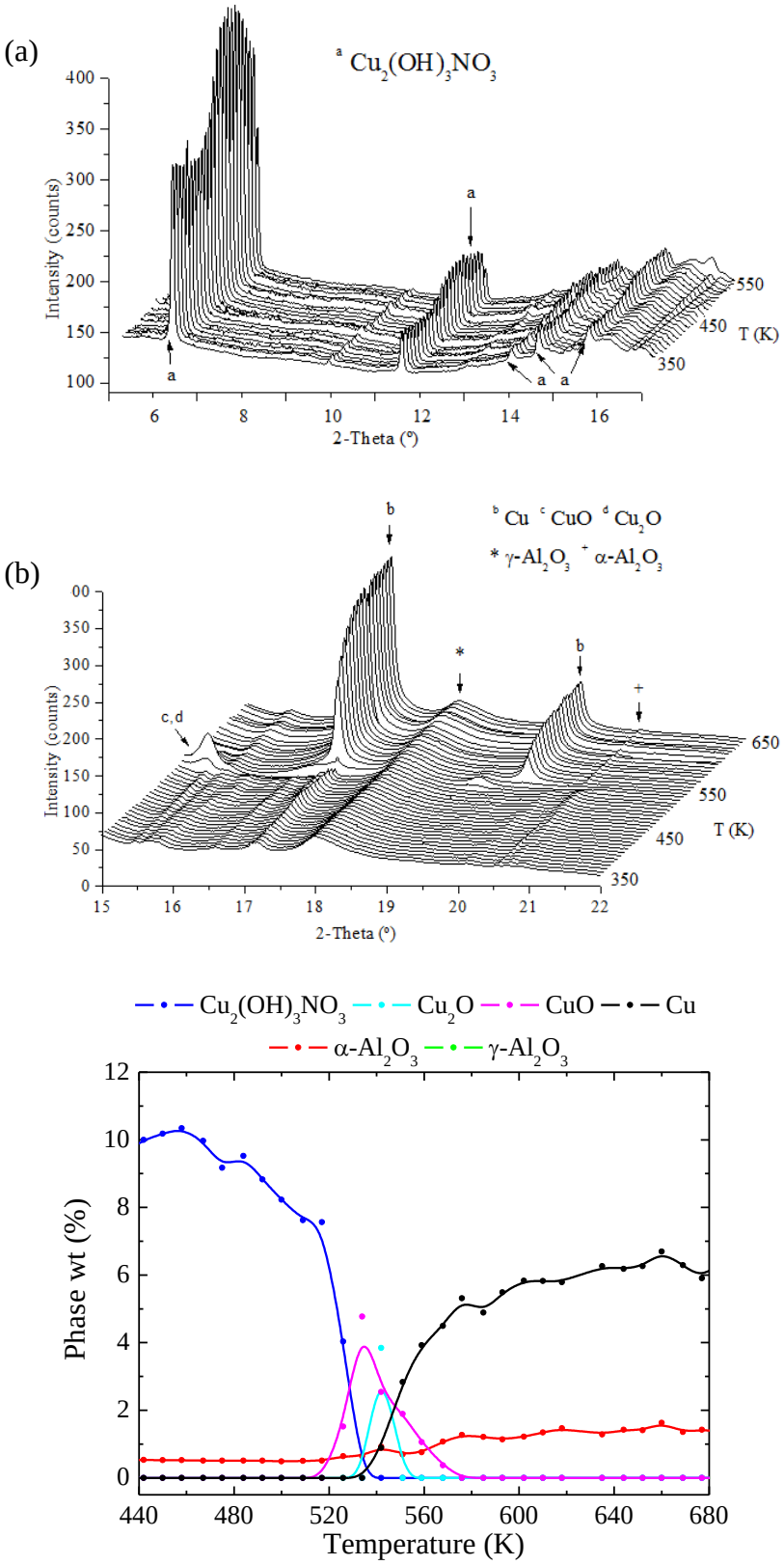

Figure 4.2 Thermal decomposition of copper nitrate precursor impregnated on γ-Al_2O_3: (a, b) *in situ* XRD, and (c) Quantitative phase analysis obtained by Rietveld refinement

The XRD peaks for metallic Cu above 600 K correspond to planes (111) and (200) (ICDD 4-836). The XRD measurements also reveal reflections corresponding to γ-Al_2O_3 (ICDD 79-1558) and α-Al_2O_3 (ICDD 46-1212). Figure 4.2c shows the change in the weight percentage versus reduction temperature for the different phases detected by XRD in the reduction of Cu/γ-Al_2O_3 sample. The results were obtained by Rietveld refinement. The weight percentage of the Gerhardite phase decreases as the reduction temperature increases until its total decomposition around 540 K. Figure 4.2c shows that the Cu_2O and CuO phases appear at around 500 K. Metallic Cu phase starts to appear at around 520 K. The weight percentage of the support is not affected by temperature.

4.2.2 TPR

The TPR profiles of the bimetallic Ni-Cu and monometallic Ni and Cu catalysts are shown in Figure 4.3. The TPR profile of the monometallic Ni sample displays one peak at 576 K (Figure 4.3a) and a broader peak at 747 K (Figure 4.3b). The first peak is due to the reduction of the Ni nitrate precursor to Ni in its oxidizing state [4-7]. The second peak is attributed to the reduction of the NiO species to metallic Ni [8]. For the monometallic Cu sample, the peak between 500 K–550 K (Figure 4.3a) can be attributed to two step reduction of CuO to Cu_2O and Cu_2O to metallic Cu [9]. This is consistent with our *in situ* XRD study (Figure 4.2) of the reduction of the copper nitrate precursor impregnated on γ-Al_2O_3. Table 4.1 shows the dates of maximum reduction temperature from TPR for the Ni-Cu catalysts.

The bimetallic catalysts show two reduction zones: the first one between 500 K and 600 K (Figure 4.3a), and the second one between 600 K and 1000 K (Figure 4.3b). For samples containing a Ni/Cu atomic ratio less than 1 the first peak shifts to lower reduction temperature as the Ni/Cu atomic ratio decreases. For samples containing higher amount of Ni the first peak is quite similar to that of monometallic Ni sample. The second peak between 600 K and 1000 K shifts to lower temperatures when the amount of Cu increases. This indicates that the presence of Cu species enhances the reduction of Ni [10, 11]. In addition, the difference in the position of reduction peaks reported here can be related to the fact that reduction peaks strongly depend on the particle dimension and the interaction strength between metal particle and the support. Previous work dealing with TPR studies on the reduction of Ni-Cu/γ-Al_2O_3 catalysts suggested that the addition of Cu to Ni

precursors can dramatically decrease the reducing temperature of Ni oxides, and might markedly enhance the reducibility of the mixed oxide catalysts [2, 12, 13].The promotion effect gets stronger as the amount of Cu introduced is increased [14-16].

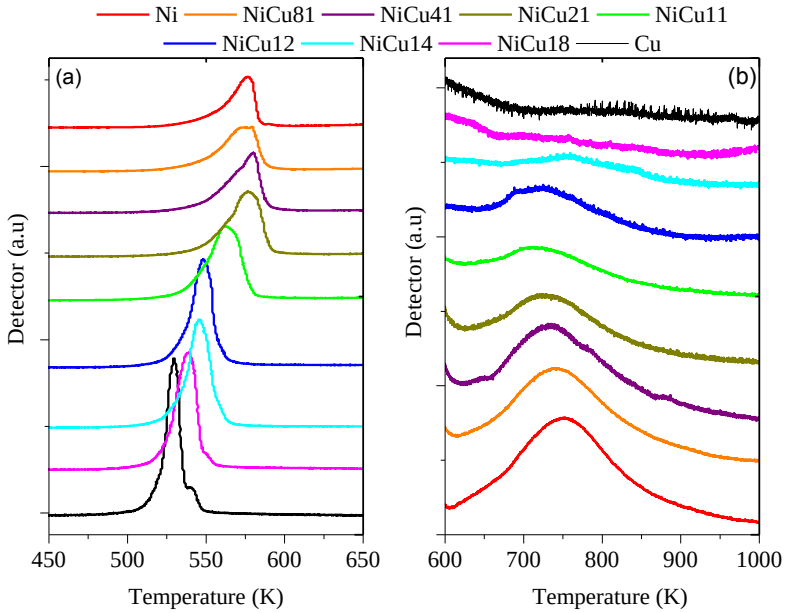

Figure 4.3 TPR patterns of the Ni-Cu/γ-Al_2O_3 catalysts

4.2.3 N_2-physisorption

The N_2-physisorption results of the fresh Ni-Cu samples are depicted in Table 4.1. The surface area of the fresh samples slightly increased with increasing in the Ni/Cu atomic ratio from 90 m^2/g for the monometallic Cu sample to 108 m^2/g for the monometallic Ni sample. The slight increase in the surface area could be related to the formation of more dispersed metal particles in the bimetallic system. Pore volume of the samples is among 0.16 cm^3/g and 0.18 cm^3/g.

4.2.4 NH_3-TPD

The amount of desorbed ammonia measured by volumetric adsorption for all the Ni-Cu samples is shown in Table 4.1. The surface acidity was calculated as total acidity and expressed as µmol of NH_3 desorbed per gram of sample. The γ-Al_2O_3 support presented a total acidity of 182.1 µmol/g_{sample}, which increased to 224.5 µmol/g_{sample} after Ni incorporation and decreased to 175.4 µmol/g_{sample} when Cu was added to γ-Al_2O_3

support. For the bimetallic catalysts, the addition of Cu produces a decrease of the total acidity regarding the monometallic Ni sample in the range from 171.8 μmol/g_{sample} to 113.5 μmol/g_{sample}.

Table 4.1 Results of N_2-physisorption, TPR and TPD-NH_3 of fresh Ni-Cu/γ-Al_2O_3 catalysts

Sample	S_{BET} (m^2/g)	Pore volume (cm^3/g)	Pore size (nm)	TPR		TPD-NH_3 (μmol/g_{sample})
				500 – 600 (K)	600 – 1000 (K)	
γ-Al_2O_3	99	0.17	4.54	-	-	182.1
Ni	108	0.17	4.15	576	747	224.5
NiCu81	108	0.16	4.54	575	739	146.0
NiCu41	104	0.16	4.54	579	729	171.8
NiCu21	105	0.17	4.54	577	723	118.8
NiCu11	111	0.18	4.54	564	716	128.0
NiCu12	104	0.17	4.54	547	715	107.1
NiCu14	104	0.18	4.54	545	-	113.5
NiCu18	101	0.18	4.54	539	-	114.7
Cu	90	0.16	4.54	529	-	175.4

4.2.5 X-ray diffraction

XRD patterns of the fresh Ni-Cu catalysts were recorded in order to identify the crystalline phases formed after the reduction process at 723 K (Figure 4.4a). It is observed crystallographic phases corresponding to metallic Cu for samples with high amount of Cu and γ-Al_2O_3 phase of the support for all the samples. The peaks at around 2θ = 37.5º, 45.7º and 66.7º are assigned to γ-Al_2O_3 phase. The other broad peaks at around 2θ = 43.3º, 50.4º and 74.1º are associated with metal Cu phase [7, 9, 12, 17-19]. Diffraction peaks of Ni species are not observed in all the XRD patterns. The lack of Ni-related reflections in the Ni catalyst diffractogram of Figure 4.4a could be attributed to highly dispersed Ni atoms.

Figure 4.4b shows the XRD patterns of the monometallic Ni and Cu samples, and bimetallic samples (NiCu11, NiCu12, NiCu14 and NiCu18), in the range 2θ = 42°–54º. The XRD measurements (Figure 4.4b) were performed with an internal standard (metallic silicium). It is noticed a slight shift in the diffraction peak of the bimetallic samples to higher 2θ as Ni/Cu atomic ratio increases.

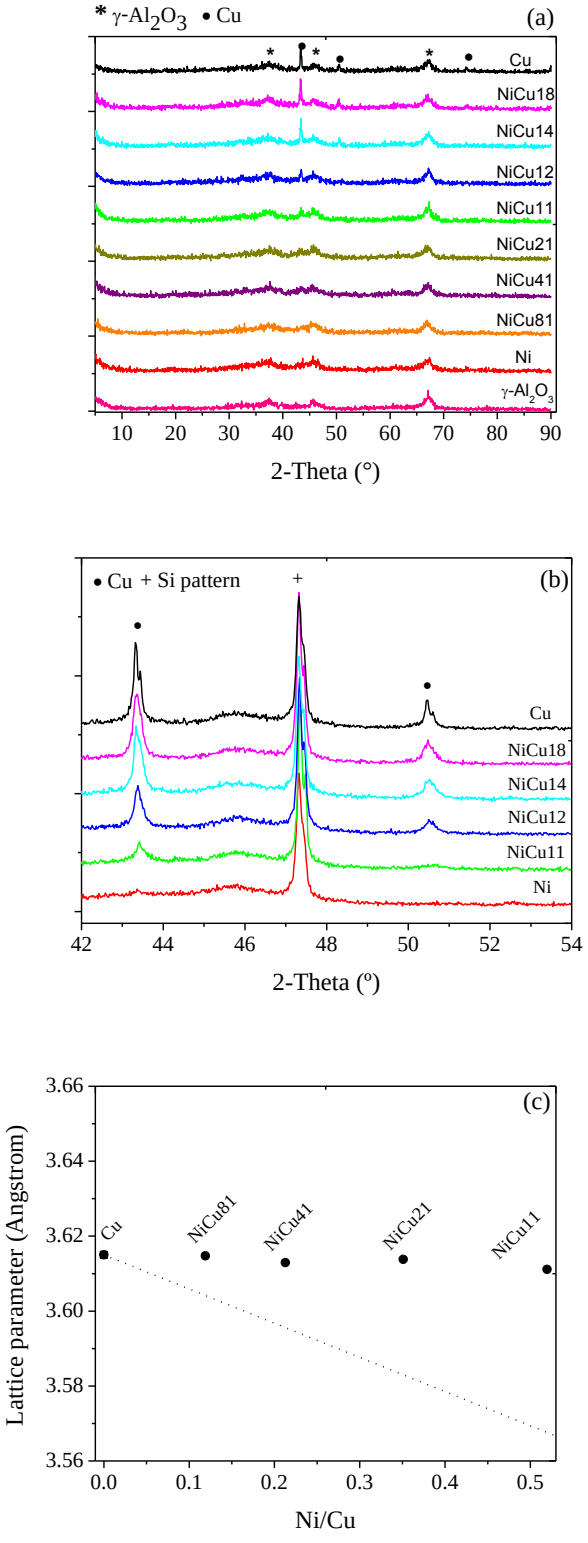

Figure 4.4 X-ray diffraction patterns (a, b) and (c) lattice parameter versus Ni/Cu atomic ratio, of the fresh Ni-Cu samples

Concerning the XRD pattern of the NiCu11 sample, the sharp peak detected at around 2θ = 43.36° is similar to that expected for metal Cu phase (2θ = 43.32°, a = 3.6150 Å) although the lattice parameter (Table 4.2) detected in this case (a = 3.6111 Å) appears slightly smaller. A possibility in this sense is that such change in the lattice parameter is due to formation of a Ni-Cu alloy which is more enriched in Cu. Based on the Vegard´s law [20] the molar fraction of Cu in the NiCu11 sample was calculated to be 0.95, which suggests that a small fraction of Ni is alloying with Cu [21].

The lattice parameters of the samples are plotted in Figure 4.4c with respect to the Ni/Cu atomic ratio. The discrepancy of the calculated lattice parameters from those expected by the Vegard's law (dashed line) reveals that our Ni-Cu samples are not a total intermetallic alloy.

4.2.6 HRTEM

The morphology and the metal particle size of the as-prepared Ni-Cu catalysts were characterized by HRTEM. Figure 4.5a shows a low magnification TEM image of the monometallic Cu catalyst. It shows very small crystallites of the γ-Al_2O_3 support along with well-dispersed small Cu nanoparticles with higher electron contrast. Figure 4.5b shows a high resolution TEM image with several Cu nanoparticles, which measure about 1.5 nm–2 nm in diameter. The lattice-fringe image allows for a proper identification, the planes at 2.1 Å correspond to (111) planes of metallic Cu.

Figure 4.5c corresponds to the monometallic Ni catalyst. It shows Ni particles well distributed over the γ-Al_2O_3 support. A HRTEM image is depicted in Figure 4.5d, where the inset corresponds to the area enclosed in the square. The lattice spacing at 2.0 Å corresponds to the (111) planes of Ni metal. Ni particles are larger than Cu ones, they measure about 4 nm–6 nm in diameter.

Figure 4.5e shows a general view of the NiCu11 catalyst, particles with higher electron contrast correspond to metal particles, which are very well distributed over the γ-Al_2O_3 support. An HRTEM image of one of these particles is shown in Figure 4.5f. The Fourier Transform image of the area selected shows spots at 1.8 Å, which correspond to (200) planes of Ni, Cu, or an alloy. The metal crystallite is oriented along the (100) crystallographic direction.

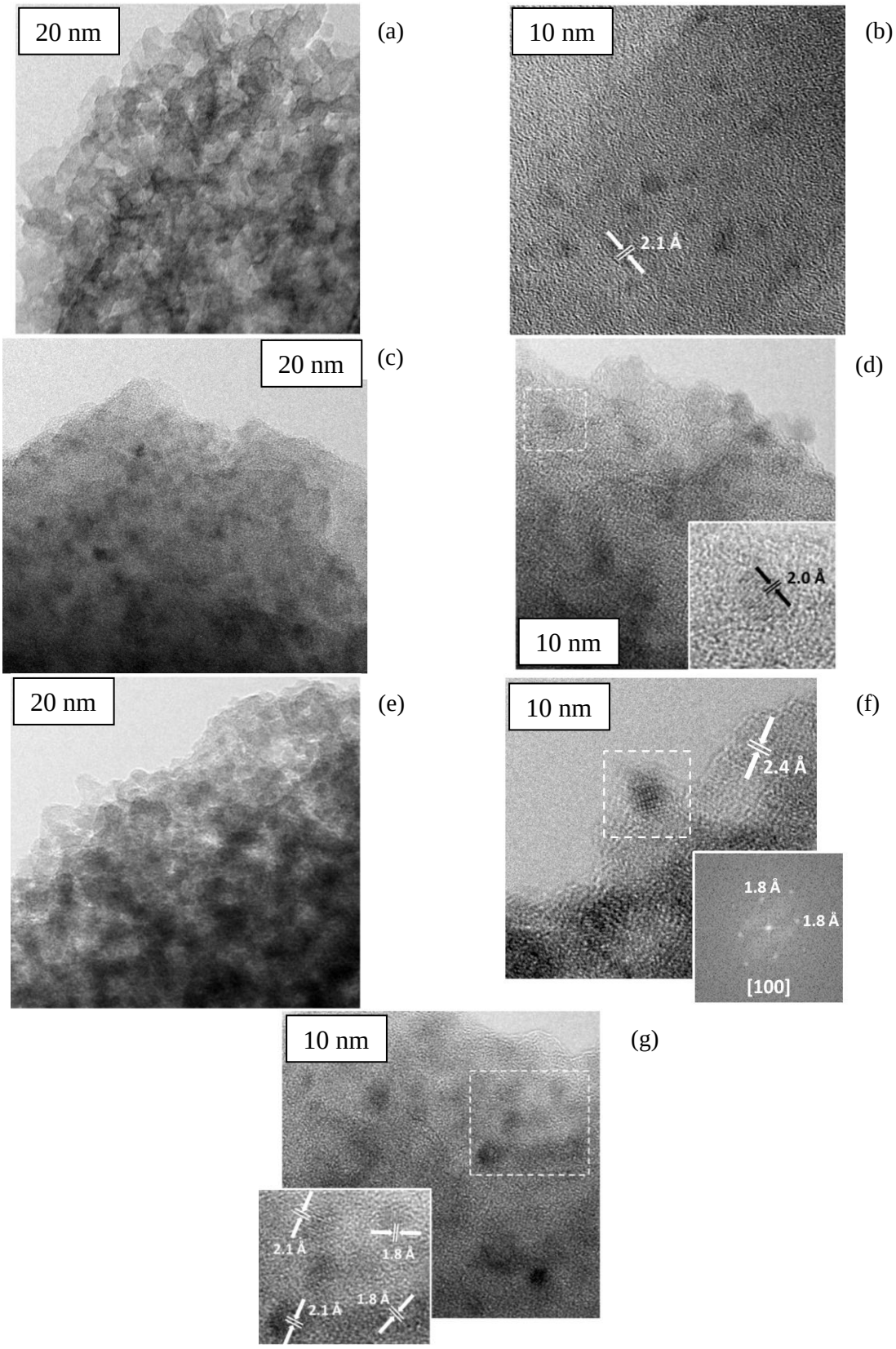

Figure 4.5 HRTEM images of the fresh (a, b) monometallic Cu, (c, d) monometallic Ni, and (e, f, g) bimetallic NiCu11 samples reduced at 723 K

Given the similarities of the lattice parameters of Ni and Cu it is difficult to distinguish between them, so it is not possible to conclude by this technique if Ni-Cu alloy particles are present or if Ni and Cu occur separately. Nevertheless, the particle size distribution of the metal particles is mostly within the range of 3 nm–5 nm in diameter, which lies within those of monometallic Cu and Ni catalysts. Another HRTEM image with various metal particles showing lattice fringes is shown in Figure 4.5g. Lattice fringes at 1.8 Å and 2.1 Å are identified, which correspond to (200) and (111) planes.

4.2.7 H_2-Chemisorption

Table 4.2 shows the number of exposed and dispersion of Ni atoms determined by H_2-chemisorption. The monometallic Ni sample has the highest number of exposed Ni atoms (9.22×10^{19}) which decreases as the Cu loading increases. The exposed Ni atoms change from 4.16×10^{19} for NiCu81 to 6.97×10^{18} for NiCu11 sample. The strongly chemisorbed H_2 is not observed for the monometallic Cu catalyst. For the catalysts NiCu12, NiCu14, and NiCu18 the number of exposed Ni atoms is also indistinguishable. It is noticed that the H_2 chemisorption ability of the bimetallic catalysts decreases upon Cu addition [22]. These results clearly suggest that Cu is the predominant component in the surface of Ni-Cu samples after preparation, in agreement with the literature [23]. The fraction of exposed nicked atoms decreases from 82 % for the monometallic Ni sample to 6.2 % for the NiCu11 sample.

Table 4.2 Results of H_2-chemisorption and lattice parameter (XRD) of the fresh Ni-Cu/γ-Al_2O_3 catalysts

Sample	Number of exposed Ni atoms	Lattice parameter (Å)[b]
γ-Al_2O_3	-	-
Ni	9.22E+19 (82 %)[a]	3.523[c]
NiCu81	4.16E+19 (37 %)[a]	-
NiCu41	3.60E+19 (32 %)[a]	-
NiCu21	2.52E+19 (22 %)[a]	-
NiCu11	6.97E+18 (6.2 %)[a]	3.611
NiCu12	0	3.614
NiCu14	0	3.613
NiCu18	0	3.615
Cu	0	3.615[c]

[a] Values in the brackets are dispersion [b] Lattice parameter determined by XRD analysis
[c] Theoretical values for Ni and Cu

4.2.8 XPS

Results from XPS are shown in Table 4.3. The monometallic Cu catalyst shows the Cu $2p_{3/2}$ main peak at 931.8 eV, and the monometallic Ni sample shows the Ni $2p_{3/2}$ main peak at 854.9 eV. There is not a significant change in these binding energies when a part of Cu is replaced by Ni.

Table 4.3 XPS experimental binding energies, surface atomic percentage and atomic ratio of the Ni-Cu/γ-Al_2O_3 samples reduced at 723 K

Sample	Binding Energy (eV)			Surface atomic (%)		Atomic ratio (XPS)		
	Cu $2p_{3/2}$	Ni $2p_{3/2}$	Al 2p	Cu	Ni	Ni/Al	Cu/Al	Ni/Cu
Ni	-	854.9	73.1	-	8.11	0.088	-	-
NiCu81	932.3	855.1	73.4	3.25	8.90	0.101	0.037	2.74
NiCu41	932.0	855.0	73.7	5.12	6.47	0.073	0.058	1.26
NiCu21	931.4	854.4	72.9	6.47	4.99	0.056	0.073	0.77
NiCu11	931.8	854.6	73.0	5.85	3.00	0.033	0.064	0.51
NiCu12	932.4	855.1	72.8	6.61	1.33	0.015	0.072	0.20
NiCu14	931.7	855.1	73.1	7.05	1.07	0.012	0.077	0.15
NiCu18	931.9	855.6	73.7	15.5	0.72	0.009	0.186	0.05
Cu	931.8	-	73.8	14.3	-	-	0.167	-

The surface atomic percentages of Cu and Ni and the XPS atomic ratios of Ni/Al and Cu/Al for all Ni-Cu catalysts are shown in Table 4.3. The Ni/Al ratio decreases as the amount of Cu increases. In contrast to Ni, the dispersion degree of Cu decreases as its concentration increases which is observed by the increase in the Cu/Al atomic ratio. In addition, the Ni/Cu atomic ratio (Table 4.3) decreases as the Cu content in the sample increases, indicating that the external boundary surfaces of the samples are enriched by Cu. The Cu catalyst surface enrichment is also suggested by the H_2 chemisorption (Table 4.2) results, where the amount of irreversible H_2 chemisorbed decreases as the Ni/Cu atomic ratio decreases. The present results are consistent with previous results on bimetallic Ni-Cu systems, where surface segregation of Cu is predominantly reported. This is justified on the basis of thermodynamics because the lower heat of sublimation (i.e., lower surface free energy) of Cu compared to Ni leads to Cu occupying the surface sites of the bimetallic particles [23].

4.2.9 FTIR of adsorbed CO

Figure 4.6 shows the FTIR spectra of adsorbed CO on Ni-Cu samples at RT after reduction at 723 K. The spectra displayed were obtained after the different CO doses and evacuation in order to eliminate the gas phase species. On the monometallic Ni sample, the observed band at 2132 cm^{-1} is attributed to CO polarized by Ni^{+2} ions [24]. The observed bands at 2056 cm^{-1} and 2037 cm^{-1} can be related to CO linearly bonded on Ni surface [25] in agreement with Blackmond and Ko [26]. The bands at 1952 cm^{-1}–1892 cm^{-1} can be assigned to CO molecules bridged-bounded to Ni atoms. The bands below 1890 cm^{-1} are attributed to Ni_3CO and Ni_4CO species [27].

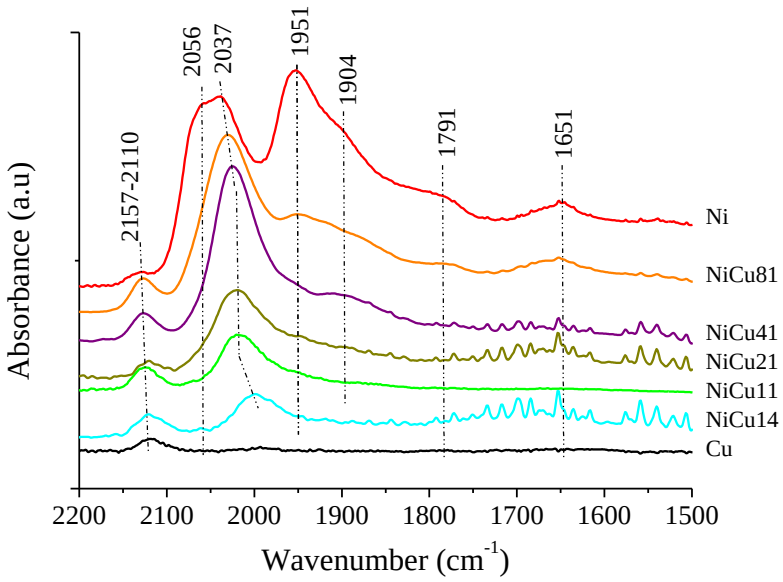

Figure 4.6 Infrared spectra of the reduced Ni-Cu/γ-Al_2O_3 catalysts after evacuation of CO

The addition of Cu to Ni catalysts (Figure 4.6) results in the elimination of CO molecules bridged-bonded to metallic Ni (geometrical effect) as the Ni/Cu atomic ratio decreases. Additionally, the IR peak position of linearly adsorbed CO molecules on Ni red shifted. The shift to lower wavenumber was about 38 cm^{-1}. This may indicate an interaction of Ni with neighboring Cu atoms (electronic effect).

The monometallic Cu catalyst presents a band at 2132 cm^{-1} ascribed to CO adsorbed on Cu^{+} species [23, 28]. With increasing Ni/Cu atomic ratio a slight shift to higher wavenumbers can be observed. This suggests an interaction of Cu^{+} species with Ni.

4.2.10 XANES

Figure 4.7(a) and (b) show XANES spectra for reduction of impregnated samples (monometallic Ni, monometallic Cu and the bimetallic NiCu11). For the monometallic Ni sample (Ni K-edge), Figure 4.7a shows that the white line (WL) is not affected by the increase in reduction temperature between RT and 700 K, indicating that the Ni content is still oxidized below 700 K. Between 700 K and 973 K, the WL decreases and 50 % of the Ni oxide is converted to metallic Ni (Figure 4.7c) at about 800 K. On the bimetallic NiCu11 sample the WL starts to change at around 350 K–400 K (Figure 4.7b). In this case 50 % of Ni oxide is reduced at about 720 K (Figure 4.7d). The decrease in the reduction temperature observed in the bimetallic sample suggests an interaction between Ni and Cu [23] and these results are in good agreement with TPR (Figure 4.3).

The XANES results taken on Cu K-edge for monometallic Cu and NiCu11 samples are shown in Figure 4.7e and f. Below 540 K Cu is completely in +II oxidation state (Tenorite: CuO) in both samples. At this temperature it is observed that 40 % Cu species in the monometallic Cu sample are as Cu(I) oxide (Cuprite: Cu_2O), 20 %–25 % as metallic Cu and around 30 % remaining as CuO (Figure 4.7g). On the other hand in the NiCu11 sample it is observed that CuO completely disappears, at 540 K the Cu species are present in two phases: 35 % as Cu_2O and 65 % as metallic Cu (Figure 4.7h).

In the final reduction condition (973 K) it is observed Cu phases distributed as follows: 20 %–25 % as metallic Cu, 80% as Cu_2O phase and CuO disappeared completely in the monometallic Cu sample (Figure 4.7g). On the other hand, in the bimetallic NiCu11 sample the Cu species present are: 10 % as Cu_2O and 90 % as metallic Cu (Figure 4.7h), suggesting an interaction between Cu and Ni species.

4.3 Hydrogenolysis of glycerol

The reduced Ni-Cu samples were studied in the conversion of glycerol at 573 K under atmospheric pressure. The main products in the condensable phase are: hydroxyacetone, pyruvaldehyde, lactide, lactic acid, acetic acid, pyruvic acid, ethylene glycol (EG), acetaldehyde, and traces of 1,2-PDO and furan derivates. The major products detected in the gas phase are CH_4, acetaldehyde and traces of acetone. The selectivity of hydrogenolysis products such as CH_4 and acetaldehyde and dehydration products (such as hydroxyacetone) are dependent on the Ni/Cu atomic ratio.

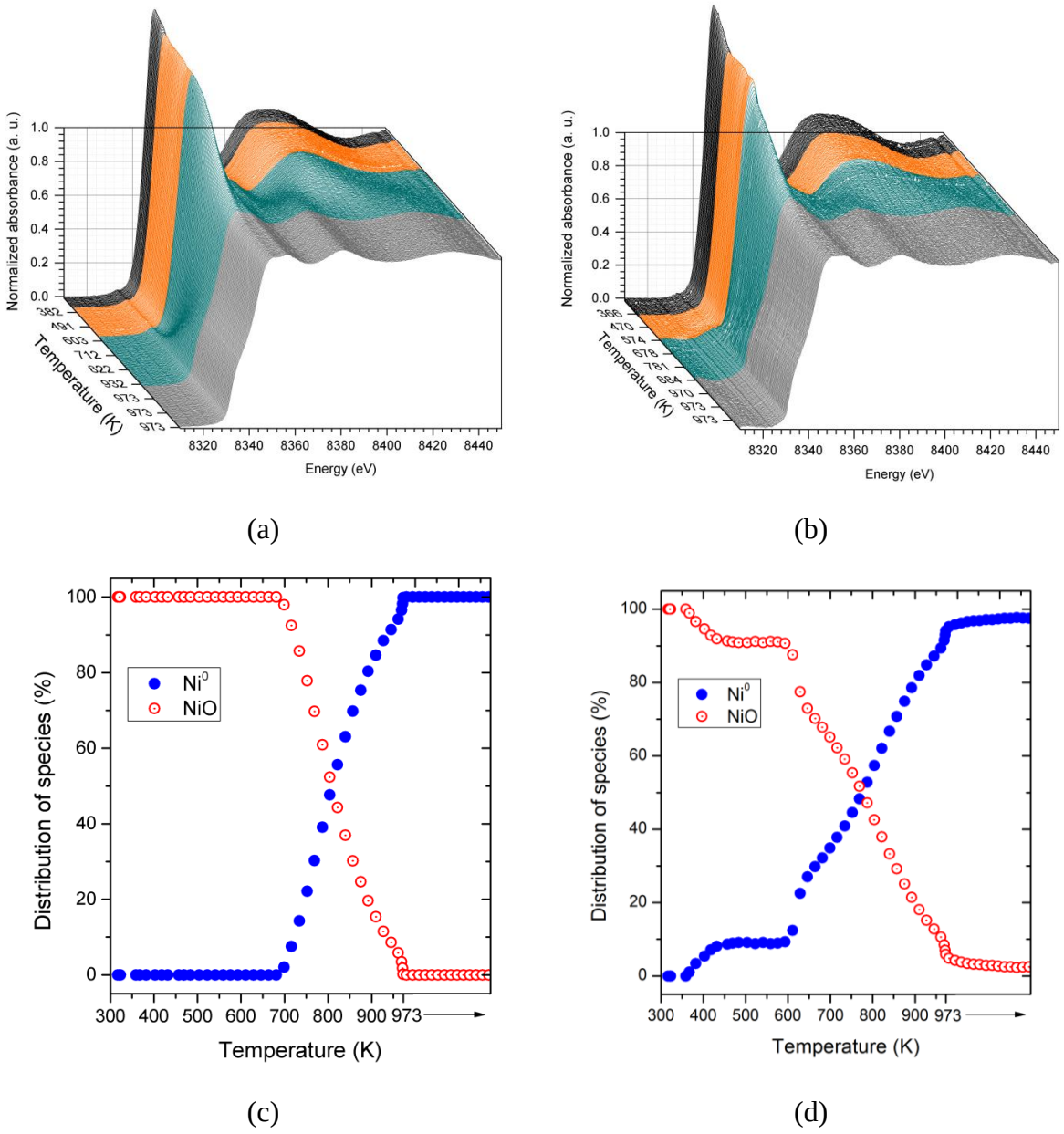

Figure 4.7(a) XANES spectra at the Ni K-edge of the (a) monometallic Ni and (b) NiCu11 samples, amount of reduced versus oxidized Ni species of the (c) monometallic Ni and (d) NiCu11 samples

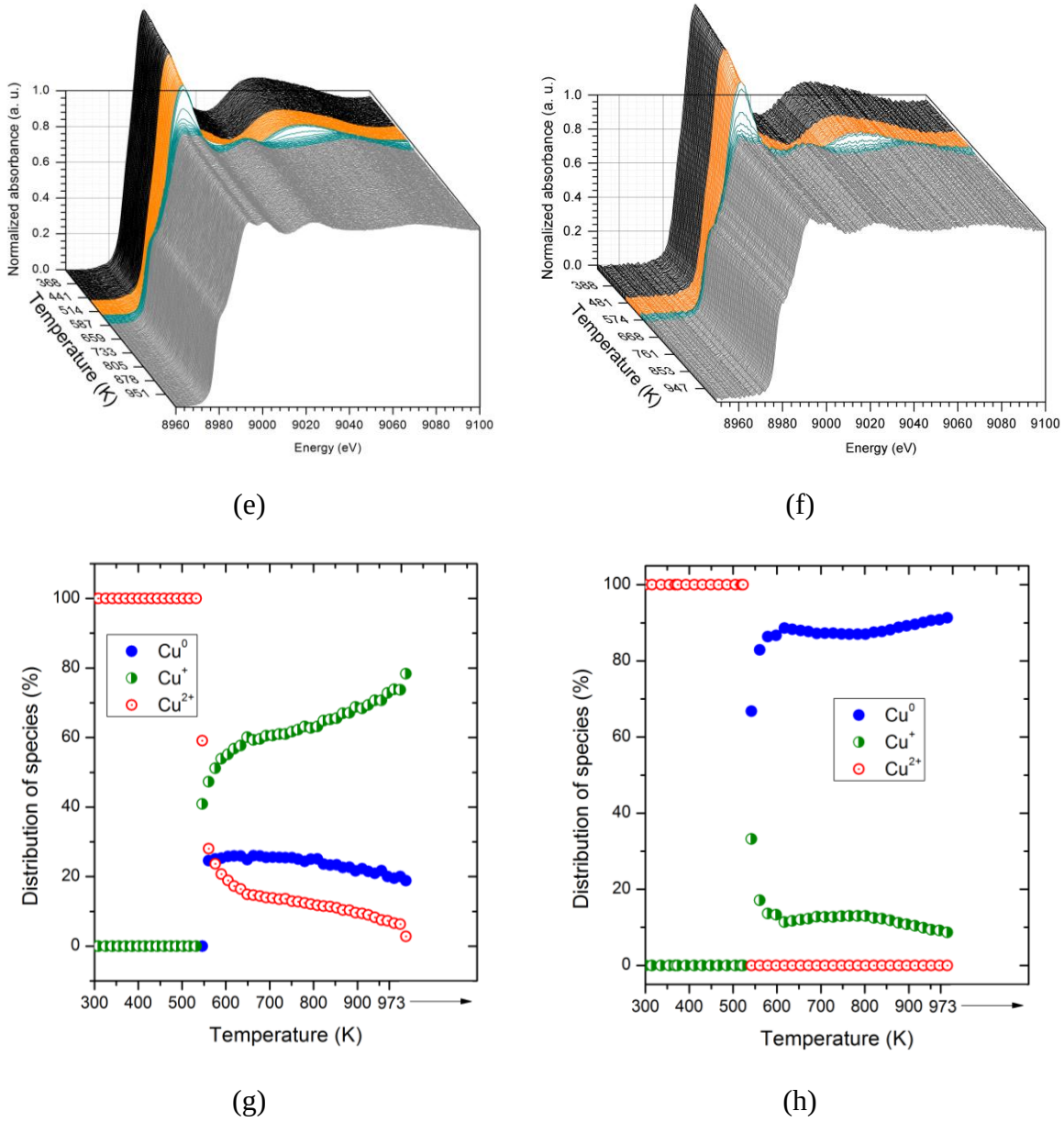

Figure 4.7(b) XANES spectra at the Cu K-edge of the (e) monometallic Cu and (f) NiCu11 samples, amount of reduced versus oxidized Cu species of the (g) monometallic Cu and (h) NiCu11 samples

The glycerol conversion versus time of reaction of the Ni-Cu catalysts is shown in Figure 4.8. For the samples with high amount of Ni (Ni, NiCu81, NiCu41 and NiCu21) the glycerol conversion is at about 100 % over 6 h of reaction indicating high stability of the catalysts. However, the glycerol conversion decreases with time on stream for samples enriched with Cu (NiCu11, NiCu12, NiCu14, NiCu18 and Cu) indicating high deactivation. It is clear that when the Cu content increases a decrease in glycerol

conversion with time on stream is observed. The deactivation is more pronounced for the NiCu14 and NiCu18 catalysts (Table 4.4). The glycerol conversion for the monometallic Cu sample drops from 93 % to about 60 %. It suffers less deactivation than the bimetallic samples with higher content of Cu.

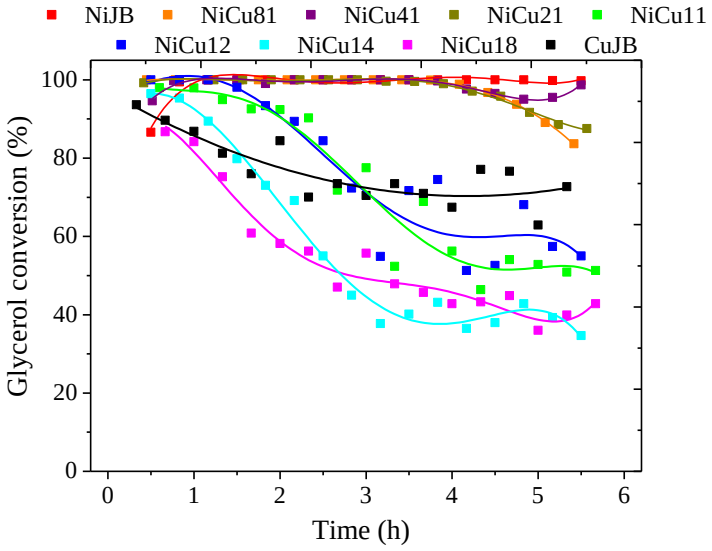

Figure 4.8 Catalytic performances for the Ni-Cu/γ-Al_2O_3 catalysts in function of time of reaction

The selectivity profiles obtained for the Ni-Cu catalysts are shown in Figure 4.9, it can be seen that the selectivity to CH_4 is practically 100 % on Ni, NiCu81, and NiCu41 catalysts. The results presented in chapter 3 revealed that the increase in the total number of exposed Ni atoms and the degree of reduction of the NiO species increases the selectivity to CH_4 affecting the catalytic stability. Further increase in Cu content produces a decrease in the selectivity to CH_4. The opposite behavior is observed on selectivity to dehydration-dehydrogenation products such as hydroxyacetone and pyruvaldehyde which increases with increasing the Cu content. The production of CH_4 was finally total suppressed in the monometallic Cu sample. Thus, the results show that selectivity to CH_4 decreases progressively when the Ni/Cu atomic ratio decreases.

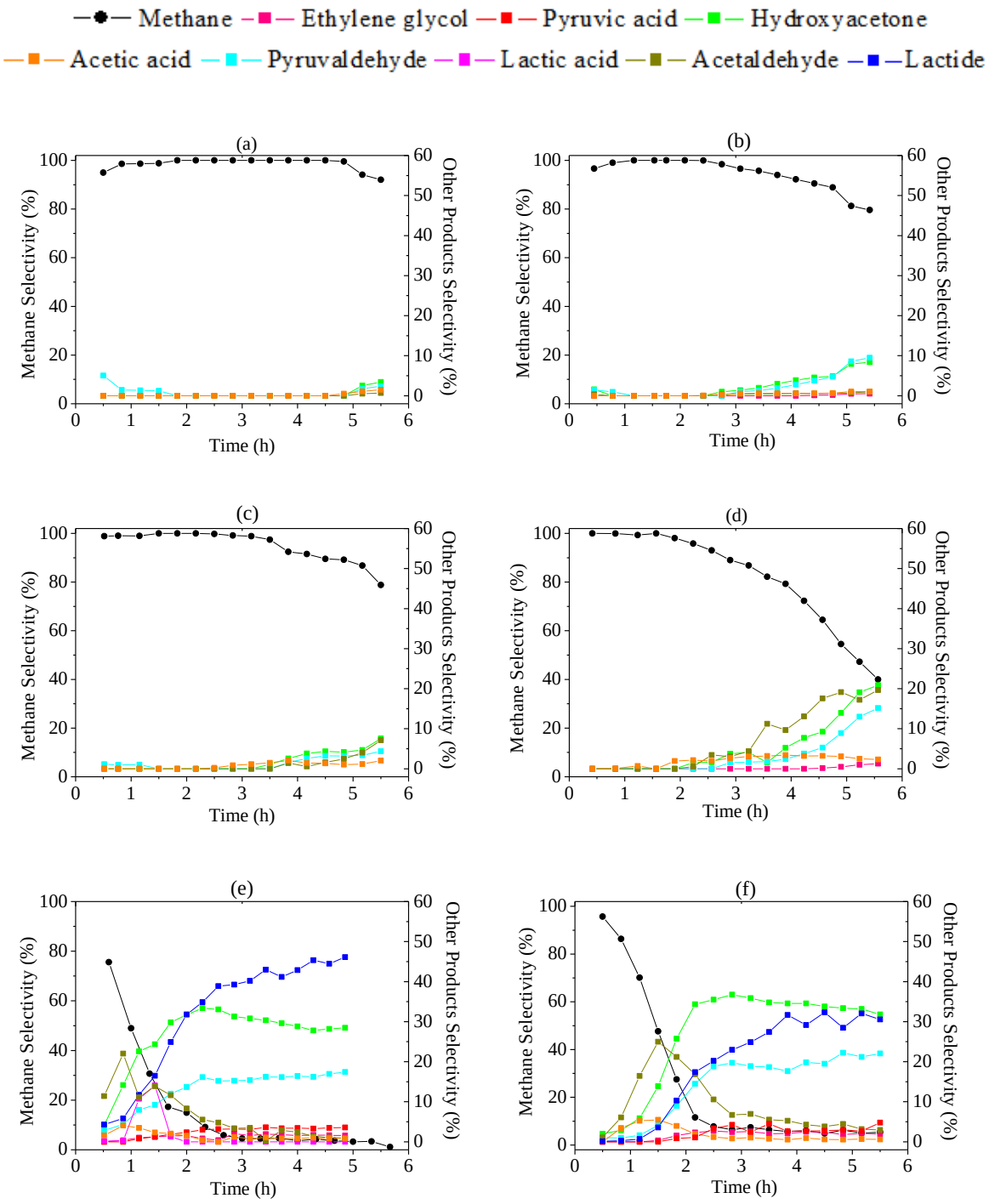

Figure 4.9 Time-on stream product selectivity in glycerol conversion over (a) Ni, (b) NiCu81, (c) NiCu41, (d) NiCu21, (e) NiCu11, (f) NiCu12, (g) NiCu14, (h) NiCu18 and (i) Cu

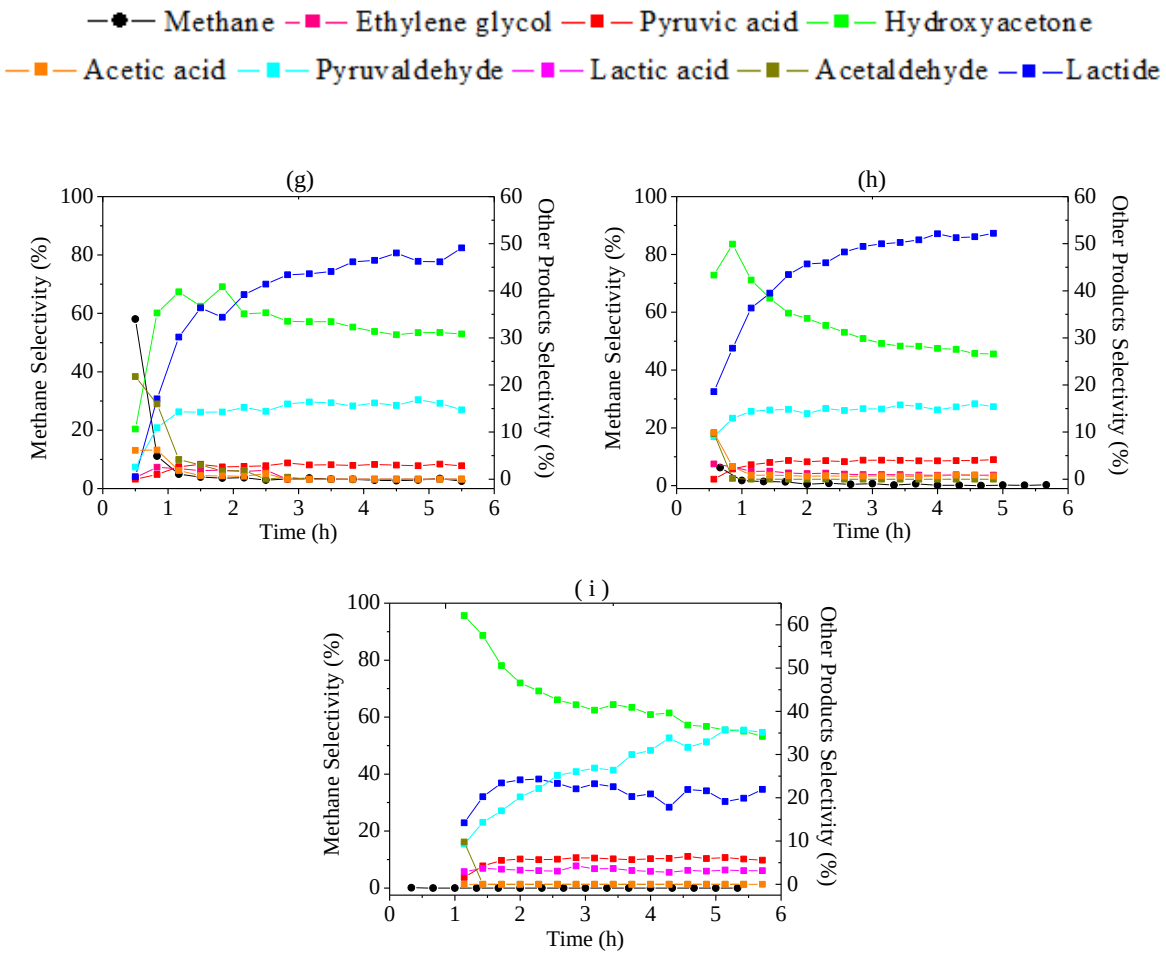

Figure 4.9 (continuation) Time-on stream product selectivity in glycerol conversion over (a) Ni, (b) NiCu81, (c) NiCu41, (d) NiCu21, (e) NiCu11, (f) NiCu12, (g) NiCu14, (h) NiCu18 and (i) Cu.

The effect of addition of Cu into Ni/γ-Al_2O_3 catalysts can be observed in Table 4.4. The selectivity to hydroxyacetone is close to 30 % for NiCu11, NiCu12, NiCu14, and NiCu18 catalysts while on Cu is about 40 % suggesting that the addition of high amount of Cu on Ni favors the dehydration of glycerol to hydroxyacetone. Similar behavior is observed to formation of pyruvaldehyde. The production of lactide preferably occurs on NiCu11, NiCu12, NiCu14, and NiCu18 catalysts and it occurs in less extension on Cu/γ-Al_2O_3.

It can be remarked that the incorporation of Cu into Ni decreases the C-C bond linkage markedly. This indicates that the metal components clearly are not isolated from each other on the support. The activity results data provide also strong evidence of

interaction between Cu and Ni. This interaction is reinforced by our characterization techniques.

4.4 Reaction pathway

Table 4.4 shows that the monometallic Ni sample promotes total deep hydrogenolysis of glycerol to CH_4. The deep hydrogenolysis route is progressively suppressed when the Ni/Cu atomic ratio decreases. EG was detected on NiCu11 and NiCu12 catalysts while acetaldehyde was detected on NiCu81, NiCu41, NiCu21, NiCu11, and NiCu12 samples. Acetaldehyde afterwards suffers oxidation to produce acetic acid. Dehydration and dehydrogenation products such as hydroxyacetone, pyruvaldehyde, lactide and pyruvic acid start to be produced when the Cu content increases. In the monometallic Cu sample the hydrogenolysis products such as CH_4, EG, acetaldehyde and acetic acid are totally suppressed.

Hydroxyacetone, pyruvaldehyde and lactic acid were used as reactants under the same operation conditions performed for the catalytic conversion of glycerol over the monometallic Cu catalyst in order to investigate the role of the Cu in the reaction pathway. The main products obtained when hydroxyacetone is employed as reactant (column 5, Table 4.5) are lactide, pyruvaldehyde and lactic acid. However, the conversion of hydroxyacetone was less than 1.0 % indicating poor catalytic activity of Cu. The strong deactivation observed can be attributed to catalytic cyclisation of hydroxyacetone. Indeed, in this case, the monometallic Cu catalyst suffered strong deactivation at only 1 h of reaction. This fact suggests that the dehydration of glycerol may strongly contribute with the carbon deposition on the catalyst surface [29]. From our results in chapter 3, the conversion of hydroxyacetone with the Ni723 sample was about 16 % and the major product was lactic acid with selectivity of 61 %. Differently of monometallic Cu sample, selectivity of 14 % to CH_4 was observed on Ni723 sample during hydroxyacetone reaction indicating the C-C bond breaking on Ni.

During catalytic conversion of pyruvaldehyde on monometallic Cu sample; hydroxyacetone, lactic acid, lactide, pyruvic acid and acetic acid are the major products with selectivity of 28.9 %, 17.7 %, 28.9 %, 17.8 % and 6.41 %, respectively (column 6, Table 4.5). These results suggest that hydroxyacetone may be formed from the hydrogenation of pyruvaldehyde.

Table 4.4 Product selectivity of the main products from the catalytic conversion of glycerol over Ni-Cu catalysts at 4 h of reaction

Column 1	Column 2	Column 3	Column 4	Column 5	Column 6	Column 7	Column 8	Column 9	Column 10
Catalyst	**Ni**	**NiCu81**	**NiCu41**	**NiCu21**	**NiCu11**	**NiCu12**	**NiCu14**	**NiCu18**	**Cu**
Conversion (%)	100	98.8	99.6	99.0	56.3	74.5	43.1	42.8	67.4
Selectivity (%)									
Methane	100	92.2	92.4	79.3	3.69	5.65	3.12	0.15	-
Hydroxyacetone	-	3.88	2.56	5.25	30.3	34.5	32.3	28.5	39.6
Pyruvaldehyde	-	2.77	1.55	2.38	16.2	17.6	15.5	15.9	33.8
Acetic acid	-	0.53	2.06	3.41	1.07	0.55	-	0.66	-
Pyruvic acid	-	-	-	-	3.59	2.62	2.90	4.02	5.98
Lactic acid	-	-	-	-	-	-	-	-	2.77
Lactide	-	-	-	-	42.9	31.6	46.1	50.7	17.8
Ethylene glycol	-	-	-	-	1.89	2.06	-	-	-
Acetaldehyde	-	0.61	1.41	9.67	0.24	5.24	-	-	-
Mass balance [a] (%)	74	90	85	86	100	96	95	100	98

[a] TOC, HPLC and GC analysis

Table 4.5 Product selectivity of the main products from the catalytic conversion of glycerol over monometallic Cu sample at 4 h of reaction

Column 1	Column 2	Column 3	Column 4	Column 5	Column 6	Column 7
Reactant	**Glycerol**	**Glycerol**	**Glycerol**	**Hydroxyacetone***	**Pyruvaldehyde**	**Lactic acid**
Molar ratio H_2/reactant	10	0 [a]	10 [b]	10	10	10
Conversion (%)	67.4	47.7	60.8	0.95	38.3	97.9
Selectivity (%)						
Acetic acid	-	-	-	-	6.41	-
Hydroxyacetone	39.6	23.9	41.7	-	28.9	-
Lactic acid	2.77	-	5.11	9.45	17.8	-
Lactide	17.8	27.7	20.6	57.9	28.9	7.17
Pyruvaldehyde	33.8	41.8	27.8	32.6	-	4.07
Pyruvic acid	5.98	6.60	4.78	-	17.9	80.7
Acetaldehyde	-	-	-	-	-	8.06
Mass balance [c] (%)	98	84	94	100	100	95

[a] Argon atmosphere, [b] CuO catalyst, [c] TOC, HPLC and CG analysis, *2 h of reaction

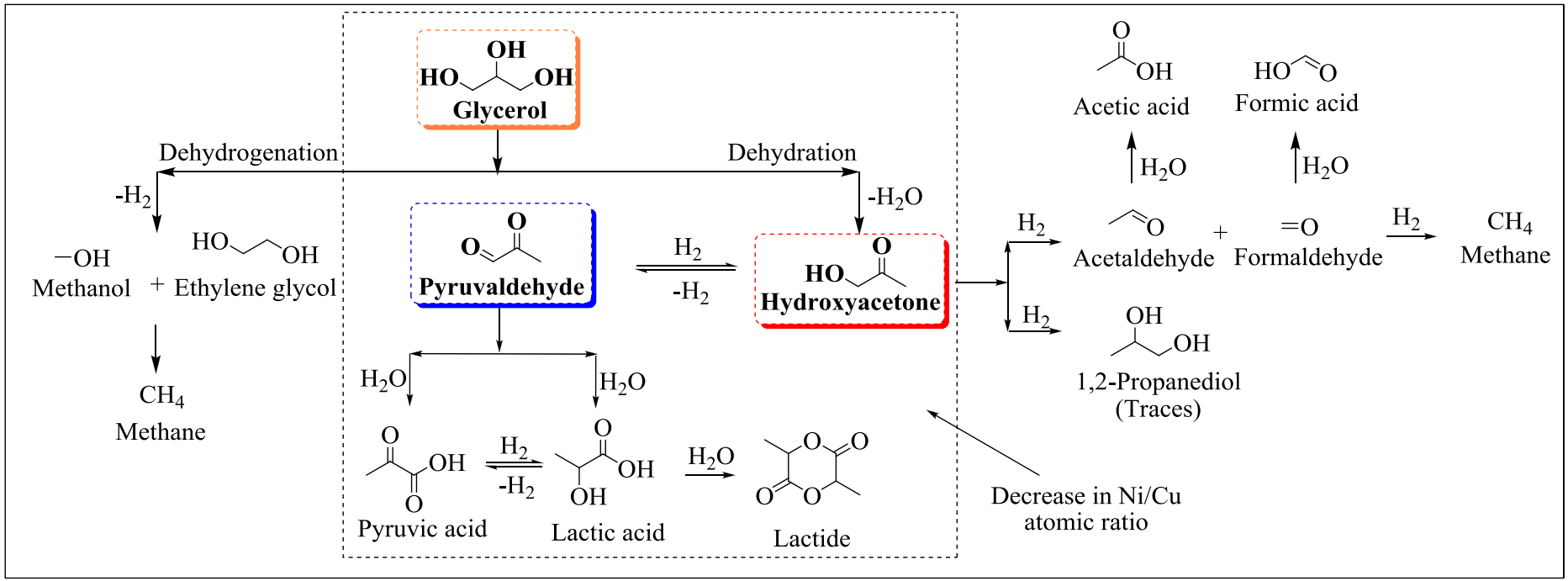

Scheme 4.1 General reaction pathway proposed for glycerol conversion over Ni-Cu/γ-Al_2O_3 catalysts

When lactic acid is employed as reactant (column 7, Table 4.5), the main products obtained are lactide, pyruvaldehyde, pyruvic acid and acetaldehyde. The major product is pyruvic acid with a selectivity of 80.7 %.

Table 4.5 also shows that when the monometallic Cu catalyst is previously calcined at 723 K instead of reduced; the glycerol conversion (60.8 %, column 4) is slight lower than that observed under H_2 flow (67.4 %, column 2). This suggests that dehydration and dehydrogenation of glycerol can also occur on oxidized Cu species.

In addition, the conversion of glycerol using the monometallic Cu catalyst under Ar flow reveals a glycerol conversion of 47.7 % (column 3, Table 4.5) which is lower than that observed under H_2 flow.

The results above are used to propose a general reaction pathway for glycerol conversion over Ni-Cu/γ-Al_2O_3 catalysts (Scheme 4.1). As the Cu content in the catalysts increases the reaction pathway is conducted to the products inside to the dashed line of the rectangle. Glycerol is consumed either by hydrogenolysis to CH_4 or dehydration to form hydroxyacetone which is dehydrogenated to form pyruvaldehyde. The dehydration route becomes more pronounced when Cu content in the samples increases. Pyruvaldehyde can be hydrogenated to form hydroxyacetone. Acetaldehyde and CH_4 can be obtained from the catalytic C-C bond cleavage of hydroxyacetone [30]. In addition, pyruvaldehyde can be converted to lactic acid either via a Cannizzaro reaction [31] or via oxidation to pyruvic acid which can further hydrogenate forming lactic acid in a reverse reaction. Finally the lactic acid undergoes dimerization to form lactide.

4.5 Characterization of the used catalysts

Catalytic deactivation was observed in the glycerol conversion as shown in Figure 4.8. The N_2-physisorption (Table 4.6) reveals a decrease in the surface area, pore volume and pore size with respect to the fresh samples (Table 4.1) especially for the bimetallic samples with higher content in Cu. This may suggests some carbon deposition during the reaction. XRD results of the used Ni-Cu samples (Figure 4.10) did not reveal changes in the structure of the materials.

Raman spectra (Figure 4.11) in the range of 1100 cm^{-1} to 2000 cm^{-1} display two main bands D and G [21] ascribed to carbon species. According to previous works [32-34],

the D-band is associated to non-deactivating carbon (amorphous carbon) and the G-band is related to deactivating carbon (graphitic carbon).

Table 4.6 N_2-physisorption and TPO results of the used Ni-Cu/γ-Al_2O_3 catalysts

Sample	S_{BET} (m^2/g)	Pore volume (cm^3/g)	Pore size (nm)	TPO (wt% C)
γ-Al_2O_3	-	-	-	-
Ni	105	0.16	4.15	1.82
NiCu81	89	0.13	4.15	0.16
NiCu41	95	0.14	4.15	1.18
NiCu21	94	0.14	4.15	1.55
NiCu11	82	0.12	4.15	3.76
NiCu12	80	0.14	4.15	7.16
NiCu14	95	0.15	4.15	2.72
NiCu18	94	0.15	4.15	4.26
Cu	98	0.17	4.15	0.34

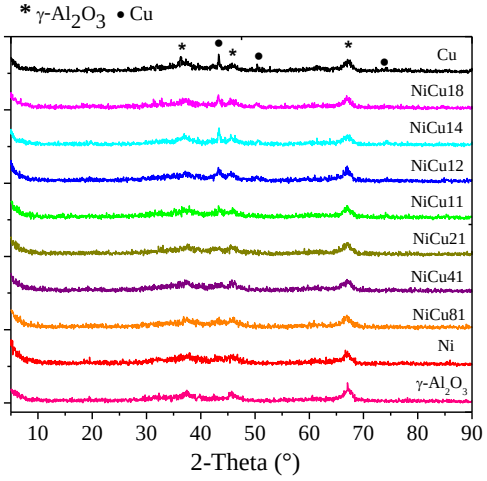

Figure 4.10 X-ray diffraction patterns of the used Ni-Cu/γ-Al_2O_3 catalysts

The carbon deposition on used Ni-Cu samples was determined by TPO as shown in Table 4.6. The monometallic Ni sample shows 1.82 wt% of carbon deposited and the monometallic Cu sample presents 0.34 wt%. For the bimetallic samples, it can be seen an increase in carbon deposition in the samples with higher Cu content such as 7.16 wt% for NiCu12, 2.72 wt% for NiCu14, and 4.26 wt% for NiCu18 samples. This indicates the direct involvement of Cu species in the dehydration of glycerol. The dehydration route markedly contributes to the carbon deposition on the catalysts as noted by previous works

leading to the observed deactivation [30]. The formation of carbon deposits during dehydration reaction of glycerol may result from consecutive reactions of glycerol, like oligomerization on acidic catalyst surface sites and/or side reactions between dehydrated products like hydroxyacetone [29]. In fact, our results (Table 4.6) show that the glycerol dehydration route dominates over the hydrogenolysis when the Cu content increases and higher content of deposited carbon is observed in these samples (e.g. NiCu11, NiCu12, NiCu14, and NiCu18). On the contrary, bimetallic catalysts with small amount of Cu such as NiCu81 are stable during glycerol conversion.

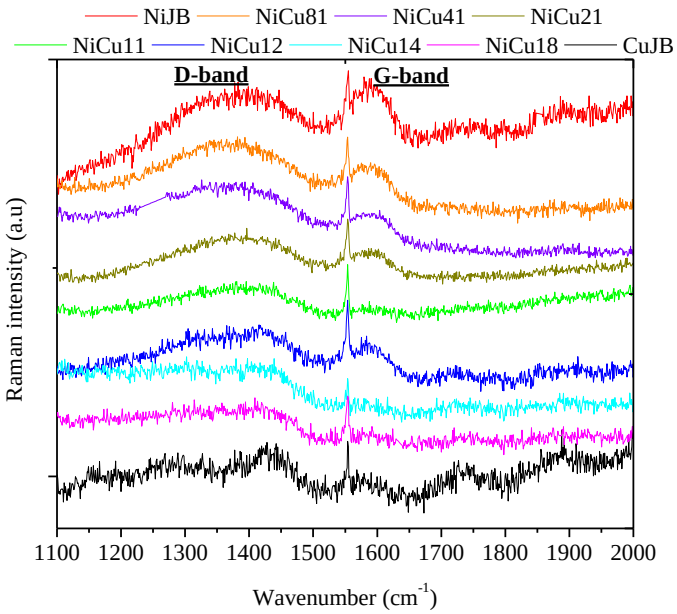

Figure 4.11 Raman spectra of the used Ni-Cu/γ-Al_2O_3 catalysts

4.6 Discussion

The dependence of the adsorption properties and the glycerol hydrogenolysis was evaluated for the bimetallic Ni-Cu system. Our results demonstrate the effects on addition of Cu into Ni/γ-Al_2O_3 catalyst on glycerol conversion and selectivity as well as adsorption properties.

The bimetallic Ni-Cu system is very well distributed on the γ-Al_2O_3 support. In addition, the XRD analysis (Figure 4.4c and d) reveals that the amount of intermetallic alloy in the Ni-Cu system is very poor. Small amount of Ni-Cu alloy were formed on the Ni-Cu catalysts.

Evidence that the surface compositions of the Ni-Cu catalysts are different from bulk compositions is provided by H_2-chemisorption (Table 4.2) and XPS analyses (Table 4.3). XPS results show that Cu is enriched on the catalyst surface. In addition, the number of exposed metallic Ni atoms determined by H_2-chemisorption declines progressively when the Ni/Cu atomic ratio decreases (Table 4.2). This indicates that Cu is recovering the Ni particles.

TPR (Figure 4.3) and XANES results (Figure 4.7) reveal a considerably lower reduction temperature of NiO in the bimetallic catalysts compared to the monometallic one. This phenomenon suggests that there is an interaction between Cu and Ni species in the catalysts.

The results of glycerol conversion at 573 K show that the addition of Cu into Ni/γ-Al_2O_3 catalyst plays an important key on the selectivity. In fact, a continuous decline is observed in the deep hydrogenolysis route as the Ni/Cu atomic ratio decreases. The CH_4 production sharply decreases by the addition of small amounts of Cu and it continues to decrease with increasing Cu content over the whole range of the Ni/Cu atomic ratios. As a result higher selectivity towards dehydration products such as hydroxyacetone is observed (Table 4.4). Selectivity profiles of CH_4 and dehydration products (pyruvaldehyde and hydroxyacetone) versus the total number of exposed Ni atoms at 1 h of reaction are shown in Figure 4.12a. Higher the total number of exposed metallic Ni atoms higher is the CH_4 selectivity. When small amount of Cu is added such as in the NiCu81 sample a decrease of 45 % of the total number of exposed Ni atoms is observed (Table 4.2). This is reflected in the increase of the dehydration products (Table 4.4).

The effect of Cu on Ni/γ-Al_2O_3 observed here can be attributed to geometrical effect and/or change in electronic properties. The geometric effect would affect the number of Ni sites available for adsorption. The H_2-chemisorption (Table 4.2) results suggest that Cu is the predominant component in the surface of the catalyst as the Ni/Cu atomic ratio decreases. Cu progressively covers the Ni atoms, which is further reinforced by our XPS results (Table 4.3). As already mentioned, the chemisorption and XPS results suggest that Cu tends to cover the Ni surface. In these regards the activity of Ni atoms towards CH_4 formation is greatly affected as illustrates Figure 4.12(b). This effect may be explained by a geometrical effect of dilution of the active hydrogenolysis Ni sites by the presence of Cu atoms. J. H. Sinfelt [35] has observed dramatic activity losses in the ethane

hydrogenolysis on Ni when small amounts of Cu are added to the catalyst. On the other hand, lower effects were observed on the same Ni-Cu samples for the dehydration of cyclohexane [36, 37].

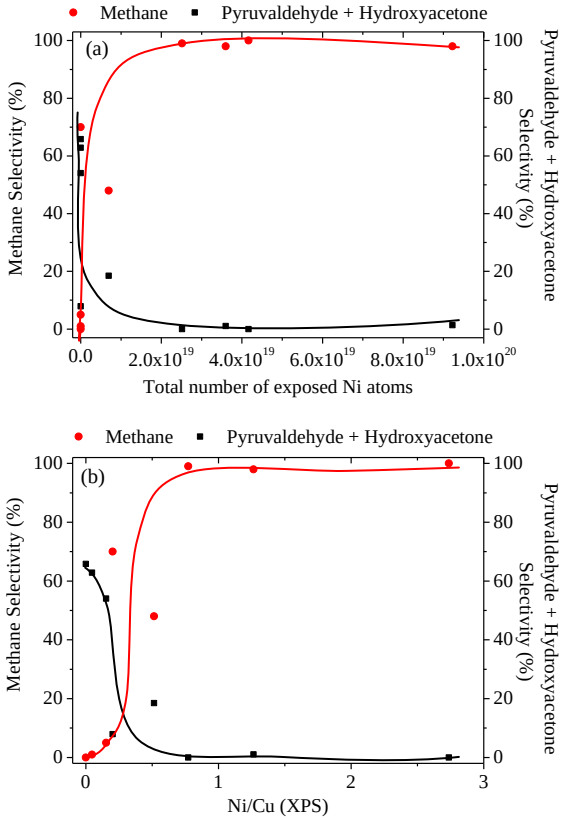

Figure 4.12 Selectivity of CH_4 and dehydration products (pyruvaldehyde and hydroxyacetone) at 1 h of reaction (a) versus the total number of exposed Ni atoms, and (b) versus atomic ratio Ni/Cu

The geometrical effect is noted by the FTIR of adsorbed CO results (Figure 4.6) revealing the progressive elimination of CO molecule bridge bounded to Ni atoms which are observed at the low frequency band at 2000 cm^{-1}–1800 cm^{-1}. In this respect, the active Ni sites for rupture of C-C bond of glycerol may require a large ensemble of atoms. Adjacent Ni atoms on the catalyst surface can form suitable ensemble for the hydrogenolysis route. The probability of finding a suitable array of active Ni atoms to accommodate the reactive molecule may greatly decreases when Cu is dispersed on the Ni catalyst surface. In this way, the decline in the CH_4 production (Table 4.4) during glycerol reaction reflects an effect of coverage of Ni sites by Cu sites. By contrast, the sites for

dehydrogenation and dehydration routes are less sensitive to coverage of the surface by Cu. This is reinforced by the presence of CO molecule linearly bounded to one Ni atom in all range Ni/Cu studied (Figure 4.6).

Electronic modifications of Ni by the presence of Cu are shown by XANES results (Figure 4.7). The observed lower reduction temperature of NiO in the bimetallic catalysts compared to the monometallic one suggests an electronic interaction. According to Pauling [38] Cu has the effect of decreasing the percentage of the d-character of Ni, and thus it can cause an inhibition of C-C bond rupture of glycerol. This electronic effect is observed on Ni-Cu catalysts during the glycerol conversion. Another potential evidence for the electronic effect is supported by the FTIR of adsorbed CO (Figure 4.6). Upon addition of Cu to Ni species, there is a red shift of approximately 38 cm^{-1}. The CO stretching vibration is predicted to shift from pure Ni as compared to the bimetallic Ni-Cu sample according the Blyholder´s scheme [39].

Our results reveal that the geometrical effects are dominant and smaller effects could be attributed to an electronic modification of Ni by the presence of Cu. It is clear that the presence of the Group IB metal such as Cu with the Group VIII metal such as Ni led to inhibition of the rupture of the C-C bond of glycerol. This line of reasoning leads to the expectation that the presence of Cu markedly inhibits the hydrogenolysis activity of Ni rendering more selectivity to dehydrogenation and dehydration of glycerol.

4.7 Conclusions

The catalytic conversion of glycerol to value-added compounds was investigated over bimetallic Ni-Cu/γ-Al_2O_3 catalysts. Different Ni/Cu atomic ratios of 8/1, 4/1, 2/1, 1/1, 1/2, 1/4, and 1/8 were studied in order to determine the effect of introduction of Cu into Ni/γ-Al_2O_3 catalyst. The Ni-Cu catalysts were characterized, before and after catalytic reaction.

HRTEM revealed metal particles very well distributed on the support with particle size of 1.5 nm to 5 nm. XRD analysis revealed that the Ni-Cu samples are not perfect intermetallic alloys. XPS analysis revealed that the surface composition of the catalysts exhibited progressive enrichment of Cu as its content in the catalyst increased. H_2-chemisorption indicated that the total number of exposed Ni atoms decreased as the Cu content increased. As a result, in the deep hydrogenolysis which produces CH_4, the rupture

of the C-C bond by hydrogenolysis decreases by addition of small amounts of Cu and continues to decrease until totally be suppressed. As the Ni/Cu atomic ratio decreases the dehydration-dehydrogenation routes start to prevail, and hydroxyacetone, pyruvaldehyde, lactic acid and pyruvaldehyde are formed. The most interesting feature is the marked difference in the effect of Cu on the catalytic activity of Ni for the glycerol conversion, so a general reaction pathway was proposed (Scheme 4.1) for the conversion of glycerol over Ni-Cu catalysts.

FTIR spectra of adsorbed CO revealed that Cu asserts both geometric and electronic effects on the adsorption properties of Ni. The geometrical effect is visualized by the progressive disappearance of the bridge-bound adsorbed CO on metallic Ni by the incorporation of Cu. This suggests that the deep hydrogenolysis of glycerol to CH_4 requires an ensemble of adjacent active Ni atoms. The electronic effect of Cu on Ni is indicated by the red shift of the IR peak of adsorbed CO as the Cu content increases. The electronic interaction between Cu and Ni species was also substantiated by the XANES results.

It is clear that the presence of Cu with Ni led to inhibition of the rupture of C-C bond of glycerol. This line of reasoning leads to the expectation that the presence of Cu markedly inhibit the hydrogenolysis activity of the Ni rendering more selectivity to dehydrogenation and dehydration of glycerol.

Catalytic deactivation was observed in the glycerol conversion by coke formation. Raman spectra displayed two main bands D and G ascribed to carbon species. TPO results showed an increase in carbon deposition in the samples with higher Cu. This indicates the direct involvement of Cu species in the dehydration of glycerol which markedly contributes to the carbon deposition on the catalysts.

4.8 References

[1] B.C. Miranda, R.J. Chimentão, J.B.O. Santos, F. Gispert-Guirado, J. Llorca, F. Medina, F. López Bonillo, J.E. Sueiras, Appl. Catal. B. 147 (2014) 464-480.
[2] P. Li, J.Liu, N.Nag, P.A.Crozier, J. Catal. 262 (2009) 73-82.
[3] F. Bonet, S. Grugeon, L. Dupont, R. Herrera Urbina, C. Guéry, J.M. Tarascon, J. Solid State Chem. 172 (2003) 111–115.
[4] I. Chen, S. Lin, D. Shiue, Ind. Eng. Chem. Res. 27 (1988) 926-929.
[5] I. Chen, D.W. Shiue, Ind. Eng. Chem. Res. 27 (1988) 429-434.
[6] J. R.A. Sietsma, H. Friedrich, A. Broersma, M. Versluijs-Helder, A. Jos van Dillen, P. E. de Jongh, K.P.d. Jong, J. Catal. 260 (2008) 227–235.
[7] G. Li, L. Hu, J.M. Hill, Appl. Catal. A. 301 (2006) 16-24.

[8] S.K.G. Subramani Velu, Kenzi Suzuki, Munusamy Vijayaraj, Sanmitra Barman, Chinnakonda S. Gopinath, Applied Catalysis B: Environmental. 55 (2005) 287-299.
[9] I. Gandarias, J. Requies, P.L. Arias, U. Armbruster, A. Martin, J. Catal. 290 (2012) 79-89.
[10] H. Kusaka, M. Onuki, Y. Hara, Appl. Catal. 185 (1999) 227-235.
[11] M. Kang, M. W. Song, T. W. Kim, K.L. Kim, Can. J. Chem. Eng. 80 (2002) 63-70.
[12] A. R. Naghash, T. H. Etsell, S. Xu, Chem. Mater. 18 (2006) 2480-2488.
[13] A. Carrero, J.A. Calles, A.J. Vizcaíno, Chemical Engineering Journal. 163 (2010) 395-402.
[14] Y. Li, J. Chen, L. Chang, Y. Qin, J. Catal. 178 (1998) 76-83.
[15] M. Khzouza, J. Wood, B. Pollet, W. Bujalski, Int. J. Hydrogen Energy. 38 (2013) 1664-1675.
[16] J-H. Lin, P. Biswas, V. V. Guliants, S. Misture, Appl. Catal. A. 387 (2010) 87-94.
[17] J. Lif, I. Odenbrand, M. Skoglundh, Appl. Catal. A. 317 (2007) 62-69.
[18] E.L. de León-Quiroz, B.A. Puente-Urbina, D.Vázquez-Obregón, L.A. García-Cerda, Materials Letters. 91 (2013) 67-70.
[19] F. Vila, M. López Granados, M. Ojeda, J.L.G. Fierro, R. Mariscal, Catal. Today. 187 (2012) 122-128.
[20] B. D. Cullity, S.R. Stock, Elements of X-ray diffraction, Addison-Wesley, United States of America, 2001.
[21] A. Hornésa, P. Bera, M. Fernández-García, A. Guerrero-Ruiz, A. Martínez-Arias, Appl. Catal. B. 111-112 (2012) 96-105.
[22] J. Batista, A. Pintar, J. P. Gomilšek, A. Kodre, F. Bornette, Appl. Catal. A. 217 (2001) 55-68.
[23] A. Kitla, O. V. Safonova, K. Föttinger, Catal. Lett. 143 (2013) 517-530.
[24] K. Hadjiivanov, M. Mihaylov, D. Klissurski, P. Stefanov, N. Abadjieva, E. Vassileva, L. Mintchev, J. Catal. 185 (1999) 314-323.
[25] J.W.C. Liberatori, R.U. Ribeiro, D. Zanchet, F.B. Noronha, J.M.C. Bueno, Appl. Catal. A. 327 (2007) 197-204.
[26] X. Zhu, Y-p. Zhang, C.-j. Liu, Catal. Lett. 118 (2007) 306-312.
[27] M. Mihaylov, O. Lagunov, E. Ivanova, K. Hadjiivanov, Top. Catal. 54 (2011) 308-317.
[28] N-Y. Topsøe, H. Topsøe, J. Mol. Catal. A: Chem. 141 (1999) 95-105.
[29] W.Suprun, M. Lutecki, T. Haber, H. Papp, J. Mol. Catal. A: Chem. 309 (2009) 71-78.
[30] A. Corma, P. J. Miguel, A.V. Orchilles, J. Catal. 145 (1994) 171-180.
[31] F. Auneau, C. Michel, F. Delbecq, C. Pinel, P. Sautet, Chem. Eur. J. 17 (2011) 14288-14299.
[32] F. F. de Sousa, H. S. A de Sousa, A. C. Oliveira, M. C. Junior, A. P. Ayala, E.B. Barros, B. C. Viana, J. M. Filho, A.C. Oliveira, Int. J. Hydrogen Energy. 37 (2012) 3201-3212.
[33] A. C. Ferrari, J. Robertson, Phys. Rev. B. 61 (2000) 14095-14107.
[34] A.C. Ferrari, B. Kleinsorge, G. Adamopoulos, J. Robertson, W.I. Milne, V. Stolojan, L.M. Brown, A. LiBassi, B.K. Tanner, J. Non-Cryst. Solids. 266-269 (2000) 765-768.
[35] J.H. Sinfelt, Adv. Catal. 23 (1973) 91.

[36] P. Biloen, J. N. Helle, H. Verbeek, F. M. Dautzenberg, W.M.H. Sachtler, J. Catal. 63 (1980) 112.
[37] Y. Soma-Noto, W.M.H. Sachtler, J. Catal. 32 (1974) 315.
[38] L. Pauling, Proc. R. Soc. London, Ser. A 196 (1949) 243.
[39] G. Bylholder, J Phys. Chem. 68 (1964) 2772.

Appendix

Appendix A. Calibration curves

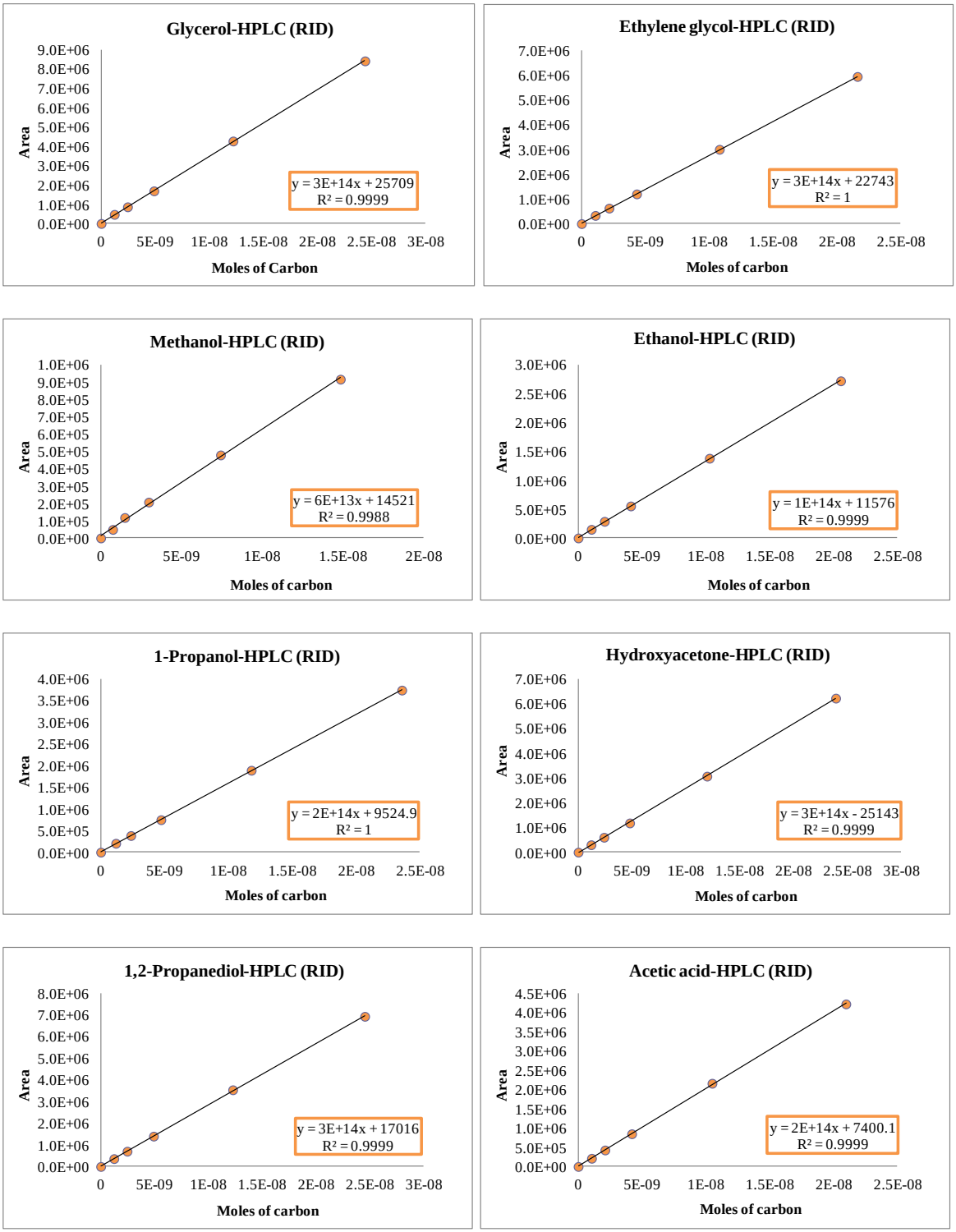

Figure A.1-Calibration curves

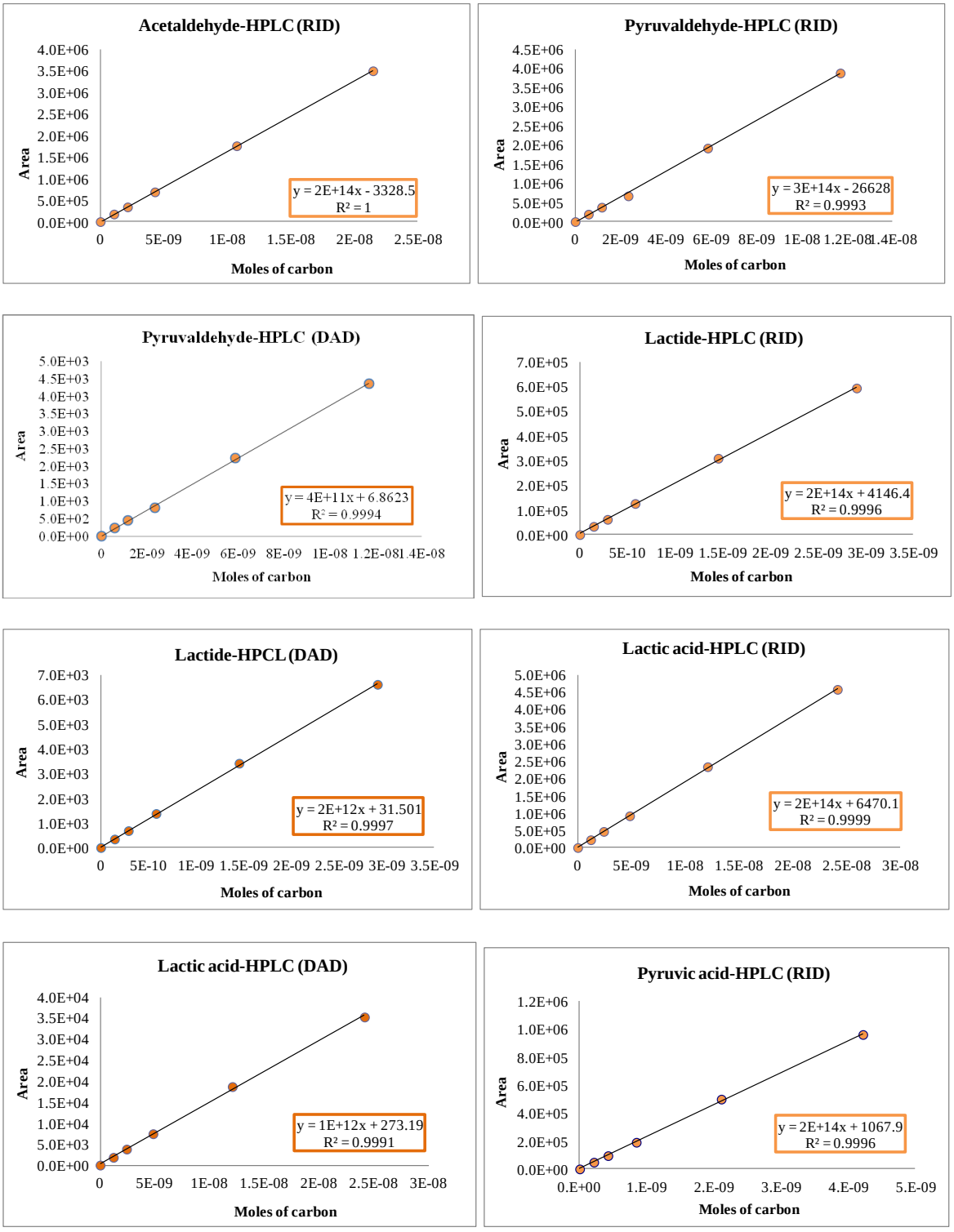

Figure A.1 (continuation) Calibration curves

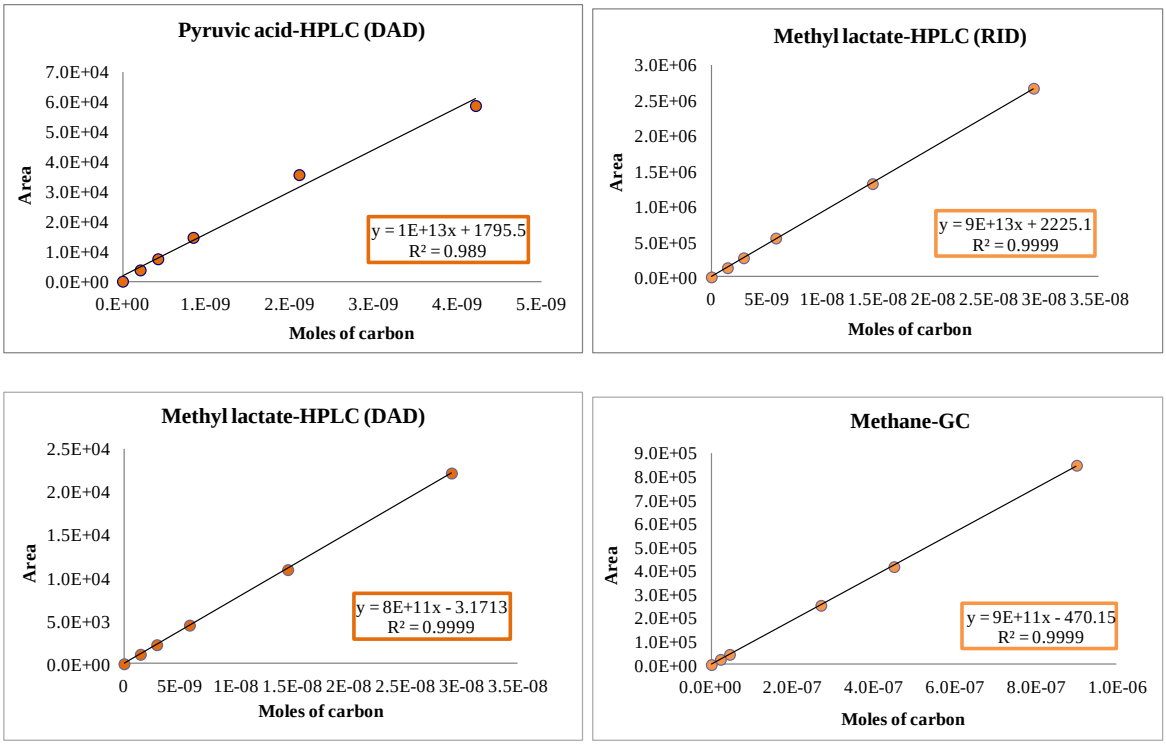

Figure A.1 (continuation) Calibration curves

Appendix B. Identification of products by GC-MS, GC, and HPLC

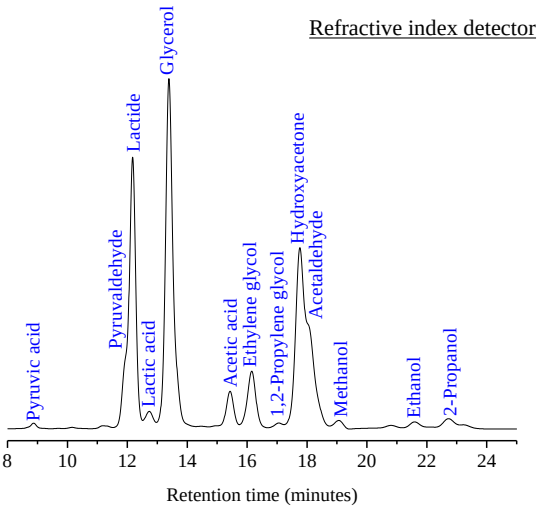

Figure B.1 Detected products by HPLC with RID detector

Table B.1 Compounds identified by GC-MS and their retention times

Number in chromatogram (Fig. B.2)	Compound	Retention time (min)
1	Acetaldehyde	1.44
2	Propanal	1.58
3	Acetone	1.68
4	Furan, tetrahydro	1.84
5	Methanol	2.02
6	Ethanol	2.36
7	2,3-Butadione	2.81
8	2-Butanone, 3-hydroxy	7.94
9	Hydroxyacetone	8.16
10	Acetaldehyde, hydroxy	8.43
11	1-Propanol	8.65
12	Glycolaldehyde dimer	8.89
13	Acetic acid	10.31
14	Propanoic acid	11.30
15	Propanoic acid, 2-methyl	11.60
16	Propylene glycol	11.95
17	1,3-Dioxane	12.10
18	Ethylene glycol	12.36
19	2-Methoxy-1,3-dioxolane	13.00
20	3(2H)- Furanone, dihydro-2-methyl	17.32
21	1,3-Dihydroxyacetone dimer	17.43
22	Glycerol	19.32

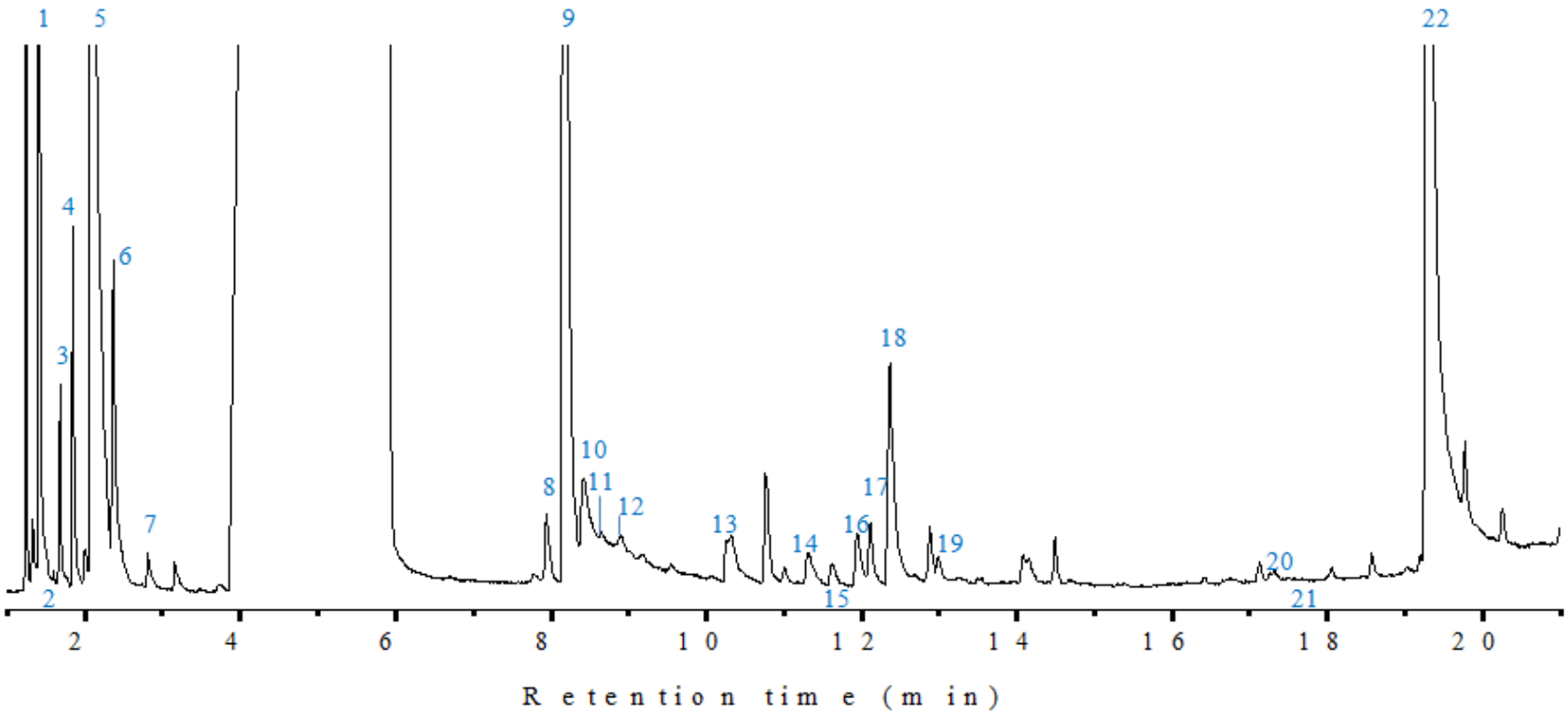

Figure B.2 Chromatogram of identified products obtained by GC-MS (see Table B.1)

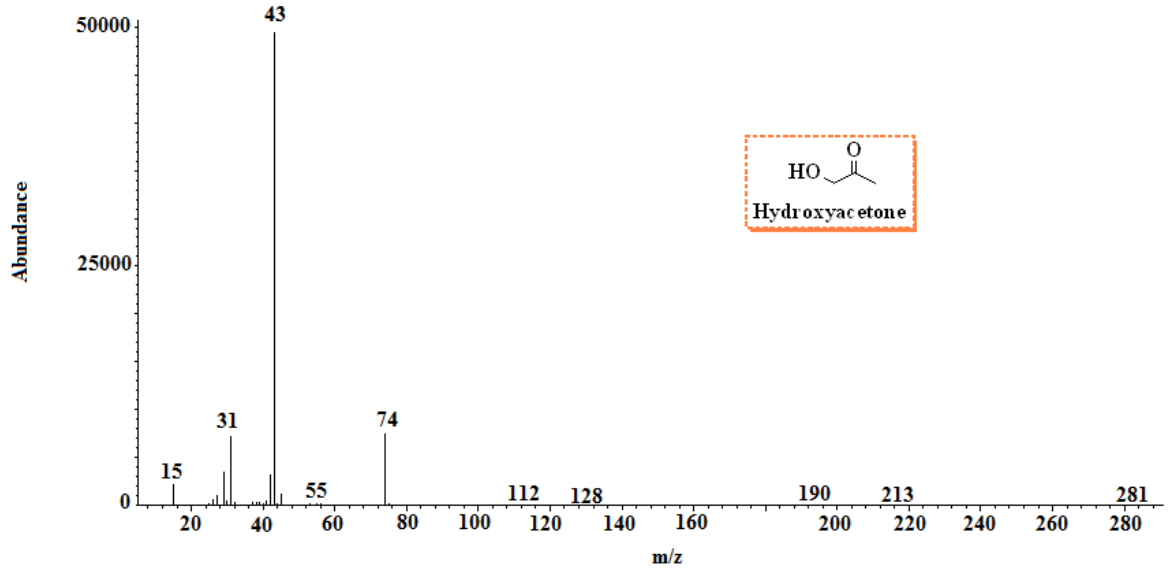

Figure B.3 Mass spectrum of hydroxyacetone (peak 9 identified in Figure B.2)

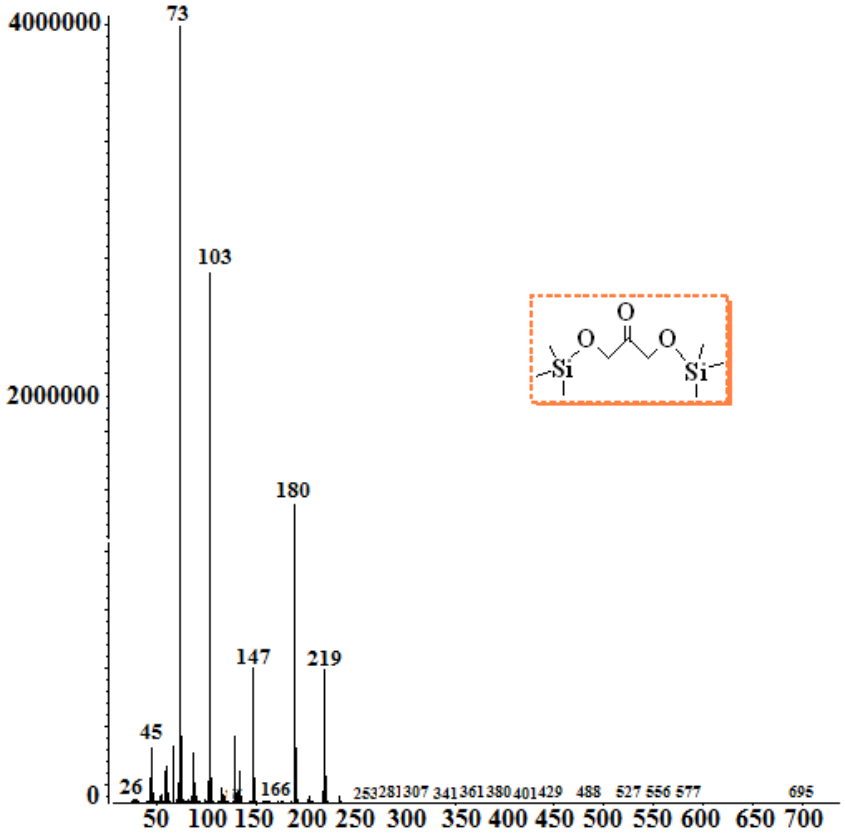

Figure B.4 The mass spectrum of dihydroxyacetone (identified by derivatization method)

Appendix C. XPS graphs obtained for the Ni-Cu/γ-Al_2O_3 catalysts reduced at 723 K

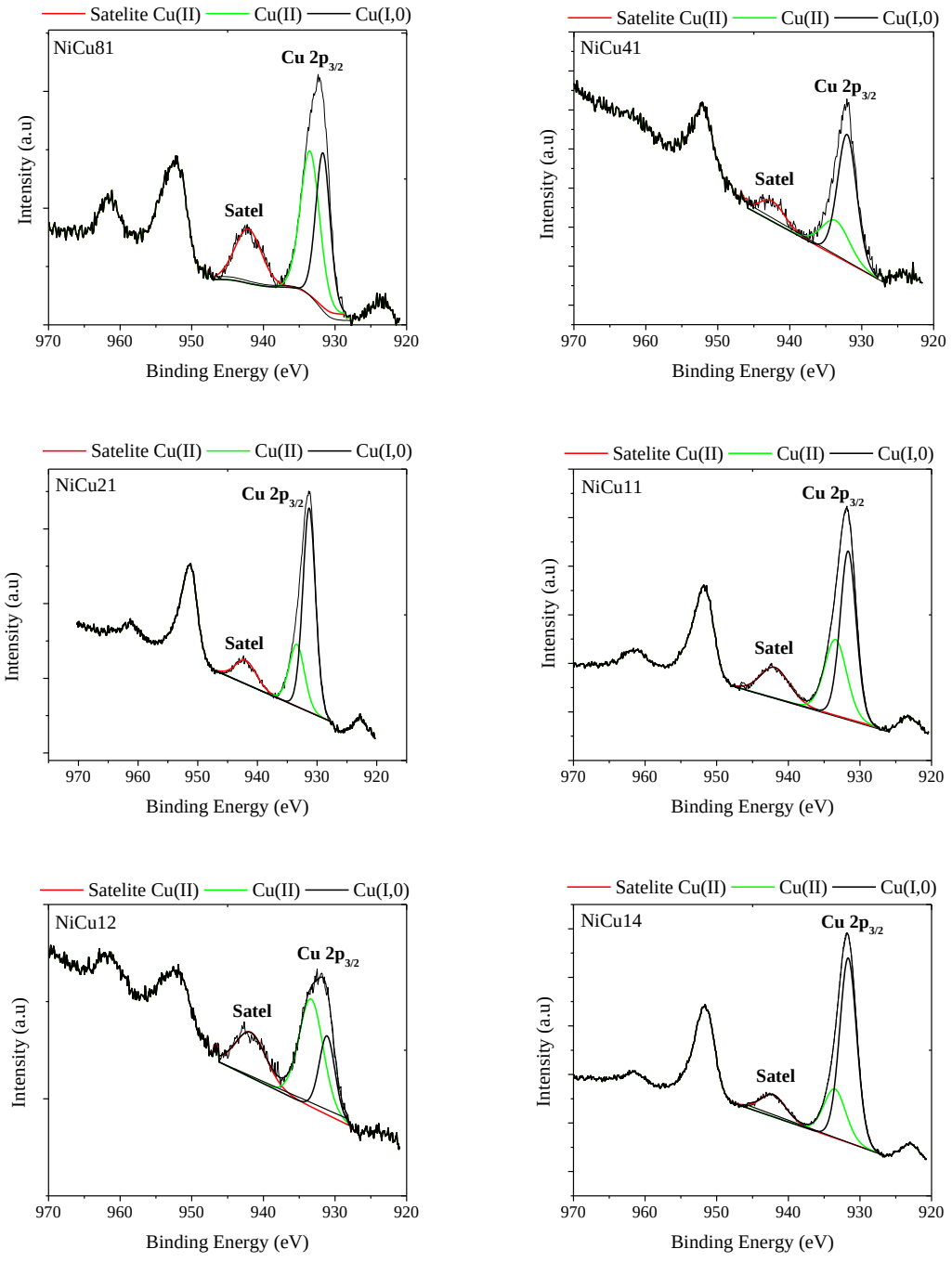

Figure C.1 Orbitals of Cu $2p_{3/2}$ deconvolution

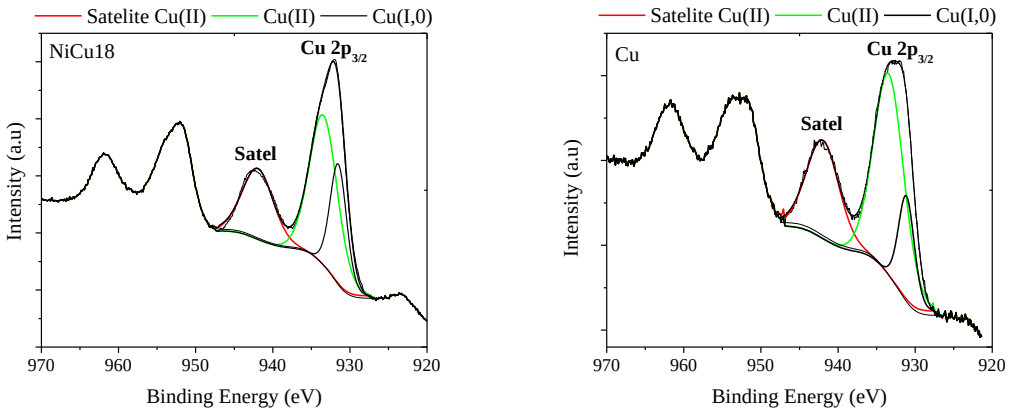

Figure C.1 (continuation) Orbitals of Cu $2p_{3/2}$ deconvolution

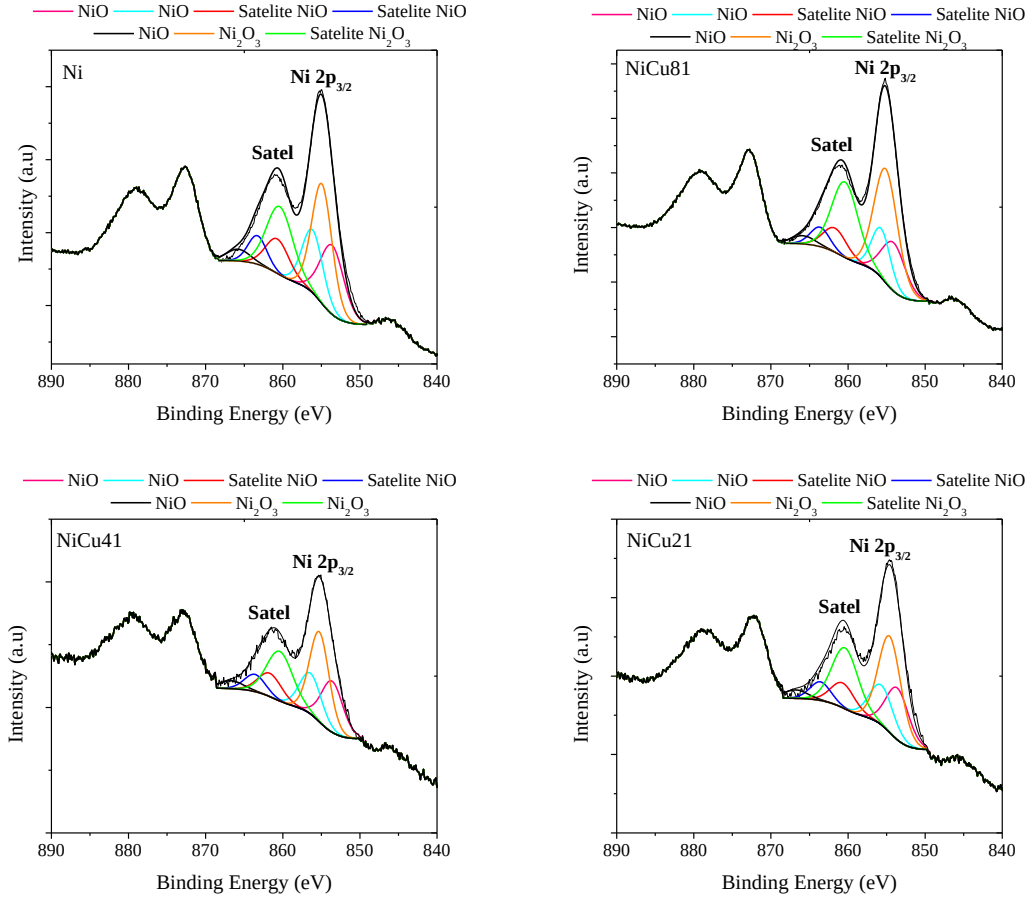

Figure C.2 Orbitals of Ni $2p_{3/2}$ deconvolution

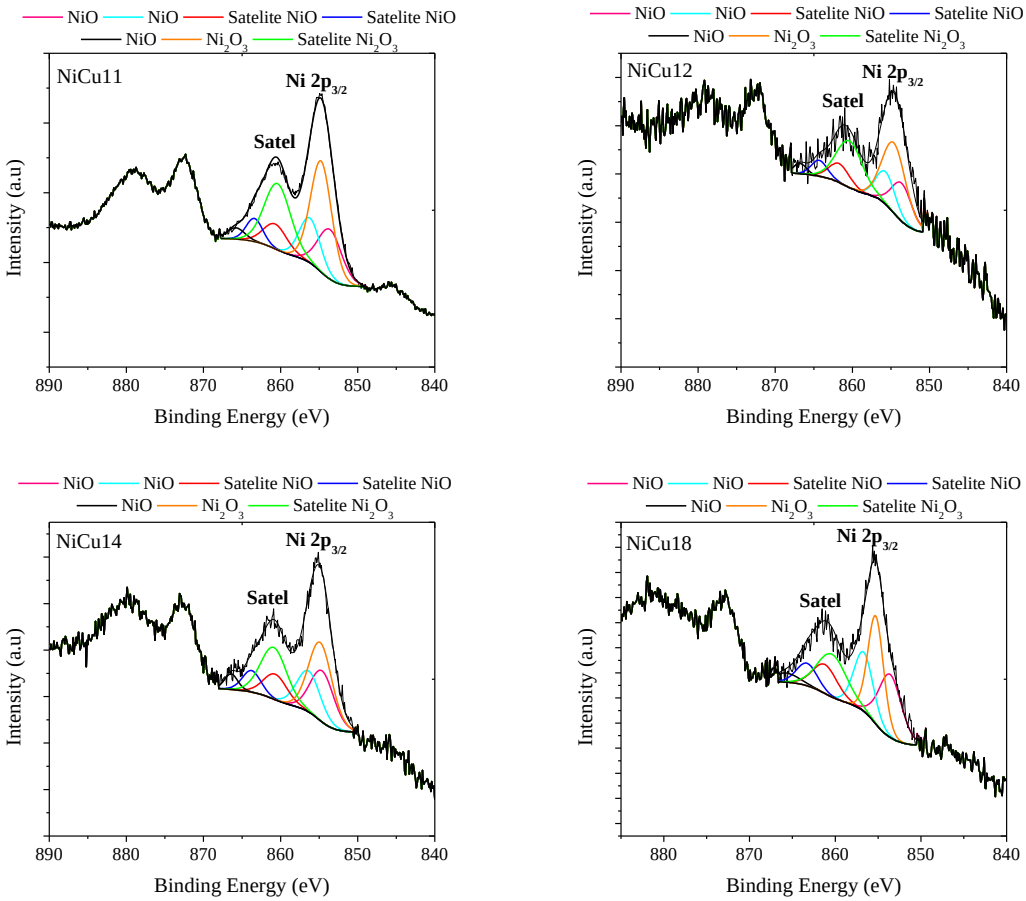

Figure C.2 (continuation) Orbitals of Ni $2p_{3/2}$ deconvolution

Publications and Conferences

Contributions in refereed journals

- **B. C. Miranda**, R. J. Chimentão, J. B. O. Santos, F. Gispert-Guirado, J. Llorca, F. Medina, F López Bonillo, J. E. Sueiras. Conversion of glycerol over 10%Ni/γ-Al_2O_3 catalyst, Applied Catalysis B: Environmental, 147 (2014) 464-480.
- **B. C. Miranda**, R. J. Chimentão, J. Szanyi, J. B. O. Santos, J. Llorca, F. Medina. Influence of copper on nickel-based catalysts in the hydrogenolysis of glycerol, *submitted to Applied Catalysis B: Environmental*.
- R. J. Chimentão, **B. C. Miranda**, J. Szanyi, J. B. O. Santos, J. Llorca, F. Medina. Deactivation and regeneration process of nickel based catalyst in the glycerol transformation, *submitted to Applied Catalysis A: General*.

Contributions in refereed conferences

- **B.C Miranda,** R. J. Chimentão. Hydrogenolysis of glycerol in gas phase over Ni/γ-Al_2O_3 catalyst. Cat4Bio Conference: Advances in Catalysis for Biomass Valorization, 8 – 11 July, 2012, Thessaloniki, Greece. Poster Communication
- **B.C Miranda,** R. J. Chimentão. Deactivation of the catalyst 10%Ni/γ-Al_2O_3 during the conversion of glycerol. SECAT'13 Catalizadores y Reactores Estructurados, 26 – 28 June, 2013, Sevilla, Spain. Poster Communication
- **B.C Miranda,** R. J. Chimentão**.** Conversion of glycerol over 10%Ni/γ-Al_2O_3 catalyst**.** XIX Congreso Latinoamericano de Ingeniería Química (COLAEIQ), 22 – 26 July, 2013, San José, Costa Rica. Oral Communication
- **B.C Miranda,** R. J. Chimentão**.** Conversion of glycerol over **1**0%NiCu/γ-Al_2O_3 bimetallic catalysts**.** XIX Congreso Latinoamericano de Ingeniería Química (COLAEIQ), 22 – 26 July, 2013, San José, Costa Rica. Poster Communication